Thesis

Investigation into Joint Use of UHF and VHF Bands For Future Internet of Things – Field Test Platform and Measurement Campaigns

Student: Daniel Wright
Supervisor: Eddie Ball

August 2021

Acknowledgement

I would like to thank everyone at the University of Sheffield that has provided help and encouragement throughout my time at the university. I would particularly like to thank my academic supervisor, Eddie Ball for his constant guidance and expertise, which proved to be of invaluable assistance.

Thank you to all my fellow students and researchers for providing friendship and camaraderie throughout the long hours spent working in the laboratory and office.

A special thank you goes to my family for their unwavering support throughout my studies.

Finally, I would like to thank the UK Engineering and Physical Sciences Research Council (EPSRC) for providing the funding that made this PhD possible.

Abstract

The UK telecommunications regulator, Ofcom, decided in 2016 to repurpose parts of the VHF spectrum between 55MHz and 81.5MHz for use in Internet of Things applications. It is believed by Ofcom that the VHF band can provide more reliable long range communications when compared to currently commercially operated UHF spectrum, due to the more favourable propagation characteristics of lower frequencies. The Internet of Things is an important, large and growing sector of communications technology with many important applications, so investigation of this re-purposed spectrum could prove to be beneficial. Studies could facilitate the design of highly reliable systems by supplying detailed knowledge of the characteristics of the new spectrum across multiple different environments.

In order to conduct a propagation and spectrum measurement study a very expensive commercially produced spectrum analyser would normally be required. This thesis takes a different approach by developing an instrument using Software Defined Radio techniques with Commercial Off the Shelf hardware, this produces a very low cost instrument. It is shown that the Software Defined Radio instrument is capable of performing a propagation study to a high degree of agreement with a commercial spectrum analyser, thus validating the approach. Readings of received power taken by the instrument are shown to agree with readings taken at the same locations with a commercial spectrum analyser to within an average of 1.4dB at 71MHz and 1.1dB at 869.525MHz. These readings of received power along with GPS locations in relation to a known transmit power allow propagation and shadowing to be calculated, background noise present in the measurements is also recorded.

The developed instrument is used to conduct a propagation study in a number of different environments (rural, suburban, urban and dense urban), with measurement equipment deployed in a manner suitable for a portable, short range (up to 2km) IoT use case with receiving antennas placed close to the ground. Results are presented in comparison to other propagation studies available in the literature and widely used propagation models such as the Hata model. Shadowing and noise are also measured and examined. It is found that current propagation models do not provide adequate predictions of path loss within the considered use case, with Root Mean Squared Errors of up to 72.4dB between measured and predicted path loss. The collected data is used to calculate log-distance based path loss propagation models that provide good predictions, with Root Mean Squared Errors of between 5.5dB and 9.0dB when comparing measured path loss to the calculated models path loss predictions. Path loss is found to be constantly lower, by between 20dB and 33dB, at VHF than UHF, but RF noise is consistently higher by between 8dB and 18dB at VHF.

The instrument is then further developed, so it may be used remotely to make long-term observations of the VHF and UHF spectrum at a static location in order to observe how the spectrum behaves over a number of days. Initial testing was performed in a sub urban environment for 6 days, with the intention of longer future deployments to rural, sub urban, urban and dense urban environments once the testing confirms the changes to the instrument function properly. In the studied area RF noise was again found to be consistently higher at VHF, by an average of 16dB, over the whole 6 day timespan of the measurements. Waterfall plots were produced that show qualitatively that more RF interference was measured in the considered environment at the VHF band. The number of users in each band was assessed by

manual examination of the waterfall plots, with the UHF band found to be much more heavily used than the VHF band (up to 12 users in the UHF band and 3 to 5 in the VHF band), with some areas seemingly congested. Work is continuing to produce better spectrum sensing algorithms to allow quantitative measurements of interference and users.

Overall, the newly released spectrum is found to compare favourably with the currently well used Short Range Devices band in all the examined environments and therefor be suitable for IoT deployments. Different strengths and weaknesses were identified in each band with VHF having lower path loss and less congested spectrum, UHF having lower noise and less interference. IoT communications could be provided by either band or a combination of both to allow the strengths of each to be exploited, increasing reliability, such as by the use of VHF spectrum to avoid congestion in the UHF band.

Contents

List of Figures

List of Tables

Chapter 1

Introduction

Inspired by the constant growth and importance of the Internet of Things (IoT) sector and Ofcom's re-purposing of parts of the VHF spectrum between 55MHz and 81.5MHz for IoT use, this thesis will examine the use of the re-purposed spectrum to deliver high reliability IoT access. IoT communication is currently provided at frequency bands around the 868MHz short-range device (SRD) or 2.4GHz Wi-Fi bands, the newly re-purposed bands are much lower in frequency and may be able to provide much more reliable long range IoT due to the difference in propagation characteristics. It is also considered that with Radio frequency (RF) spectrum scarcity a redundant dual band system utilising the currently used and repurposed bands together could improve IoT reliability.

This thesis covers the creation of a low-cost software defined radio (SDR) based instrument using commercial off the shelf (COTS) components that is able to perform measurements of the re-purposed VHF band and the UHF SRD band at the same time. The instrument is small and portable allowing it to meet a mobile IoT use case. This SDR instrument is then transported around various environments (rural, suburban, urban and dense urban) to perform a propagation study, in order to compare the path loss at both VHF and UHF. Modifications are then made to the instrument to allow for long term observations at a single location, observing RF noise and interference as well as the number of other users in each band as a measure of congestion.

Comparisons of all these measurements are made between the two bands in order to assess whether the newly re-purposed band is suitable for IoT communications in different environments and if it is more reliable than the current VHF band. Also explored are levels of congestion in each band and if these levels are problematic and use of both bands together could produce an increase in reliability.

The following papers based on work in this thesis have been published:

D. P. Wright and E. A. Ball, "Highly Portable Software Defined Radio Test Bed for Dual Band Propagation Studies," in The Loughborough Antennas Propagation Conference (LAPC 2018), Nov 2018, pp. 1–6. [3]

D. P. Wright and E. A. Ball, "Highly Portable, Low-cost SDR Instrument for RF Propagation Studies," IEEE Transactions on Instrumentation and Measurement, vol. 69, no. 8, pp. 5446–5457, August 2020. [4]

D. P. Wright and E. A. Ball, "Iot Focused VHF and UHF Propagation Study and Comparisons," IET Microwaves, Antennas & Propagation, vol. 15, no. 8, pp. 871–884, 2021. [5]

This first chapter provides an introduction to the thesis, covering the background of the IoT use case and the technology exploited to allow the subsequent research to be performed. It also includes a detailed list of the contribution and novelty of the work in this thesis.

Chapter 2 provides the background knowledge of RF engineering required to produce the work in this thesis. RF wave properties are discussed with reference to their effects on propagation. Noise and interference are defined for use within the thesis. Properties of the Fast Fourier Transform in relation to RF frequency domain measurements are outlined. Finally the properties of antennas are discussed, with the ones to be used in the thesis listed and described.

Chapter 3 details the literature review that was conducted for the thesis. It covers widely used propagation models as well as the latest research in propagation measurement, general RF spectrum measurement and the state-of-the-art for research using SDR based instruments.

Chapter 4 deals with the design, construction and validation of an instrument to take measurements in the VHF and UHF bands for analysis and comparison.

Chapter 5 describes how propagation studies were conducted by moving through rural, suburban, urban and dense urban environments using the instrument developed in Chapter 4. Measurements are presented and analysed with reference to current models.

Chapter 6 shows how the instrument from chapter 4 was modified to provide long-term remote measurements of the RF spectrum in a static location, which are communicated back to a central point via the cloud. Initial measurements were taken and are presented.

Chapter 7 provides an overview of the conclusions derived from the research performed in the thesis. Ideas for future work for are also discussed.

1.1 Existing IoT Technologies and Use Cases

IoT is the idea of using multiple small, low cost sensors connected via the internet gathering data to aid in planning, monitoring and operation of people, places and processes. Many applications have been found in this area including smart homes (e.g. monitoring heating or security) Smart Cities (e.g. monitoring traffic or street lighting) and health care monitoring (e.g. monitoring blood glucose analysis or ECG's) amongst others, many more applications will be found wherever the ability to receive data from a remote sensor is desirable. Fig. 1.1 shows examples of IoT use cases.

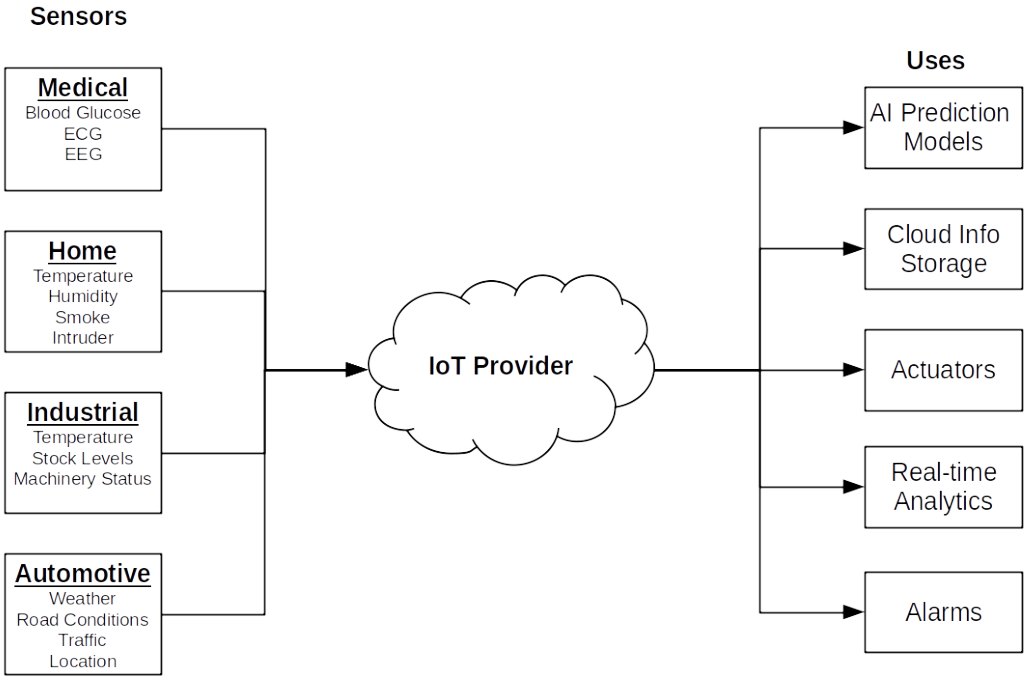

Figure 1.1: Example IoT Use Cases

IoT is a rapidly growing area of communication technology with competing standards (led by Sigfox and LoRa). The IoT market is predicted to rise with 7 billion devices currently deployed and up to 22 billion devices expected to be deployed by 2025 [6]

A number of companies are working on commercial solutions targeted at the low power IoT market, these are in various stages of development and deployment. Within the EU these devices are regulated by EN 300 220-1 witch defines restrictions on radiated power, channel access duty cycle and maximum bandwidth amongst other things [7]. A selection of existing technologies are discussed here, this list is not exhaustive.

LoRa: LoRa is a protocol developed by the LoRa Alliance for battery operated IoT. The protocol describes a Low Power Wide Area Network (LPWAN) laid out in a star topology and uses the frequency band 867MHz to 869MHz in the UK [8]. The topology of a theoretical LoRa network is designed so user end nodes are connected to gateways via RF signals, these gateways then use existing Backhaul to connect to network servers owned by the LoRa Alliance, these network servers then connect via the internet to the customer's application servers [8]. Different specifications are used for a LoRa systems in Europe and North America, for instance Europe uses the frequencies 867-869MHz with a max power of 14dBm while North America uses 902-928MHz with a max power of 30dBm. Data rates are 250bps to 50kbps in Europe and 980bps to 21.9kbps in North America. Specifications for other areas have not yet been finalised [8]. Multiple LoRa RF transceivers are available from companies such as the Microchip and Semtech. Many end user products have been designed and deployed by a number of companies, including rail temperature sensors, remote lighting controls and smart water meters [9].

Sigfox: Sigfox is a LPWAN with a star topology for small message payloads, 12 bytes uplink, 8 bytes downlink. As with LoRa, messages are transmitted from user devices via RF to base stations, messages are then passed to the Sigfox cloud and on to users via the internet [10]. Sigfox operates over 200kHz

of the 868MHz band. Only 140 uplink messages and 4 downlink messages are permitted per day to meet the restrictions set out in EN 300 220-1 for a 0.1% duty cycle [7]. Downlink messages must be requested by the device. A "several year" battery life is anticipated for user devices. Encryption and scrambling are supported, each message is signed with a private key unique to the message and device. User devices have data rates of 100bps and 600bps with a maximum power of 22dBm [10]. Multiple transceivers, SoC and modules are available from Silicon Labs, Texas Instruments, Atmel and Others. Sigfox systems are currently deployed in areas such as smart meters and wireless alarms [11].

HaLow 802.11ah: HaLow has been designed by Wi-Fi alliance as an extension to the 802.11 Wi-Fi standard. Operating in the 900MHz band for lower power consumption and longer range, the standard claims to offer 1km of range, much further than traditional Wi-Fi [12]. Hardware is not yet available for this standard, Qualcomm claim to be in the R&D phase of their efforts, therefor no HaLow systems are currently deployed [13]. Wi-Fi alliance are targeting Smart Home and Smart City markets.

The IoT market is still in its early stages with only a small number of providers up and running at a commercial scale, but with its usefulness already understood across a number of sectors. Outside of Europe and North America the specifications and standards are still in flux, with plenty of scope for research projects to provide influence on future developments.

1.2 Spectrum

It has been stated that the competing standards Sigfox and LoRa use the 868MHz SRD band. They attempt to use novel modulation schemes to achieve long range communication at this frequency. This work will attempt to discover if long range urban IoT communication can be provided more reliably via the combined or single use of lower frequency bands.

In an attempt to encourage the IoT market in the UK, new spectrum has been allocated the by UK telecommunications regulator Ofcom for use in IoT applications in the following bands: 55-68MHz, 70.5-71.5MHz and 80.0-81.5MHz, it is hoped these new frequencies will enable reliable, long range communication between devices due to the more favourable propagation characteristics of lower frequencies, which are discussed further in Chapter 2. However, the smaller antennas often used in IoT applications have much worse efficiency at these frequencies, possibility nullifying this advantage. Interest has also been shown in the USA and Japan for re-purposed, now vacant, VHF and UHF television bands [14].

Ofcom is focusing this repurposed spectrum on providing IoT in rural areas [15]. In a recent public consultation respondents agreed with Ofcom's rural approach [15]. However, there is no reason this new spectrum should only be used rurally, urban uses are worth investigation to identify any possible benefits.

Ofcom states that there have been very few recent noise and propagation studies for the frequencies of 50MHz to 100MHz and even though the current consultation is closed they are still very interested in any new information and studies in this area [15], this shows a clear need for the planned investigations in this area. Ofcom states that information they have received indicates that noise at these frequencies can be high and is increasing [15]. The International Telecommunication Union (ITU) currently has an active study question asking for information for terrestrial IoT type propagation at frequencies over 30MHz [16].

In order to investigate these newly available bands and identify the characteristics of their use in an IoT use case, a propagation study is conducted in this thesis.

1.3 Reliability Requirements for Future Systems

The ITU defines the reliability of a communication system as the probability over a given time that the system can meet its required performance expectations when operating within specified conditions [17]. IoT could benefit from a high reliability approach due to the nature of some of its suggested uses. The health care sector is a large user of IoT, failures of an IoT device could lead to a patient welfare issue. In smart farming, failures of an IoT device could lead to an animal welfare issue. Failure of an IoT security device could lead to a personal safety issue or financial loss. Failure on an IoT device in any time sensitive environment could lead to disruption, such the failure of a "just in time" stock system. If users can have confidence in the reliability of IoT they will be more likely to employ it for a wider range of uses. With the huge number of IoT devices planned to be deployed and the well known scarcity of RF spectrum resources, congestion in the utilised bands could degrade reliability, which a dual band VHF / UHF redundant system could address.

Hecht [18] sets out four areas which can be exploited to reduce the probability of failure and therefore increase reliability. The first area is during the system design, taking a cautious approach, such as the use of specific high reliability parts and operating well within known parameters giving large margins for failure. The second area is during design analysis, properly using known techniques to examine potential failure modes and fault trees to establish areas in need of re-design in order to correct potential reliability problems. The third area is testing to verify the design meets reliability expectations, gaining knowledge of the environment of operation, including at extreme conditions. The fourth area is redundancy, by providing back-up functionality in order to allow continued operation in case of an unexpected failure.

In this thesis extensive testing of the RF environment at the repurposed VHF band and the currently utilised band UHF band will be conducted. This will facilitate Hecht's third area of high reliability design via the provision of knowledge of the environment of operation, it is proposed that due to more favourable propagation characteristics, such as lower penetration loss and reduced scattering with longer wavelengths [1], lower VHF spectrum could be exploited for use in low power, high reliability communications systems [19]. It will also be established if the repurposed VHF band is suitable for replacement or redundant use, to avoid congestion when compared to the UHF band, thus facilitating Hecht's fourth area of high reliability design.

1.4 Brief Technology Background

SDR involves transferring the functions of a radio from a hardware focus to a software one. It consists of the minimum amount of hardware necessary to receive an RF signal and convert it to a digital signal that is readable by a processing device such as a computer, microprocessor or FPGA. Software techniques are then used to manipulate the digital signal it to useful information [20]. The idea of SDR enables the RTL-SDR device used in this research for the necessary RF measurements. The use of SDR over a traditional radio provides many advantages, SDRs are easily adaptable via updates to their software, providing long life cycles and making them easy to repurpose [21]. Development costs and lead times are also reduced due to the lack of required hardware development [22]. Fig. 1.2 shows a basic diagram of a generic SDR set up with a superheterodyne receiver connected to an IQ demodulator providing digital information to a processing device.

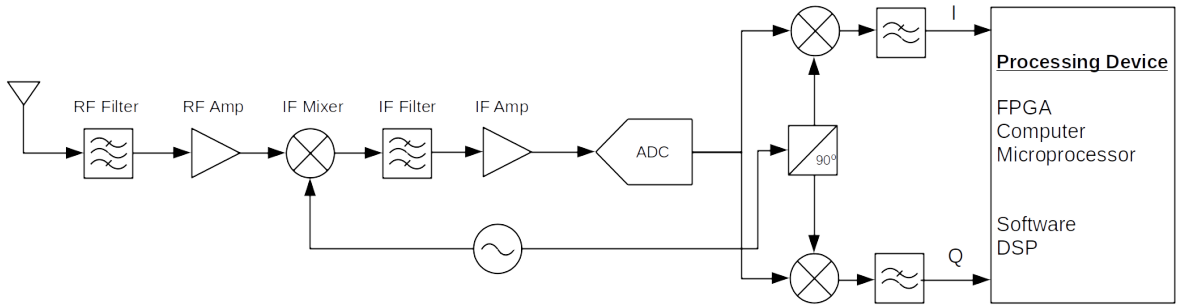

Figure 1.2: Example of a Generic SDR Setup

Cognitive Radio (CR) is the idea of an intelligent, autonomous radio capable of observing all areas of its operation and physical surroundings, it can then adjust its operation to achieve the greatest quality of service possible [20]. SDR provides the enabling technology for this idea due to its reprogrammable and flexible nature [23]. CR's employ dynamic spectrum management and often use GPS in conjunction with Geolocation databases to select appropriate spectrum to use [22]. A typical CR architecture could include an SDR enhanced by the addition of a spectrum sensor and a cognitive engine. Each stage of the receivers operation and the surrounding spectrum could be observed, with the readings fed to the cognitive engine, the engine than makes decisions regarding adjustment of the CR's operation, the decisions are fed to the SDR for implementation [22]. Ideas also exist for cognitive networks of CR's which would constantly monitor and adjust performance at a network level by sharing data between CR nodes in the network, such as the idea of using a cooperative approach to create a dynamic propagation map of the environment by sharing data between nodes.

Standards are currently available including aspects of CR, giving an idea of intended uses for CR in the near term:

- **IEEE 802.22:** Standard for CR use of Television White Space (TVWS) from 54MHz to 862MHz in Wireless regional area networks. This standard is specifically aimed at enabling wireless broadband access for up to 512 devices over a 100km radius, it concerns itself with ways to reduce interference with the primary users of the spectrum (TV stations) by using geolocation databases and spectrum sensing [24].
- **IEEE 802.11af:** Standard for the use of TVWS to extend 802.11 Wi-Fi, including use of geolocation databases [25].

From these standards it is possible to see that plans are already under way for CR use in the VHF band. The work completed in this thesis to evaluate the use of VHF spectrum for IoT use could be used to develop CR IoT networks at these frequencies.

1.5 Research Activity, Contribution and Novelty

This thesis presents measurements of the VHF and UHF RF spectrum for use in an IoT use case. Measurements are taken of path loss to allow comparisons of the link budget at each frequency, measurements of RF noise and congestion are also made. This allows these measurements to be compared to provide a determination as to if the newly re-purposed spectrum can provide IoT communication to the same standard as the SRD band spectrum and if a dual band approach could enhance reliability beyond

the current standard. In order to perform these measurements it was decided to design, build and test an SDR based instrument so this thesis also covers this work.

The use case considered in this work is for a portable IoT device. The device should be able to be carried by one person, so it may be used as a personal device e.g. in some kind of heath care monitoring. Being human portable also means that the antenna will be close to the ground and its radiation pattern may be affected by the human body or other method used for transport, like a car.

In order to represent the small antennas common in IoT applications and keep the measurement platform portable, small antennas are used, it is accepted that these antennas may not provide the best performance but will provide a realistic result.

Chapter 4 describes the SDR based instrument's development. The goal was to produce an instrument capable of conducting a propagation study to a similar standard as a commercial spectrum analyser within a specific use case and for specific frequencies. This is accomplished by finding cost and complexity savings by focusing only on IoT propagation at specific frequencies, rather than attempting to replicate the entirety of the functions of a commercial spectrum analyser. It is accepted that outside of the stated use case the performance of the instrument described in this chapter is not comparable to a commercial spectrum analyser.

The novelty and contribution of this chapter is:

1. Low cost of the instrument with comparable performance to a spectrum analyser over the stated frequency bands and use case.
2. The highly portable nature of the instrument, allowing hundreds or even thousands of measurements to be taken in a much shorter time than a traditional manual spectrum analyser based study.
3. Producing an instrument capable of taking measurements and producing models which closely match an IoT deployment i.e. a close to ground, on body, mobile RX and a building height TX with distances starting from less than 1km. Current widely used empirical models such as Hata only cover distances greater than 1km, frequencies from 150MHz to 1500MHz and TX deployed at a height of at least 30m.
4. Producing an instrument capable of taking measurements in this IoT deployment style of newly re-purposed IoT spectrum in the VHF ($\sim$70MHz) band. This spectrum has not previously been considered for urban IoT.
5. Initial results obtained from the platform are presented for an urban field trial, leading to a measurement based propagation model.

Chapter 5 describes a propagation study performed by the developed instrument in rural, suburban, urban and dense urban environments. The instrument was transported through the environments, taking measurements at multiple locations of received power and RF noise. These measurements are used to develop path loss models based on the log-distance method including shadowing. Results for VHF and UHF are compared to each other and currently accepted propagation models in order to assess the suitability of the re-purposed spectrum for IoT use.

The novelty and contribution of this chapter is:

1. Provide an IoT focused propagation study at $\sim$70MHz, which is a frequency not previously used for IoT. The instrument will be deployed consistently with the portable IoT use case previously outlined.
2. Provide comparisons between currently utilised IoT spectrum in the $\sim$869MHz SRD band and the re-purposed $\sim$70MHz band, identifying comparative strengths and weaknesses.

3. Provide comparisons between ITU predictions (for propagation, noise, shadowing and clutter) and an extensive set of real world measurements.

4. Provide new propagation models for the measured re-purposed ∼70MHz band based on the Log-Distance pathloss model.

Chapter 6 discusses the modification of the instrument described in chapter 4, the instrument is then placed in a static indoor, suburban location in order to provide long term measurements of the RF spectrum in a selected environment. Measurements are sent from the instrument to be analysed by a PC via a cloud computing service, it is envisioned that in future work this will allow multiple instruments to be deployed to multiple environments at the same time with a central system observing them. FFT measurements are taken of the RF spectrum around 71MHz and 869.525MHz, including RF noise and how it changes in an environment over time, also the number of other users in the band and subsequent congestion.

The novelty and contribution of this chapter is:

1. Develop a low cost distributed instrument capable of long term RF measurements in a single environment.

2. Provide a platform for the future research and development of spectrum sensing techniques, such as those discussed in Section 3.3, which is cheaper and more flexible than current platforms, such as the one developed by Yarkan [26]. It is able to facilitate real world measurements, not simulations as used by Bao *et al.* [27]

3. Provide a long term study of RF noise in an environment and how it changes over time, especially around the frequencies re-purposed by Ofcom for IoT use, as it is stated there has been few studies in this area.

4. Provide a long term observation of the number of users within the UHF SRD and VHF bands, assessing and comparing the congestion present.

The novelty described for chapters 4 and 5 is confirmed by the work in these chapters being accepted for publishing in the academic journals ‘IEEE Transactions on Instrumentation and Measurement‘ and ‘IET Microwaves, Antennas & Propagation‘ [4] [5].

Chapter 2

RF Engineering Background

This chapter deals with the theoretical background knowledge necessary to complete the work in this thesis. It begins by describing RF waves and their interaction with the environment. It will provide the definitions of noise and interference use in the thesis, describe how the Fast Fourier Transform is used to perform the required measurements and the background of the antennas that are used.

In order to understand RF propagation it is beneficial to understand the background surrounding RF waves and their interaction with the environment. RF waves are composed of magnetic fields (H), caused by current flow and electric fields (E), caused by electrical charges. These fields are mutually orthogonal from each other and the direction of propagation (S), this relationship is shown in Fig. 2.1. The directions of the fields are referred to as their polarisation.

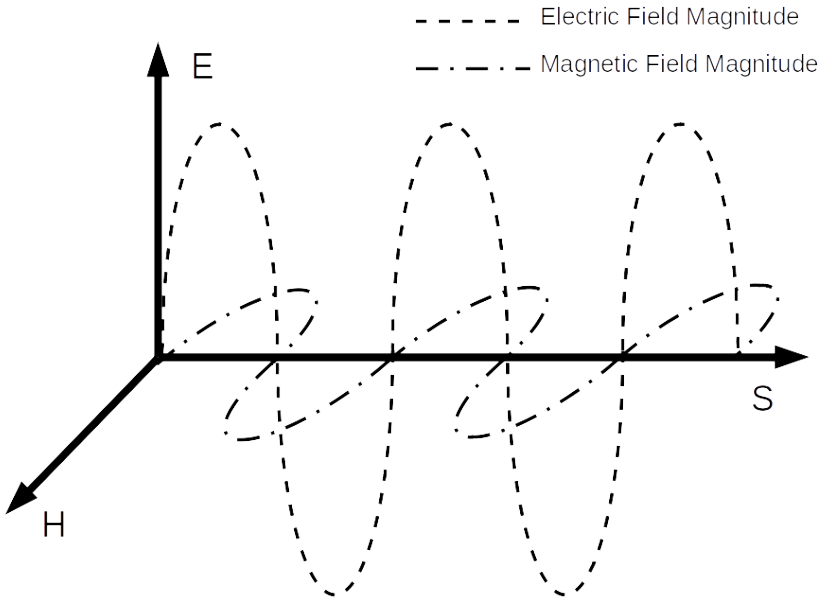

Figure 2.1: Relationship Between the Electric Field, Magnetic Field and Direction of Propagation of an RF Wave

The interaction of these fields with a given medium depends on the permeability, permittivity and conductivity of the medium in question. The propagation of RF waves are affected by reflection from smooth surfaces, scattering from rough surfaces and diffraction around objects, with differing effects based on the wavelength of the wave and / or EM properties of the surface. These ideas will be further explored in this section. Because part of this thesis involves comparisons of propagation at 71MHz and

869.525MHz, wherever it is appropriate, comments will be made on how the ideas affect RF waves at these different frequencies to different extents.

2.1 Material Properties

Materials can be classified as dielectrics or conductors, most materials have properties of both but are classified according to their dominant property. Perfect Dielectrics have no conductivity, as conductivity increases materials become known as Lossy Dielectrics, with the loss increasing until conductivity becomes the dominant property and the material is classified as a conductor.

The permeability of a material shows the relationship between the applied magnetic field and the density of magnetic flux within the material, thus providing a measure of how susceptible a material is to the formation of a magnetic field. The relationship is given in (2.1) [28]:

$$B = \mu H \tag{2.1}$$

where:
B = Magnetic Flux Density (T)
μ = Permeability (H/m)
H = Magnetic Field Strength (A/m)

The permittivity of a material shows the relationship between the applied electric field and the density of electric flux within a material, thus providing a measure of how susceptible the material is to polarisation by an electric field and how well it stores energy. The relationship is given in (2.2) [28]:

$$D = \varepsilon E \tag{2.2}$$

where:
D = Electric Flux Density (C/m^2)
ε = Permittivity (F/m)
E = Electric Field Strength (V/m)

The conductivity of a material shows the relationship between the electric field and the current flowing within it, thus providing a measure of how good a conductor a material is. The relationship is given in (2.3) [28]:

$$J = \sigma E \tag{2.3}$$

where:
J = Current Density (A/m^2)
σ = Conductivity (S/m)

2.2 Reflection

If, as an RF wave propagates it passes from a certain medium in to contact with a second medium of a different type, some of the waves energy will be reflected at the boundary of these mediums and some

will be transmitted from the first in to the second. The amount of energy reflected or transmitted depends on the electrical properties of the different mediums, polarisation of the wave, angle of incidence on the boundary and the frequency of the wave. The Plane of incidence is shown by the vector of the propagated wave towards the medium boundary

By considering two polarisations of RF wave it is possible to examine the effects of reflection. Fig. 2.2 shows a representation of the interaction when the electric field is in the same plane as the plane of incidence, with the magnetic field extending out of the paper at 90° to the electric field. Fig. 2.3 show a representation of the interaction when the magnetic field is the same plane as the plane of incidence, with the electric field extending out of the paper at 90° to the magnetic field.

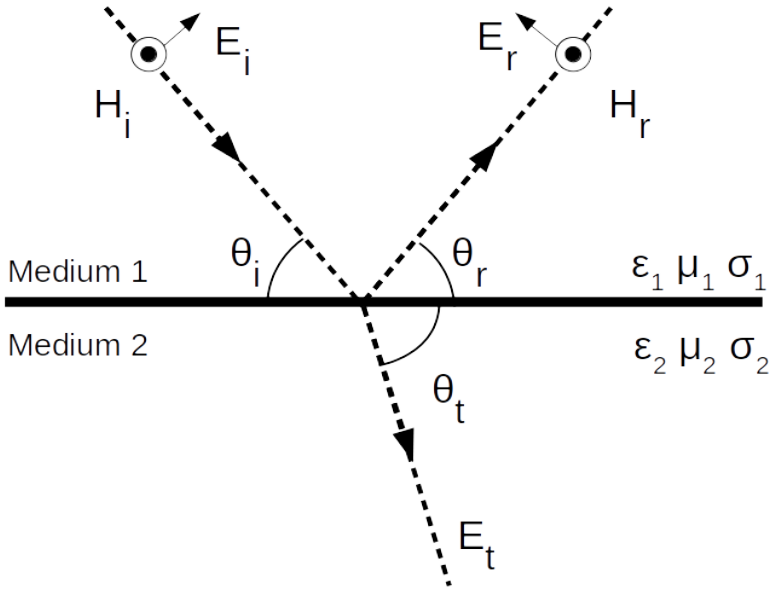

Figure 2.2: Representation of Reflection When the Polarisation of the E Field is in the plane of incidence [1]

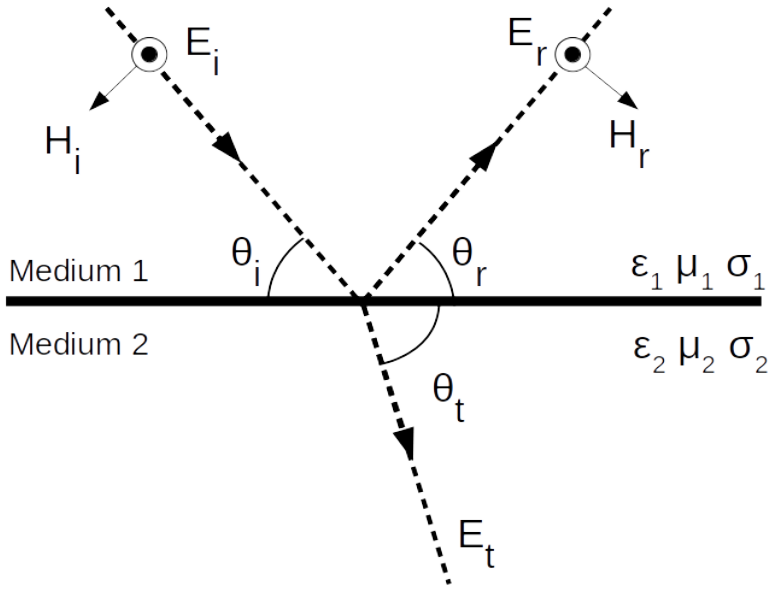

Figure 2.3: Representation of Reflection When the polarisation of the E Field is 90° to the plane of incidence [1]

The reflection coefficient is used to represent the fraction of the RF wave which is reflected at the boundary, with the remainder being transmitted in to the second medium. This relationship is shown in (2.4) [1].

$$E_r = \Gamma E_i \tag{2.4}$$

where:
Γ = Refection coefficient
E_r = Reflected electric field
E_i = Incident electric field

Using Fig. 2.2 and 2.3 with the boundary conditions of Maxwell's equations it is possible to define a reflection coefficient for each of the two different polarisations. Equation (2.5) gives the refection coefficient when the polarisation of the E field is in the plane of incidence and (2.6) gives the reflection coefficient when the E field is at 90° to the boundary [1].

$$\Gamma_{\parallel} = \frac{\eta_2 \sin\theta_t - \eta_1 \sin\theta_i}{\eta_2 \sin\theta_t + \eta_1 \sin\theta_i} \tag{2.5}$$

$$\Gamma_{\perp} = \frac{\eta_2 \sin\theta_i - \eta_1 \sin\theta_t}{\eta_2 \sin\theta_i + \eta_1 \sin\theta_t} \tag{2.6}$$

$$\eta_i = \sqrt{\frac{\mu_i}{\varepsilon_i}} \tag{2.7}$$

where:

$\Gamma_{\parallel}$ = Refection coefficient for vertical polarisation
$\Gamma_{\perp}$ = Refection coefficient for horizontal polarisation
η_1 = Intrinsic impedance of material 1 (Ω)
η_2 = Intrinsic impedance of material 2 (Ω)
θ_i = Angle of incident ray ($^\circ$)
θ_t = Angle of reflected ray ($^\circ$)

Lossless (Perfect) Dielectric

The permittivity of a lossless dielectric can be expressed relative to the permittivity of free space as follows [1]:

$$\varepsilon = \varepsilon_r \varepsilon_0 \tag{2.8}$$

where:
ε_r = Relative Permittivity
ε_0 = Permittivity of free space (8.85×10^{-12} F/m [1])

Lossy Dielectric

If the dielectric is lossy, the permittivity becomes complex, with the complex part representing the absorbed power as follows [1]:

$$\varepsilon = \varepsilon_r \varepsilon_0 - j\varepsilon' \tag{2.9}$$

$$\varepsilon' = \frac{\sigma}{2\pi f} \tag{2.10}$$

where:
σ = Conductivity
f = Frequency

From (2.10) it can be seen that the absorption ($j\varepsilon'$) depends on the conductivity of the medium and the frequency of the RF wave. As frequency increases less power will be absorbed for the same conductance.

Conductor

Perfect conductors do not absorb any power and so reflect all of the waves incident on them. Equations (2.11) and (2.12) show the effect on waves of different polarisation [1].

$$\Gamma_{\parallel} = 1 \tag{2.11}$$

$$\Gamma_{\perp} = -1 \tag{2.12}$$

If the E field is in the same plane as the boundary between the mediums (2.11) shows that is that the wave is reflected and its phase is preserved. If the polarisation of the E field is perpendicular to the boundary between the mediums (2.12) shows that is that the wave is reflected with a 180° phase shift.

2.3 Free Space Propagation

The simplest way to imagine RF wave propagation is to imagine an isotropic antenna radiating equally in all directions through empty space. Transmitted power dissipates over the surface of a sphere with the antenna at the centre [28]. A representation of this is shown in Fig. 2.4 with 'd' representing the distance between two antennas and 'A' representing the aperture of the receiving antenna.

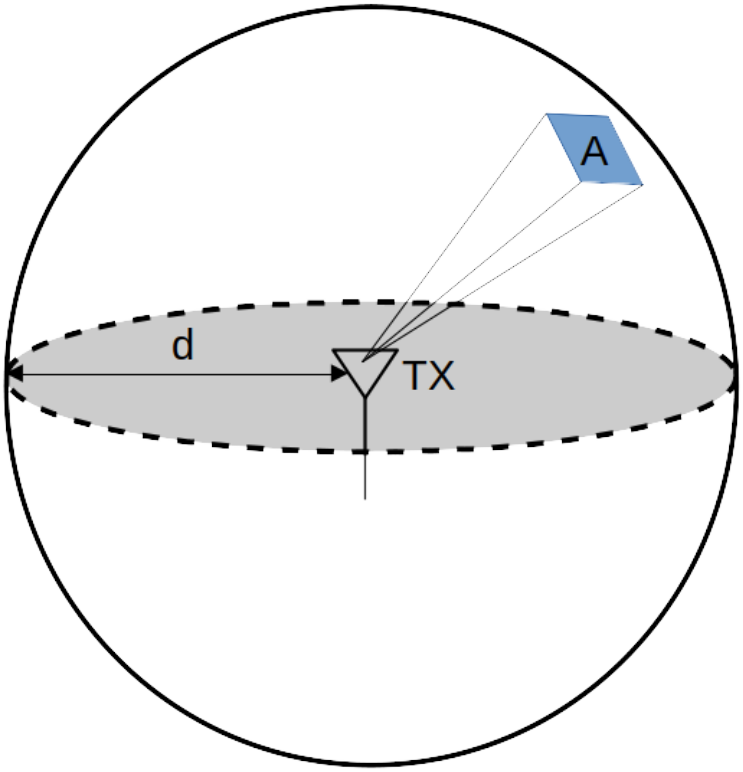

Figure 2.4: Free Space Isotropic Propagation

The surface area of a sphere of radius 'd' is given by:

$$Surface\ Area = 4\pi d^2 \tag{2.13}$$

where:
d = Radius

Because the antenna is isotropic the power it transmits must be equally distributed across the whole surface of the sphere. Therefor it is shown in (2.14) that the receive power at distance 'd' from the antenna decreases by the square of this distance and so is an inverse square law.

$$S = \frac{P_t}{4\pi d^2} \tag{2.14}$$

where:
S = Power density on the surface of a sphere (W/m^2)
P_t = Transmit power at TX (W)

An antenna can only collect the fraction of the power transmitted which is incident upon it. Fig. 2.4 shows the area 'A', this is aperture size of the RX antenna and defines the effective size of the antenna as an area. Antenna aperture is discussed in more detail in section 2.9. Aperture is given by:

$$A = \frac{\lambda^2}{4\pi} \tag{2.15}$$

where:
A = Antenna aperture area (m)
λ = Wavelength (m)

If the amount of power that reaches the RX antenna from (2.14) is combined with the aperture given in (2.15) it is possible to see that the received power can be expressed as:

$$P_r = SA = \left(\frac{P_t}{4\pi d^2}\right)\left(\frac{\lambda^2}{4\pi}\right) \tag{2.16}$$

where:
P_r = Received power (W)

If the gains of the TX and RX antennas are considered the equation becomes:

$$P_r = P_t\left(\frac{\lambda}{4\pi r}\right)^2 G_t G_r \tag{2.17}$$

where:
G_t = Gain of transmitting antenna
G_r = Gain of receiving antenna

This is the most basic way to model RF propagation and does not take in to account any environmental effects. Section 3.1 explores the use of this basic theory to produce a propagation model as well as investigating more complex propagation models.

2.4 Diffraction

Diffraction occurs when an RF wave meets the edge of an obstacle, the wave appears to bend around the obstacle, propagating in to the shadowed region behind the obstacle. This bending is caused by the Huygen's principle, this principle models all points on a primary wavefront as sources of secondary waves, it is these produced secondary waves that propagate in to the shadowed region.

Fig. 2.5 shows a diagram of the Knife Edge Diffraction model, where an RF wave propagates over an object with an edge that is very small compared to its wavelength. The wave is bent, allowing a propagation path between the TX and RX which have no line of sight.

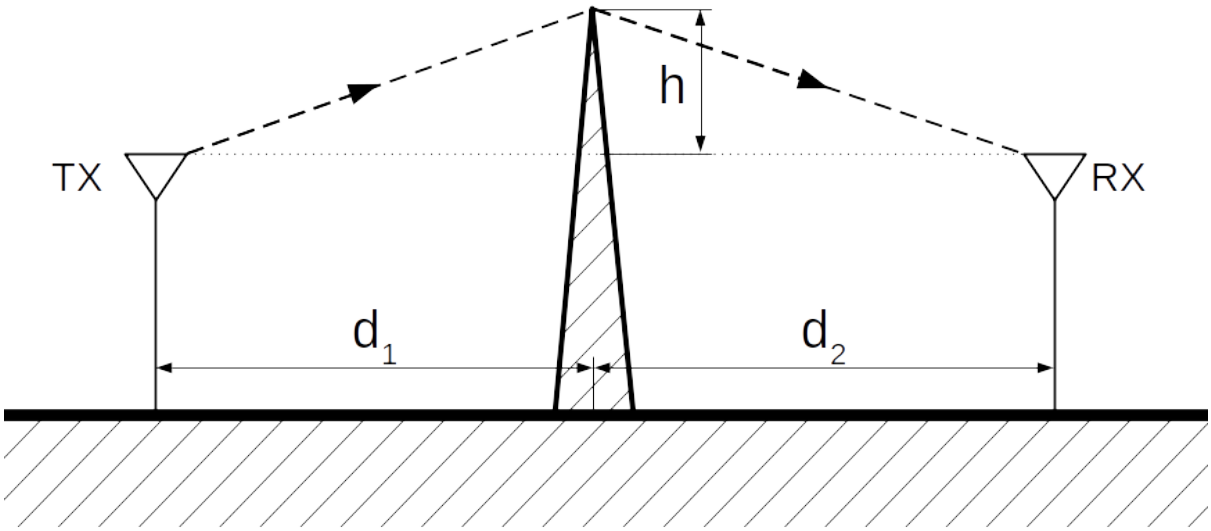

Figure 2.5: Knife Edge Diffraction

The Fresnel-Kirchoff diffraction parameter [1] can be used to analyse the given geometry of the diagram in Fig. 2.5 and is given in (2.18).

$$\nu = h\sqrt{\frac{2(d_1 + d_2)}{\lambda d_1 d_2}} \tag{2.18}$$

where:
ν = Fresnel-Kirchoff diffraction parameter
h = Height of knife edge above antennas (m)
d_1 = Distance between TX and knife edge (m)
d_2 = Distance between RX and knife edge (m)
λ = Wavelength (m)

Diffraction gain, when compared to free space path loss, due to a knife edge can be calculated using the Fresnel-Kirchoff diffraction parameter and is given in (2.20) [1].

$$G_d(dB) = 20\log|F(\nu)| \tag{2.19}$$

$$G_d(dB) = \begin{cases} 0 & \nu \leq -1 \\ 20\log(0.5 - 0.62\nu) & -1 \leq \nu \leq 0 \\ 20\log(0.5\exp(-0.95\nu)) & 0 \leq \nu \leq 1 \\ 20\log\left(0.4 - \sqrt{0.1184 - (0.38 - 0.1\nu)^2}\right) & 1 \leq \nu \leq 2.4 \\ 20\log\left(\frac{0.225}{\nu}\right) & \nu > 2.4 \end{cases} \tag{2.20}$$

where:
$G_d(dB)$ = Diffraction gain
ν = Fresnel-Kirchoff diffraction parameter

Equation (2.20) shows that as the Fresnel-Kirchoff diffraction parameter increase, so does the loss of power compared to the free space loss. To investigate the effects of wavelength it is possible to imagine two scenarios as in Fig. 2.5 with the exact same geometries but different wavelengths. Using (2.18) it is possible to see that a longer wavelength will produce a lower Fresnel-Kirchoff diffraction parameter, thus meaning an RF wave with a frequency of 71MHz will experience less loss than one with a frequency of 869.525MHz

2.5 Scattering

When an RF wave is incident on a surface, a smooth surface will cause the wave to be reflected and a rough surface will cause the wave to be scattered. Surfaces that have a dimension larger than a wavelength of the incident wave are considered smooth and surfaces with a dimension smaller than a wavelength of the incident wave are considered rough. The classification of a surface as rough or smooth can be made using the Rayleigh Criterion [1]:

$$h_c = \frac{\lambda}{8 \sin \theta_i} \tag{2.21}$$

where:
h_c = Critical Height
λ = Wavelength (m)
θ_i = Angle of Incidence (degrees)

If a the maximum size of features on the surface exceed the critical height (h_c), then that surface is considered to be rough.

The work presented in this thesis considers RF waves at 71MHz ($\lambda = 4.23m$) and 869.525MHz ($\lambda = 0.35m$), these wavelengths can be used to calculate the Rayleigh Criterion for each wave, assuming they are incident at 45° using (2.21).

$$\frac{4.23}{8 \sin(45)} = 0.747m \tag{2.22}$$

$$\frac{0.35}{8 \sin(45)} = 0.061m \tag{2.23}$$

From (2.22) and (2.23) it can be seen that the critical height for RF waves incident at 45° is 0.747m for 71MHz and 0.061m for 869.525MHz. From this it can be inferred that, for the same angle of incidence, RF waves at 869.525MHz are more susceptible to scattering than at 71MHz, due to the smaller critical height level required to produce scattering at that wavelength.

To find the reflection coefficient of a rough surface, the reflection coefficient shown in (2.4) must be multiplied by an amount representing the loss caused by scattering, this is known as the scattering loss factor [1]:

$$\Gamma_{rough} = \rho_S \Gamma \tag{2.24}$$

where:
Γ_{rough} = Reflection Coefficient of Rough Surface
ρ_s = Scattering Loss Factor
Γ = Reflection Coefficient of Smooth Surface

The Scattering Loss Factor is given by [1]:

$$\rho_s = \exp\left[-8\left(\frac{\pi\sigma_h \sin\theta_i}{\lambda}\right)^2\right] \tag{2.25}$$

where:
ρ_s = Scattering Loss Factor
σ_h = Standard Deviation of the Mean Surface height
(assumed to be a Gaussian distributed random variable)

By examining (2.25) it is possible to see that increasing wavelength will decrease the scattering loss factor, confirming the inference that more energy will be lost to scattering at 869.525MHz than 71MHz each time an RF wave is reflected.

2.6 Noise

RF noise is defined by the ITU as an unwanted RF effect which varies with time, does not convey information and maybe combined with or block out a wanted signal which does convey information. The ITU specifically excludes from its definition of background noise, signals from other RF spectrum users, such as transmissions within the same channel or spurious emissions [29]. These excluded signals will be considered interference and covered in the next section.

Sources of noise can be divided in to those sources internal to the receiver, such as thermal noise and those external to it. External noise can further be divided in to natural and artificial categories. Natural noise may be produced by atmospheric emissions, weather or radiated from the ground. Artificial noise may be produced by electronic or electrical devices, power lines or engine ignition. Detailed recommendations regarding noise are available from the ITU in their recommendation P.372-14 [29].

Every electronic component generates thermal noise which contributes to the overall noise of any electronic system. The noise power produced by resistor at room temperature, measured over a certain bandwidth is given by:

$$P_n = kT_0B \tag{2.26}$$

where:
P_n = Noise power (W)
k = Boltzmann's constant ($1.38x10^{-23}$ J/K)
T_0 = Room temperature (290K)
B = Measurement bandwidth (Hz)

Noise factor is used to show the degradation in the signal-to-noise ratio (SNR) caused by noise added by a component. This is defined by looking at the ratio of the SNR at the input against the output, as shown here [30]:

$$F = \frac{SNR_{in}}{SNR_{out}} \tag{2.27}$$

where:
F = Noise factor
SNR_{in} = Signal-to-noise ratio at the input
SNR_{out} = Signal-to-noise ratio at the output

For instance an ideal, noiseless, amplifier would amplify a signal and the noise equally, so the ratio would be maintained from input to output. In real systems what actually happens is that the input signal and noise are amplified, but extra noise is added to the output along with the amplified input. This can be represented explicitly as [30]:

$$F = \frac{S}{N_{in}} \Big/ \frac{GS}{GN_{in} + N_a} \tag{2.28}$$

where:
S = Signal
N_{in} = Noise at the input
N_a = Added noise
G = Gain

Sometimes noise figure is used instead of noise factor. This is the noise factor expressed in dB as shown:

$$NF = 10 \log_{10} \left(\frac{SNR_{in}}{SNR_{out}} \right) = SNR_{in}(dB) - SNR_{out}(dB) \tag{2.29}$$

where:
NF = Noise figure (dB)

The idea of effective noise temperature is used to represent noise performance, it is a measure of the temperature a resistor would have to be to at, according to (2.26), to produce the same amount of added noise as is present in a certain device. A resistor at this temperature is imagined to be added to the input of a noiseless device, thus modelling the noise performance of the considered device. Because the resistor is imagined to be added to the input of the device, the devices gain must also be taken in to account, as follows [30]:

$$N_a = GkT_eB \tag{2.30}$$

$$T_e = \frac{N_a}{GkB} \tag{2.31}$$

where:
T_e = Effective noise temperature (K)

The effective noise temperature can be related to the noise figure [30]:

$$T_e = (F - 1)T_0 \tag{2.32}$$

The noise factor of an attenuator, e.g. a transmission line, is equal to its loss at room temperature [1]. At other temperatures it may be found using [29]:

$$F = 1 + (L - 1)\left(\frac{T}{T_0}\right) \tag{2.33}$$

where:
L = Loss
T = Actual temperature

If multiple noisy devices are connected, e.g. in a receiver, each device will have a cascading effect on the noise figure of the system. Each successive device will not only add its own noise to the output, it will amplify the added noise of each device before it. Fig. 2.6 shows an example of a 3 device cascaded system, indicating the output at each intermediate stage of the system.

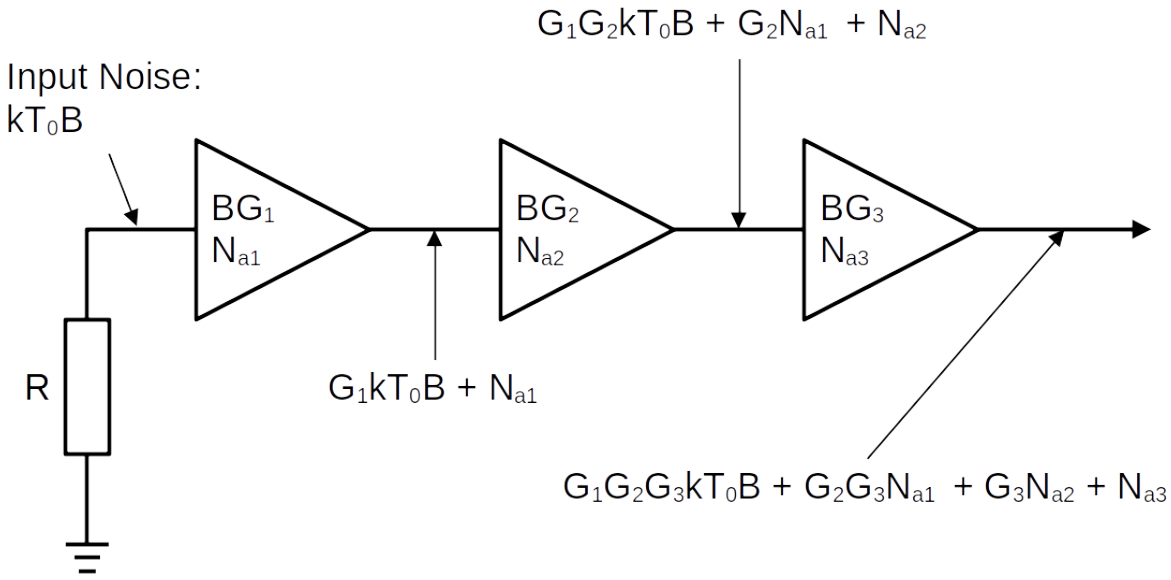

Figure 2.6: Example of a cascaded systems effect on noise figure

The total noise factor of a cascaded system is shown by [1]:

$$F_{sys} = F_1 + \frac{F_2 - 1}{G_1} + \frac{F_3 - 1}{G_1 G_2} + \ldots \frac{F_n - 1}{G_1 G_2 \ldots G_{n-1}} \tag{2.34}$$

where:
F_{sys} = Noise factor of the overall system
F_n = Noise factor of the nth individual component of the system
G_n = Gain of the nth individual component of the system (absolute value)

Alternately the system can be represented using the effective noise temperatures of each device [1]:

$$T_{sys} = T_1 + \frac{T_2 - 1}{G_1} + \frac{T_3 - 1}{G_1 G_2} + \dots \frac{T_n - 1}{G_1 G_2 \dots G_{n-1}} \tag{2.35}$$

where:
T_{sys} = Effective noise temperature of the overall system
T_n = Effective noise temperature of the nth individual component of the system

Using the ideas presented above, the noise an antenna presents to a receiver may be modelled as an equivalent temperature resistor, as in (2.31). The noise here would not just be the thermal noise, all the external natural and artificial noise would be included. In the cascaded equations (2.34) and (2.35) the gain of the antenna would be considered to be 1, regardless of the antennas actual properties.

2.7 Interference

The ITU describes interference in terms of radio communication as the reception of unwanted energy which causes any loss of information in the received signal or any reduction in performance of the system that otherwise would not have occurred [31]. This includes intentional signals from other users as well as unintentional spurious emissions. Signals from other users my be present due to illicit activity or propagation effects such as diffraction, scattering, ducting and multi path components causing RF waves to propagate far beyond their intended, regulatory permitted area of operation. The ITU provides models for predicting interference in [32]. With cognitive radios having the ability to frequency hop, often within unused ‘white space‘ spectrum, the risk of these systems generating interference for other users increases. A measurement of the amounts of interference currently present, as well as how congested with other users some bands currently are will provide interesting data useful for the design of future cognitive radios.

2.8 Fast Fourier Transform

In order to examine the frequency components of a received RF signal the Fast Fourier Transform (FFT) will be used. All signals can be represented by the sum of multiple sinusoidal waves at different amplitudes and frequencies via the Fourier Transform, this allows a known signal in the time domain to be represented in the frequency domain. The FFT is a set of algorithms that perform a Discrete Fourier Transform (DFT) in a computationally efficient manner, allowing fast examination of received signals. [33]

The Continuous Fourier Transform of an analogue signal represented by $X_a(t)$ is shown [34]:

$$X_a(F) = \int_{-\infty}^{\infty} x_a(t) e^{-j2\pi F t} dt \tag{2.36}$$

where:
$X_a(F)$ = Frequency domain representation
t = Time
F = Frequency

In order to obtain a digital representation of an analogue signal the signal is sampled at uniform intervals, this is shown mathematically:

$$x(n) = x_a(t) \mid_{t=nT} \tag{2.37}$$

where:
$x(n)$ = nth sample
n = Sample number
t = Time
T = Uniform time interval (sampling period)

Fig. 2.7 shows a graphical representation of the process. Each nth point represents the value of the sampled wave at a particular point in time defined by the sampling period.

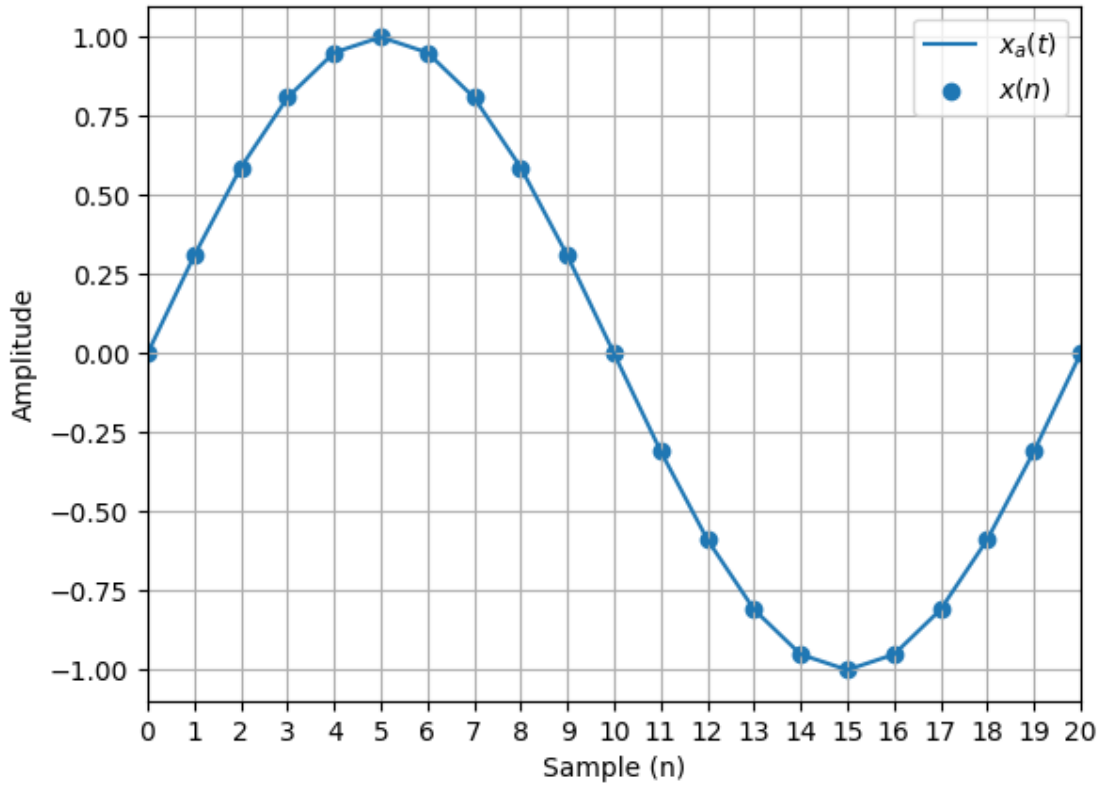

Figure 2.7: $x(n)$ samples of analogue wave $x_a(t)$

Because the sampled signal represented by $x(nT)$ from (2.37) is now a discrete sequence rather than continuous, in order to perform a Fourier Transform the DFT must be used [34]:

$$X(kF) = \sum_{n=0}^{N-1} x(nT)e^{-j2\pi kFnt} \tag{2.38}$$

where:

N = Number of samples
F = Spacing of frequency domain samples
T = Sample period in the time domain

From (2.38) the frequency domain representation of the sampled signal can calculated by an FFT algorithm.

In order to correctly produce an FFT plot many variables must be considered, the following sections will cover the necessary choices.

Dynamic Range

Dynamic range is defined as the difference between the smallest and largest signal that can be displayed at the same time. This is given by the differences between the noise floor and the highest power signal it is possible to receive with sending the instrument into compression. The following sections will show how other aspects of the FFT can affect the Dynamic range.

Sampling Rate

The sampling rate is a measure of how quickly samples of the observed signal are taken. Higher frequency signals must be sampled at a higher frequency in order to obtain enough points on the waveform, as shown in Fig. 2.7, to be able to accurately recreate the signal. The sampling frequency must be greater than twice the maximum frequency in the analogue signal $X_a(F)$, this sampling frequency is known as the Nyquist rate. The Nyquist frequency is half the sampling frequency, any frequency components in the sampled signal above the Nyquist frequency are aliased to lower frequencies, where they will be incorrectly shown on the FFT [34].

The sampling frequency also has affect on sample collection and processing time, as well as the resolution of the FFT, as discussed in the next section.

Resolution Bandwidth

Due to sampling, the frequency domain representation of a signal is spaced out in to a number of FFT 'bins' which contain the energy for all signals within that bin. This is referred to as the Resolution Bandwidth (RBW) and determines the narrowest bandwidth it is possible to resolve from the FFT.

RBW is determined by the number of samples taken and the sampling frequency as shown in (2.39) [34]. It can be seen that RBW can be adjusted to meet a specific requirement by changing the sampling frequency and number of samples in data collection.

$$RBW = \frac{1}{NT} = \frac{F_s}{N} \tag{2.39}$$

where:
F_s = Sampling frequency

From (2.39) it can be seen that the FFT has N bins, to calculate the Frequency of the nth bin of an FFT (2.40) can be used:

$$F_n = \frac{nF_s}{N} \tag{2.40}$$

where:
F_n = Frequency of nth point
n = Point n

Because the DFT is symmetrical around N/2, (2.40) shows the maximum frequency plotted is Fs / 2 when n = N/2 [34].

Fig. 2.8 shows an FFT conducted on sine waves at 100Hz and 95Hz. The solid line shows the trace when the RBW is set to 1Hz, it is possible to clearly identify peaks at the two separate frequencies. The dotted trace shows when the RBW is set to to 5Hz, the two signals now fall within the same FFT bin and are indistinguishable from each other.

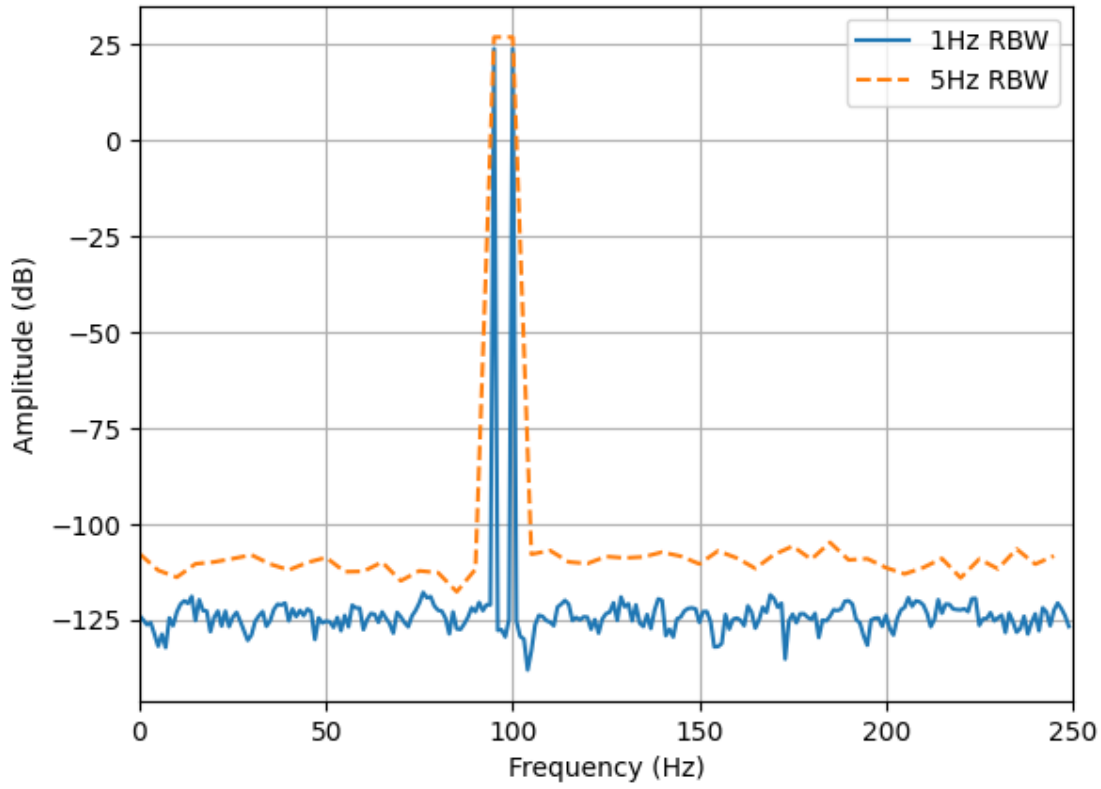

Figure 2.8: Showing the effect of changing RBW on FFTs

This shows the need to carefully select the parameters for the FFT based on the bandwidth of the signals to be observed and the likelihood of adjacent signals falling in to the same FFT bin.

From Fig. 2.8 it is also possible to see the effect changing RBW has on the noise floor of the FFT plot. As the bins become wider more of the noise energy now falls within each bin, resulting in an increase in noise floor which could obscure low power signals. Based on a known noise in dBm/Hz, the noise floor at a certain RBW is given by:

$$N_{RBW} = N + 10\log_{10}(RBW) \tag{2.41}$$

where:
N_{RBW} = Noise floor at a certain RBW (dBm)
N = Noise (dBm/Hz)
RBW = Resolution bandwidth (Hz)

This shows that lower RBW gives a lower noise floor and therefore a higher dynamic range. The trade off here is that increasing the RBW requires decreasing the sampling frequency and keeping the number of samples the same, or keeping the sampling frequency the same and increasing the number of samples taken. Reducing sampling frequency reduces the highest frequency it is possible to observe and increasing the number of samples increases the time taken for data collection (sweep time).

This means that selecting the correct RBW is compromise between the separation of adjacent signals to be observed, the frequency of those signals, the noise floor required and the required sweep time.

Windowing

The DFT assumes that any sampled signal is periodic over infinity [34]. The algorithm extends the sample by replicating it an infinite number of times, if the points where the samples meet introduce a discontinuity in to the signal, this can be seen in the FFT by the spectral lines spreading out from the line associated with the true signal, this is know as spectral leakage. This effect is mitigated by the practice of windowing. Figure 2.9 shows a hypothetical example considering a sine wave. The first plot shows a sine wave captured over a non-integer number of periods, so in the second plot, when the sample is replicated the points where the samples meet do not match up and the signal is no longer a sine wave, artificially introducing frequencies in to the signal that are not actually present. The third plot shows how windowing tapers the sample towards the ends, so when the samples are extended the discontinuity when they meet is reduced.

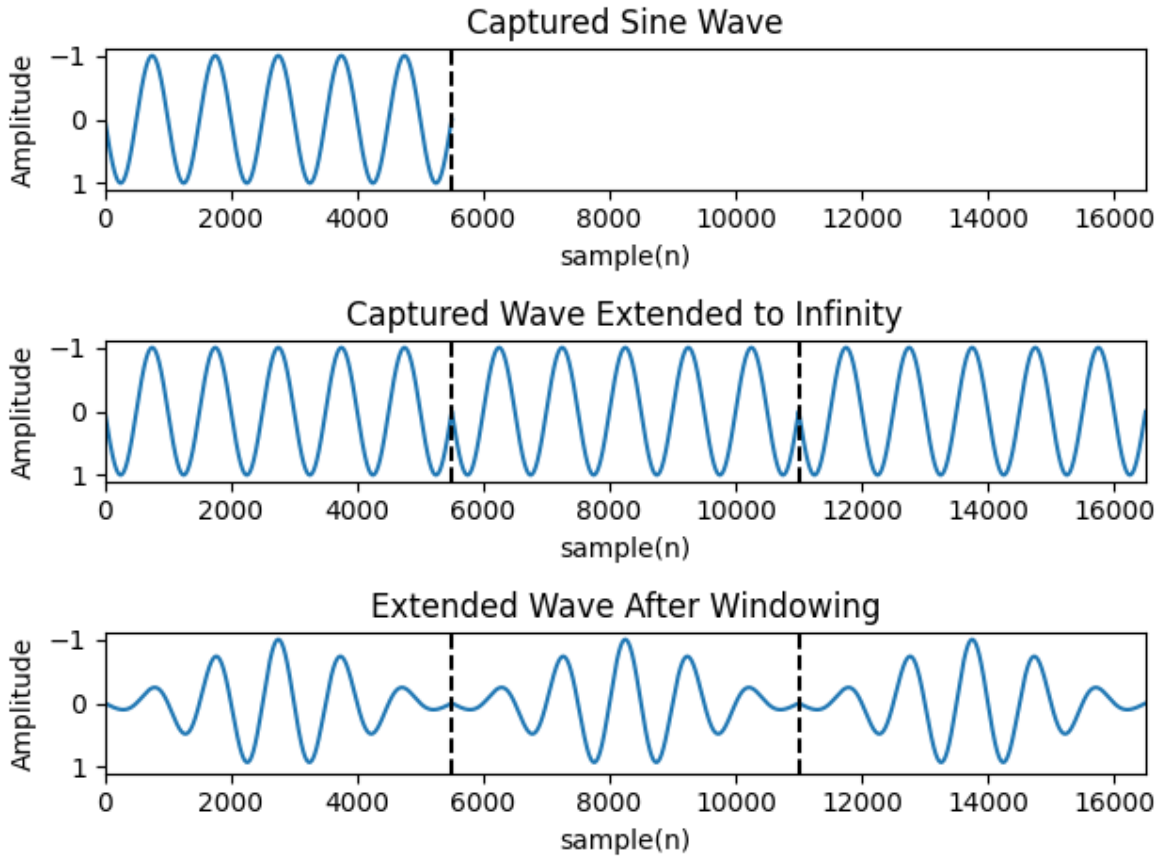

Figure 2.9: Captured sine wave extended with discontinuity and windowed

Fig. 2.10 shows some commonly available windows. The sampled signal is multiplied by one of these window functions before the FFT is conducted. Because the use of this technique reduces the amplitude of the sampled signal a correction factor must be applied to the FFT to compensate for the lost energy, this is known as processing loss.

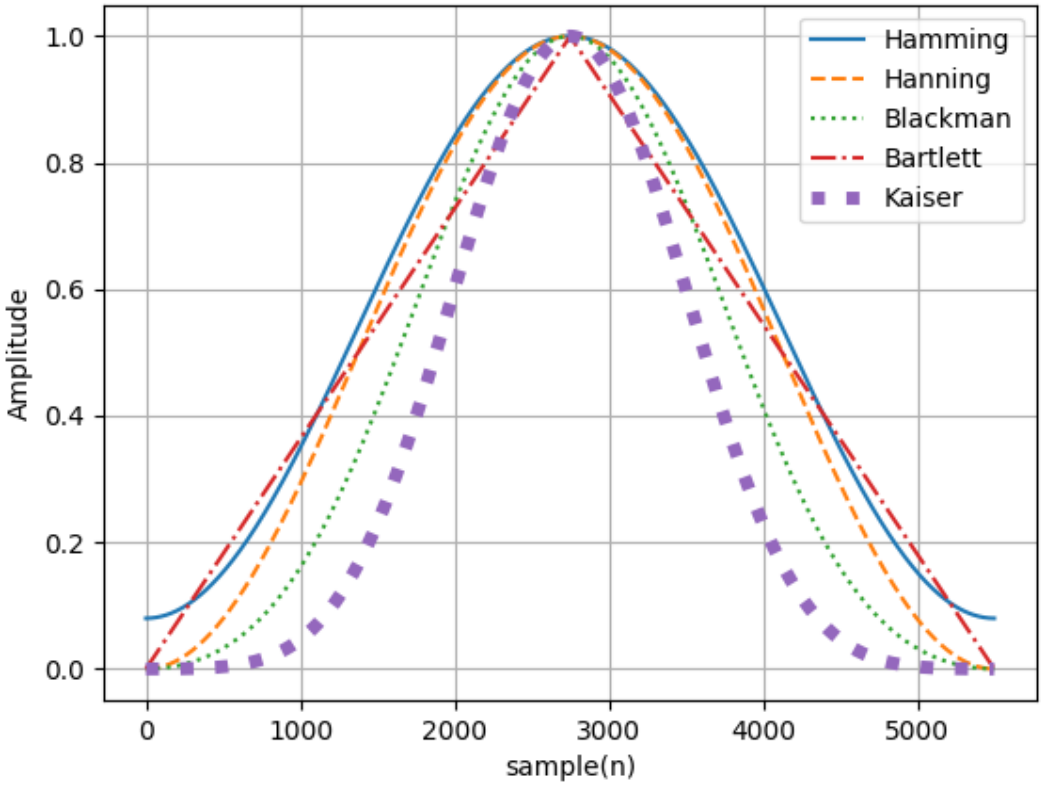

Figure 2.10: Examples of some windows available

Each window has different characteristics, and so should be chosen based on the signal to be observed. The Hanning window is often recommended for measuring broadband signals and noise. Therefore this is the window that is used in this thesis.

Averaging

Averaging can be used to improve an FFT. The Averaging can be applied in the time and/or frequency domains for different affects [34].

Time domain averaging reduces the noise floor of the FFT, by the amount shown here [34]:

$$Noise\ Floor\ Drop = 3dB \times \log_2(N_{avg}) \tag{2.42}$$

where:
N_{avg} = Number of averages

Fig. 2.11 shows the affect of taking 100 time domain averages on the FFT of a 100Hz sine wave. Equation (2.42) predicts that the noise floor will drop by 19.9dB. From the figure it can be seen that the noise floor has reduced from 4.9dB to -15.0dB, just as predicted. This shows that this technique will improve the dynamic range of the FFT. The figure also shows that while the noise floor is reduced the variance of the trace remains unchanged.

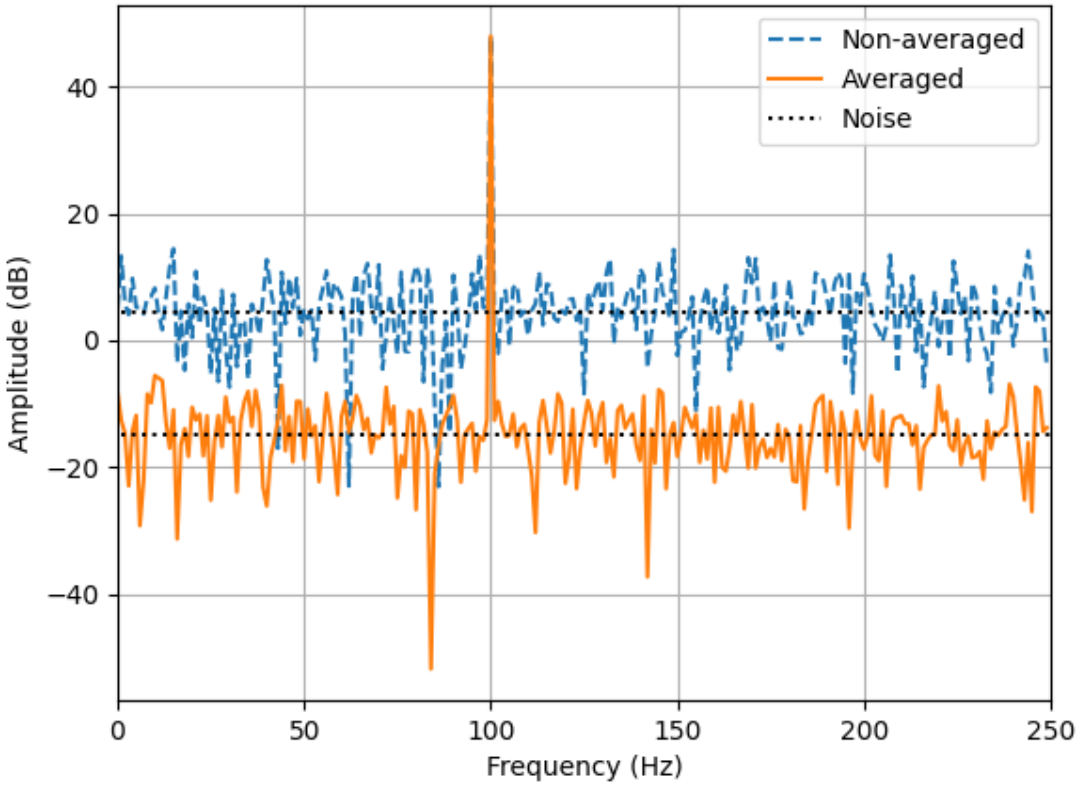

Figure 2.11: FFT showing 100Hz sine waves with and without time domain averaging

Averaging can also be applied in the frequency domain, i.e. to the trace of the FFT. Fig. 2.12 shows the effect of taking 100 frequency domain averages on the FFT of a 100Hz sine wave. The figure shows that the noise floor remains unchanged but the variance in the FFT trace has been reduced and now appears ‘smoother‘.

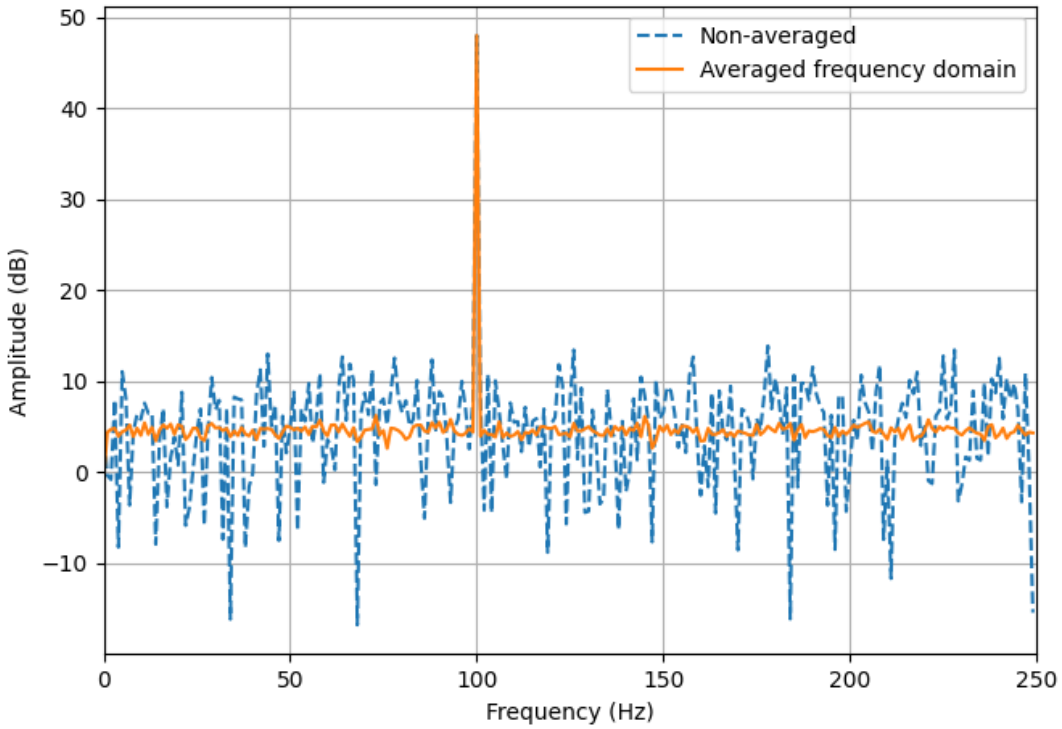

Figure 2.12: FFT showing 100Hz sine waves with and without frequency domain averaging

This shows that combining these two averaging techniques can provide a powerful tool for increasing dynamic range and readability for an FFT.

2.9 Antennas

In order to transmit and receive the necessary RF signals for the work in this thesis a number of antennas must be used, separate antennas will be used for the VHF and UHF band at both TX and RX. For the TX antennas size is not a limiting factor, because these antennas will remain in a stationary, secured position such as a rooftop. For the RX antennas size is very important because the measurement instrument to be designed will be required to be easily portable, in order to simulate a mobile IoT use-case. The wavelength for the utilised frequencies is 4.23m for 71MHz and 0.35m for 869.525MHz. A half wave dipole is therefore portable for the UHF RX, but not the VHF. In order to reduce the size of antenna needed a helical antenna will be used for VHF TX.

This section will describe the characteristic of antennas and provide a description of the antenna types to be utilised. All work in this Thesis will be conducted in the far field region, so the characteristics will be described in this region.

Radiation Pattern and Directivity

The radiation pattern of an antenna describes the shape of the radiated field produced by an antenna. Figure 2.13 shows a cross section of the radiation pattern of a dipole antenna, with its distinctive figure

of 8 shape visible in the XY plane. In 3d space this radiation pattern is torus shaped. Different antenna configurations have different antenna patterns, but because the antennas used in this thesis both display this type of pattern this is the one displayed here.

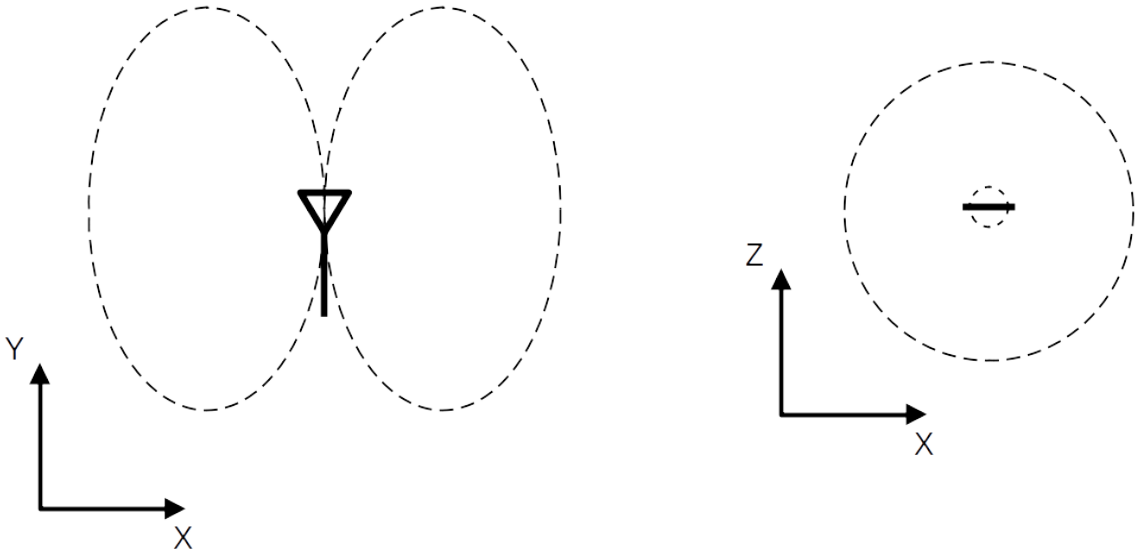

Figure 2.13: Cross section of the radiation pattern of a dipole in the XY and XZ directions

Directivity is related to the antenna pattern. A theoretical antenna which radiates its energy equally in all direction is known as an isotropic antenna, if figure 2.13 is examined it can be seen that this is not the case for this real world example. Directivity is the ratio of an antennas radiation in a specific direction, compared to the radiation of an isotropic antenna in that same direction [2], this is given by (2.43). Directivity is usually quoted in the direction of maximum radiation from the antenna.

$$D = \frac{U}{U_0} = \frac{4\pi U}{P_{rad}} \tag{2.43}$$

where:
D = Directivity
U = Radiation intensity (W/unit angle)
U_0 = Radiation intensity of an isotropic source (W/unit angle)
P_{rad} = Total power radiated (W)

Input Impedance

Antennas present an input impedance at their terminals for a specific wavelength, defined by the antenna dimensions and type. This determines the frequencies the antennas will usefully operate over.

Input impedance is made up of resistive and reactive components [2]:

$$Z_A = R_A + jX_A \tag{2.44}$$

where:
Z_A = Impedance at the antenna input terminals (Ω)

R_A = Resistance at the antenna input terminals (Ω)
X_A = Reactance at the antenna input terminals (Ω)

With the resistive component made up of the radiation resistance and the loss resistance, as seen in (2.45). Radiation resistance represents the amount of power radiated by the antenna, while loss resistance represents the amount of power lost as heat [2].

$$R_A = R_r + R_L \tag{2.45}$$

where:
R_r = Radiation resistance of the antenna (Ω)
R_L = Loss resistance of the antenna (Ω)

Matching networks are sometimes use the match the input impedance of the antenna to the impedance of the transmitter or receiver connected to it, allowing the transmission of power from one component to the other with minimum losses due to reflection. Reflection is discussed in more detail in section 2.2.

Antenna Efficiency

The efficiency of an antenna is a measure of how much of the energy presented to the antenna can be usefully radiated.

Firstly the radiation efficiency must be considered, this is given by the ratio of the power delivered to the radiation resistance over the power delivered to the radiation and loss resistance together [2]:

$$e_{cd} = \left[\frac{R_r}{R_L + R_r}\right] \tag{2.46}$$

where:
e_{cd} = Radiation efficiency

Total antenna efficiency can then be considered by looking at the amount of energy reflected at the antennas input due to impedance miss-matches, thus showing how much energy is conducted to the radiation and loss resistance. Impedance miss-matches can be different between different antenna and transmitter combinations, this figure would only remain constant if the antenna was being moved between different transmitters with terminals of the same impedance, for instance if both had 50Ω terminals. The reflection efficiency and radiation efficiency are combined to find the total efficiency [2]:

$$e_0 = e_r e_{cd} = e_{cd}(1 - |\Gamma|^2) \tag{2.47}$$

where:
e_0 = Total antenna efficiency
e_r = refection efficiency
Γ = Voltage reflection coefficient at the antenna input

Antenna Aperture

Antenna aperture is a measure of the amount of energy an antenna can capture from an incident RF wave. It is the amount of power transmitted to a load from a received RF wave of a specific power, by the receiving antenna. It is expressed as an area, which is of a size that is equivalent to that of an imaginary area that collects the same amount of power as delivered to the load from an RF wave of a specific power density [2]:

$$A_e = \frac{P_T}{W_i} \tag{2.48}$$

where:
A_e = effective aperture (m^2)
P_T = Power delivered to the load (W)
W_i = Power density of the incident wave (W/m^2)

Maximum antenna aperture can be related to directivity [2]:

$$A_{em} = \frac{\lambda^2}{4\pi} D_0 \tag{2.49}$$

where:
A_{em} = Maximum effective aperture (m^2)
D_0 = Maximum directivity

It is assumed by (2.49) that no losses are present in the antenna and it is connected to a matched load, if this is not the case then the maximum aperture is expressed in relation to directivity and antenna efficiency:

$$A_{em} = \left(\frac{\lambda^2}{4\pi}\right) D_0 e_0 \tag{2.50}$$

Gain

The gain of an antenna is related to its directivity and radiation efficiency. it is the amount of power transmitted in a specific direction by an antenna, compared to the power that would be radiated by a lossless isotropic antenna in the same direction. The maximum directivity describes the maximum amount of power that can be transmitted in a specific direction, compared to an isotropic antenna and the radiation efficiency specifies the loss of the antenna. So the gain in dB can be expressed as [2]:

$$G_0(dB) = 10 \log_{10}(e_{cd} D_0) \tag{2.51}$$

where:
G_0 = Antenna gain (dB)

Dipole Antenna

A dipole antenna is constructed from two straight wires, this thesis will consider the special case of a dipole which is half a wavelength long ($L = \lambda/2$). Fig. 2.14 shows a diagram of a half-wave dipole while Fig. 2.13 some a cross section of the radiation pattern produced by this kind of antenna.

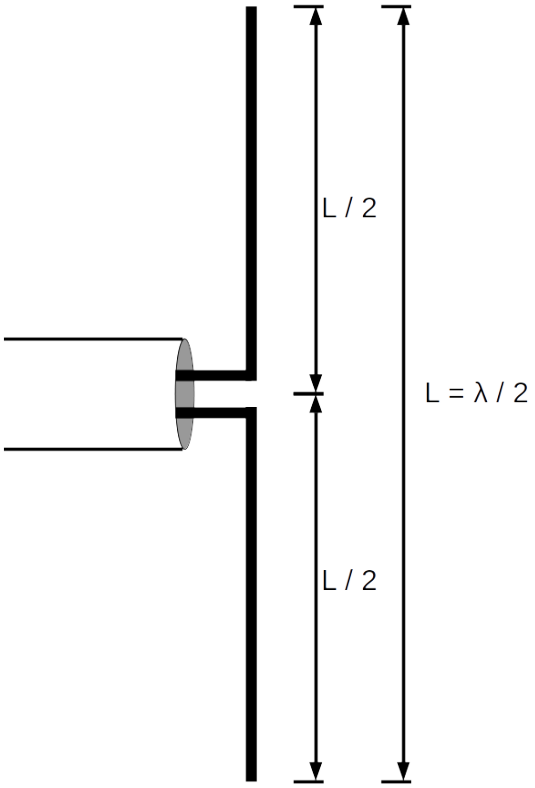

Figure 2.14: Diagram of a half-wave dipole antenna

Because extensive work and measurements have been conducted on this type of antenna, it is known that the maximum directivity, from (2.43) $\simeq 1.643$ (2.15dB) [2]. The input impedance of an half-wave dipole is also widely known [2]:

$$Z_A = 73 + j42.5 \tag{2.52}$$

The reactive component of the input impedance can be brought to 0 by slightly varying the length of the antenna. Depending on the radius of the wire used to construct the antenna the length is usually adjusted to between 0.47λ and 0.48λ, with larger radius wire requiring the length the be reduced more than smaller radius wire [2]. The input impedance is then close to the standard 50Ω or 75Ω impedance of readily available co-axial cables, making this antenna an attractive choice.

Helical Antenna

A helical antenna is constructed from a wire wound in to a helical shape, connected to a ground plane, Fig. 2.15 shows a diagram of this type of antenna. This type of antenna has the characteristics of a of a small loop and a small dipole, the ratio of which depends on the antennas dimensions. Helical antennas are popular in mobile communications due to their reduced size when compared to a half-wave dipole.

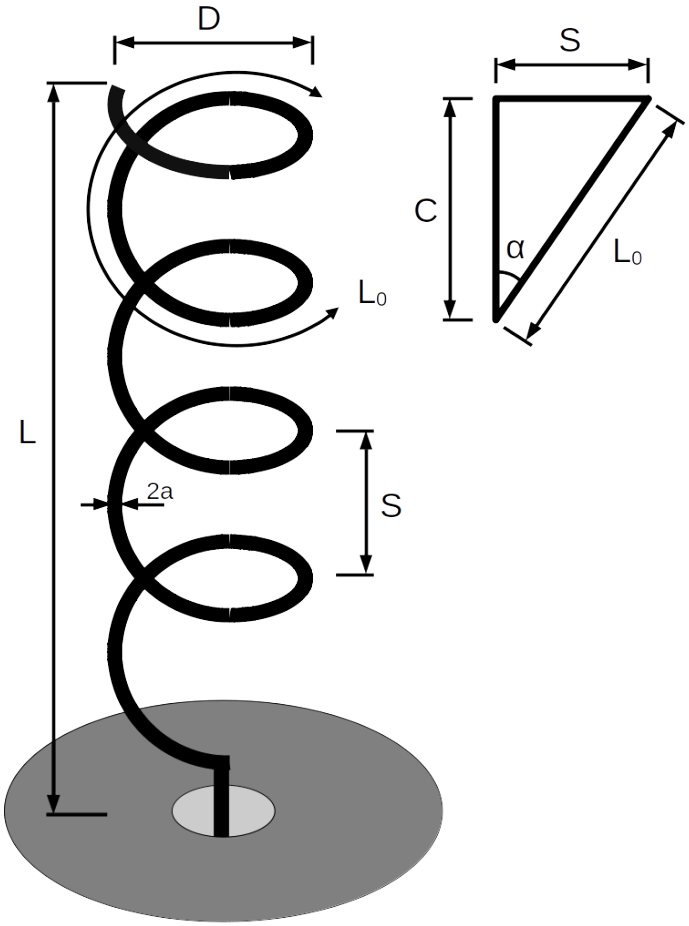

Figure 2.15: Diagram of an helical antenna with ground plane [2]

The antenna dimensions of an N turn helical are given by [2]:

$$L_n = NL_0 = N\sqrt{S^2 + C^2} \tag{2.53}$$

where:
L_n = Total Length of wire
N = Number of Turns
L_0 = Length of wire in each turn
S = Spacing between each turn
C = πD
D = Diameter of the turn

Pitch angle in give by (2.54), this gives a measurement of the relationship of the antenna to a straight wire or a loop. A pitch angle of 0° means the helix has been flattened to a loop antenna of N turns. A pitch angle of 90° means the helix has been reduced to a straight wire of length S. So a real helical antenna will have a pitch angle between 0° and 90° [2].

$$\alpha = \tan^{-1}\left(\frac{S}{C}\right) \tag{2.54}$$

where:
α = Pitch angle

A helical antenna can operate in either normal mode or axial mode. Axial mode produces an end-fire mode, highly directional radiation pattern emanating from the end of the helix. Normal mode produces a broadside radiation pattern that is similar to a dipole, in this thesis the helical antenna will be used in normal mode. Normal mode operation occurs when the dimensions of the antenna make $NL_0 << \lambda_0$.

The helical antennas far field radiation pattern is a superposition of the radiation pattern from a small loop and a small dipole. The ratio of the magnitude of each component is given by the axial ratio[2]:

$$AR = \frac{|E_\theta|}{|E_\phi|} = \frac{2\lambda S}{(\pi D)^2} \tag{2.55}$$

where:
AR = Axial ratio
E_θ = Electric field radiated by a short dipole (far field)
E_ϕ = Electric field radiated by a small loop (far field)

Radiation resistance of a normal mode helical antenna is approximately [28]:

$$R_r \approx \left(\frac{25.3NS}{\lambda}\right)^2 \tag{2.56}$$

This allows the number of turns and their separation to be chosen to give an approximate radiation resistance in a useful range. Directivity of the antenna is approximately 1.5 (1.76dB)[28], very similar to the directivity of an half wave dipole.

Chapter 3

Literature Review

This section will cover a review of the areas required to realise the work in this thesis. Section 3.1 covers a review of how path loss is calculated and the propagation models that are in current widespread use. Section 3.2 covers a review of studies performed to measure and understand path loss in different scenarios and environments, as well as what kinds of test beds are used to perform these studies. Section 3.3 covers a review of studies performed to measure and examine features of the RF spectrum. Section 3.4 covers studies that use SDR instruments to preform high quality scientific measurements.

3.1 Propagation Models

RF propagation is an important factor to consider when designing radio systems, knowledge of the propagation environment gives information which allows coverage and reliability to be considered.

Multiple factors affect RF waves and therefore multiple models are used to predict their propagation. Once transmitted, an RF wave encounters an environment which may cause the wave to be reflected, refracted, diffracted, scattered, attenuated or absorbed [28]. This can create many reflections of the wave at various different amplitudes, frequencies, delays and phases. These multi-path components can cause distortion when they arrive at the transmitter [35].

Discussed below are a selection of models which are used to predict the propagation of RF waves in different environments and circumstances. It is important to understand the propagation environment when planning a radio system, for instance when designing a cellular network this information will allow the position and density of base stations to be planned.

The commonly used propagation models discussed here can then later be compared to the real world readings taken as part of the study, where the models can then be validated for the required purposes or a new model developed.

Some models are based on theoretical concepts and others are based on empirical data from large scale studies. The models examined here predict path loss in dB, path loss is given by the difference between transmitted power and received power in dB. The definition of path loss is given by the ratio of transmitted power to received power at a given point [35], (3.1) gives the linear definition of this relationship and (3.2) gives the definition in dB:

$$P_L = \frac{P_t}{P_r} \tag{3.1}$$

$$P_L(dB) = 10\log_{10}\left(\frac{P_t}{P_r}\right) \tag{3.2}$$

where:
$P_L(dB)$ = Path Loss (dB)
P_t = Transmitted power (W)
P_r = Received power (W)

Fig. 3.1 shows the hypothetical relationship between path loss and distance, the red line shows how path loss measured in decibels increases with the log distance from the transmitter, the green lines shows a more realistic scenario where fluctuations to the path loss are caused by shadowing and multipath propagation components combining in constructive and destructive ways (slow and fast fading).

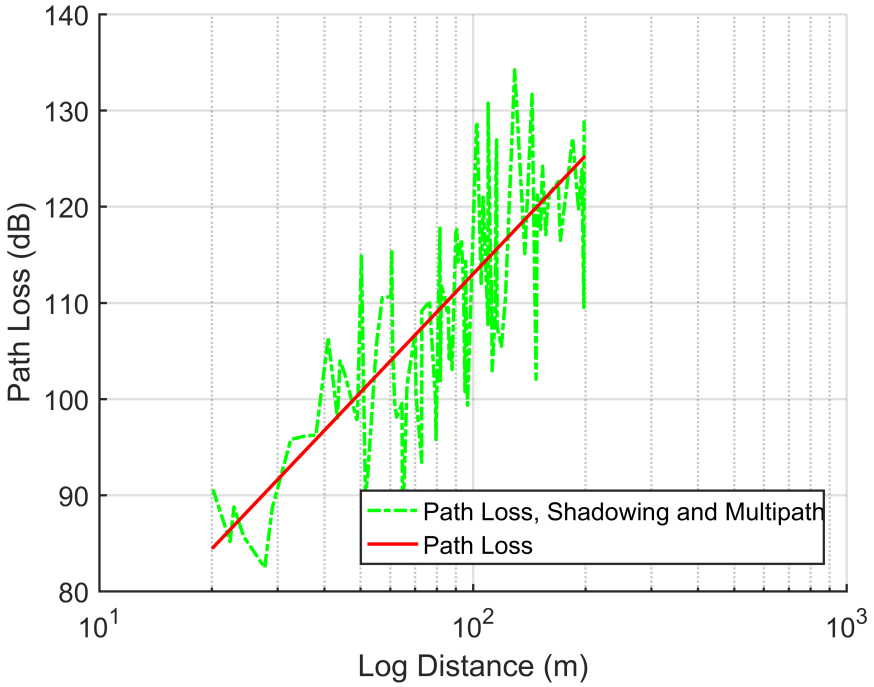

Figure 3.1: Path Loss, Shadowing and Multipath Against Distance

Free Space Path Loss

The concepts behind Free Space Path Loss (FSPL) are discussed in Section 2.3, this section shows how FSPL can be used as a simple model to calculate expected path loss in decibels. If the performance of the antennas are ignored, the free space path loss in dB can be found by [28]:

$$L_P = 10\log_{10}\left(\frac{P_t}{P_r}\right) = 20\log_{10}(f) + 20\log_{10}(r) + 20\log_{10}\left(\frac{4\pi}{c}\right) \tag{3.3}$$

where:
L_p = Path loss (dB)
P_r = Received power (W)

P_t = Transmitted power (W)
f = Frequency (Hz)
r = Distance (m)

Fig. 3.2 shows the predicted Free Space Path Loss of RF waves at 71MHz and 869MHz. It indicates a higher loss is expected at 869MHz compared to 71MHz.

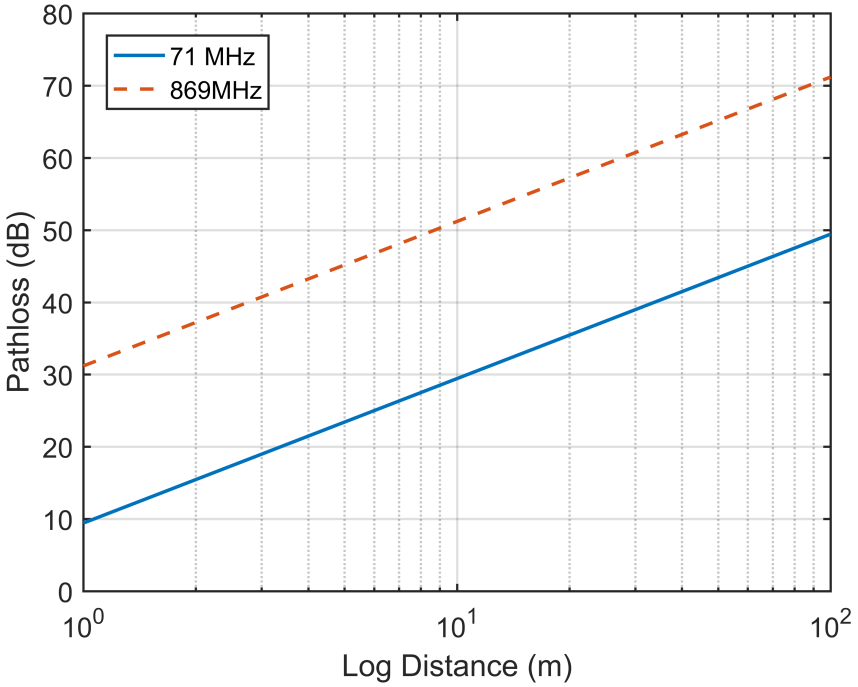

Figure 3.2: Free Space Path Loss Against Distance

Two Ray Model

In the two ray model it is assumed that transmitted RF waves reach the receiver via two separate paths. One path is a line of sight (LoS) ray, the other path is a ray reflected by the ground. These two rays are combined at the receiver and may cause constructive or destructive interference [28]. Fig. 3.3 shows a representation of this process.

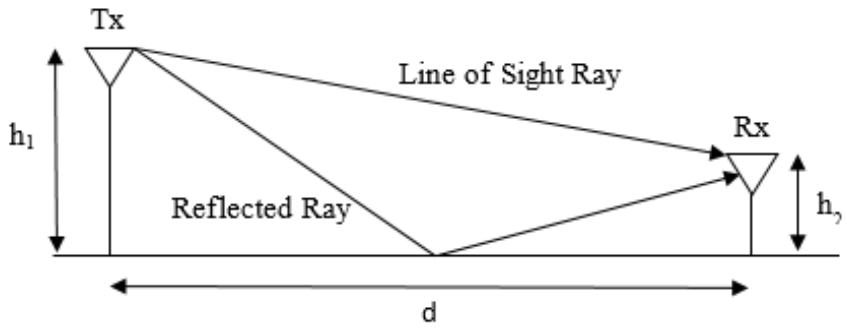

Figure 3.3: Two Ray Model

An area of multipath fast fading can be seen close to the transmitter as the LoS and reflected rays interfere with each other, this is the first Fresnel zone [28]. Beyond the first Fresnel zone RX power falls of at a steady rate.

First Fresnel zone distance given by [28]:

$$d_f = \frac{4h_1h_2}{\lambda} \tag{3.4}$$

Beyond the first Fresnel zone distance the path loss (assuming all power is reflected by the ground) is given by [28]:

$$L_p = -10\log_{10}\left(\frac{h_1h_2}{d^2}\right)^2 = 40\log_{10} d - 20\log_{10}(h_2h_2) \tag{3.5}$$

where:
d_f = Distance to the end of the first Fresnel Zone (m)
d = Distance between TX and RX antennas
h_1 = Height of TX antenna (m)
h_2 = Height of RX antenna (m)
λ = Wavelength (m)
L_p = Path loss (dB)

Okumara / Hata Model

The Okumara / Hata Model is one of the ITU models for mobile channels, it is widely use to predict propagation in urban areas [36].

This model is based on many readings taken by Okumara in Tokyo, calculations were then simplified by Hata [35]. There are different models for urban, suburban and rural environments, all of these models will be considered. The model is intended to cover the frequencies 150MHz to 1500MHz, base station heights of 30m to 100m and distances of 1km to 1000km [35]. Because this study will be conducted at a low frequency (for one band) with lower antennas and at a shorter distance it is not anticipated that this model will be very accurate in this case, but as it is an established model it will provide a good comparison.

Hata urban model is [35]:

$$\begin{aligned} L_{purban} =& 69.55 + 26.16\log_{10}(f_c) - 13.82\log_{10}(h_t) - a(h_r) \\ &+ (44.9 - 6.55log_{10}(h_t))\log_{10}(d) \end{aligned} \tag{3.6}$$

$$a(h_r) = (1.1\log_{10}(f_c) - 0.7)h_r - (1.56\log_{10}(f_c) - 0.8) \tag{3.7}$$

where:
L_{purban}= Predicted Path loss (dB)
f_c = Frequency (MHz)
h_t = Height of TX antenna (m)
h_r = Height of RX antenna (m)
d = Distance between TX and RX antenna (km)

Hata suburban model is [35]:

$$L_{psuburban}(dB) = L_{purban}(dB) - 2\left[\log_{10}\left(\frac{f_c}{28}\right)\right]^2 - 5.4 \tag{3.8}$$

Fig. 3.4 shows the predictions for path loss at 71MHz and 869MHz for the urban and suburban models. It indicates a higher loss for 869MHz than 71MHz and a higher loss for urban areas over suburban areas.

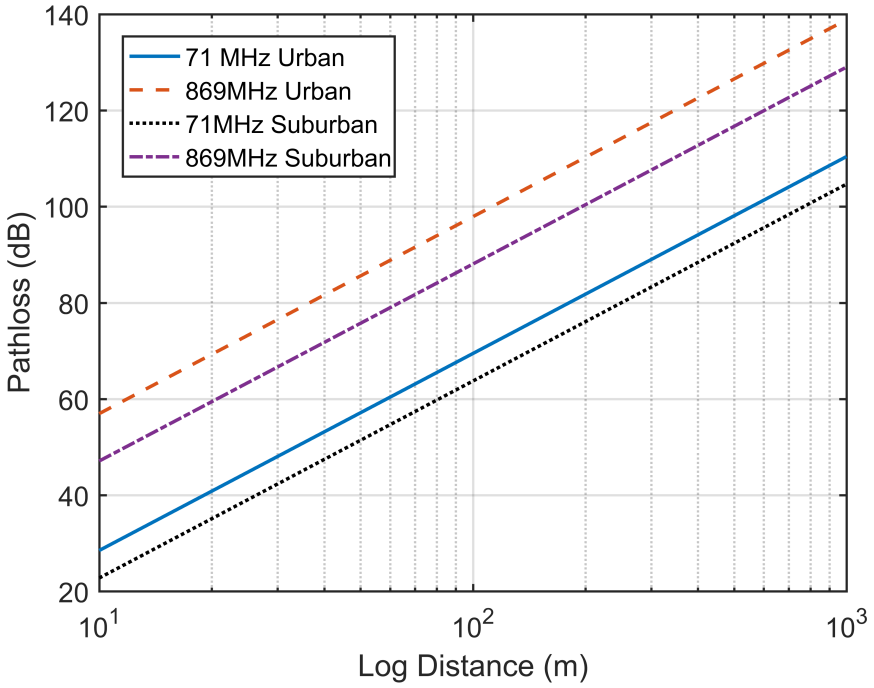

Figure 3.4: Hata Path Loss Against Distance

3.2 Propagation Studies

Many existing propagation models are based on having base stations with very high antennas and are only valid at longer distances, such as the Hata model only being valid for distances of 1km to 1000km with antenna heights of 30m to 100m. Many of these models for urban areas are based on mobile phone usage and so cover much higher frequencies (900MHz+) than the VHF frequencies examined in this thesis. The work in this thesis will cover shorter distances and lower antennas. The ITU provides important information regarding Propagation on their website, including models, data and details of atmospheric effects [37].

IoT applications often have antennas closer to the ground and are obstructed, often by the objects or people they are observing. Many propagation studies are examined here, with a focus on those conducted with IoT in mind. No IoT focused studies outside in an urban area with body height antennas were found at or around 70MHz. None of the studies covered the measurement of noise at the selected frequencies.

Analysis of Outdoor-to-Indoor Propagation at 169 MHz for Smart Metering Applications (Fuschini *et al.*) [38]

A smart meter focused outdoor to indoor propagation study was conducted by Fuschini *et al.* at a frequency of 169MHz, in order to match the European standard defined SRD band frequency range for smart meters of 169.4MHz to 169.475MHz [7]. A CW signal with an effective isotropic radiated power (EIRP) of 27dBm was used in the study, this is the maximum power level allowed by the standard [7]. TX was provided by an HP 8663A signal generator, connected via an amplifier to a Yagi antenna. A directional antenna such as this does not fit the smart meter use case and would have caused fewer reflections than a less directional antenna such as a dipole, this could affect the measured propagation. RX readings are provided by a Narda SRM3000 portable spectrum analyser connected to a 1/4 wave helical antenna.

The study investigates losses associated with propagation through the fabric of a building (building penetration loss) and losses associated with the positioning of the meter within the building, such as within a metal enclosure (installation loss). Readings of received power were taken at multiple stationary positions around the perimeter and inside the test building.

It was found that building penetration loss could be represented by a log-normal distributed variable, like the one used to represent shadowing, with an average of 7.5dB and a standard deviation of 4.5dB. Installation loss was found to be 7dB when installed within a metal grid and 13dB when installed in a basement.

Clutter and Terrain Effects on Path Loss in the VHF/UHF Bands (Faruk *et al.*) [39]

This paper describes a study in to the effects of urban clutter and changes in terrain elevation on propagation. It provides a comparison between real world measurements and prediction models from a statistical point of view.

Measurements were taken with an Agilent N9342C portable spectrum analyser connected to a whip antenna at a height of 1.5m, the location of each measurement was recorded with a GPS receiver. The transmitters used for the study were local TV transmitters with antenna heights of 100m to 340m and TX power of 1kW to 7kW. Frequencies used are in the VHF and UHF bands (89.3MHz, 103.5MHz, 203.25MHz, 479.25MHz, 615.25MHz, 559.25MHz and 695.25MHz). Measurements are taken over 15 different routes with distance of up to 33km within urban and countryside environments, the UHF transmitters are measured concurrently with each other, the VHF transmitters are measured separately from the UHF but concurrently with each other.

The models considered for comparison in this study are:

- **Hata Model:** as previously discussed in Section 3.1
- **COST 231 Model:** an extension of the Hata model to 2GHz (Unknown why this was used as the frequencies studied are not above the Hata model upper limit)
- **Egli Model:** a model covering propagation over irregular terrain
- **EC-33 Model:** a modification of the Hata model
- **Davidson Model:** an extension of the Hata model to distances up to 300km
- **ILORIN Model:** a modification of the Hata-davidson model to suit the area of Ilorin, Nigeria. This is the area where the study was carried out.

The readings taken were compared to the predictions of each model and the following statistical comparisons were used to analyse the differences between the two:

- **Prediction Error:** the difference between the measured signal strength at a certain distance and the predicted signal strength at that same distance
- **Mean Prediction Error:** the average value of the prediction error
- **Maximum Error:** the maximum prediction error
- **Standard Deviation Error (SDE):** the standard deviation of the prediction error

SDE for COST 231, Hata and ILORIN models were measured at between $\sim$17dB and $\sim$5dB for transmitters at 89.3MHz, 103.5MHz and 203MHz. SDE for Hata, COST 231, Davidson and ILORIN were measured at between $\sim$16dB and $\sim$5dB for transmitters at 479.25MHz, 615.25MHz, 559.25MHz and 695.25MHz. Egli and EC-33 models were dropped from the study because of their constant over estimation of path loss.

None of the models provided a good accuracy across the whole distance studied, different models were more accurate at different distances (ILORIN was best from 0-2km, Hata from 2.2-4km). None of the models were accurate close to the TX or in line of sight, this is because the models are not intended for this use and so this is expected. Clear correlation is shown with prediction error rising with terrain elevation. The authors found the ILORIN model to be the most accurate, this is not surprising as this model was developed specifically for the area the test was conducted in, based on empirical measurements. This shows that a model tailored to the environment it is used in performs the best in that environment, however it may not function well outside that area.

Detailed results for prediction error relating to each transmitter on each of the 15 routes are not presented in the paper, this leads to the conclusion that too many readings were taken to be clearly analysed and a greater focus on fewer routes may have been beneficial, however the overall results for SDE are presented for all the routes, which provides useful information. The paper focuses on the effect of terrain elevation and very little attempt is made to characterise urban clutter, which is also a source of prediction error in the results.

This paper covers transmission powers, distances and antenna heights well in excess of our proposed study, but it has been included as an example showing interest in VHF and UHF propagation measurements and showing possible ways to compare models and measurements.

VHF General Urban Path Loss Model for Short Range Ground-to-Ground Communications (Andrusenko *et al.*) [40]

This Paper describes a VHF (30MHz to 88MHz) propagation study at distances less than 1km. The authors found few models relevant to lower VHF or ground to ground communication. This study focuses on five scenarios, scenario 1 most closely matches the work that has been performed in this thesis:

Scenario 1: Outdoor line of sight RF Propagation in an Urban Canyon
Scenario 2: Indoor Propagation within the Same Building
Scenario 3: Indoor-to-Indoor Propagation between Two Buildings
Scenario 4: Indoor-to Outdoor Propagation
Scenario 5: Outdoor-to-Indoor Propagation

The TX consists of a Wiltron 68177B signal generator producing a CW signal connected to a high power amplifier and a whip antenna. RX readings are provided by an HP 8562A connected to a bandpass filter, LNA and whip antenna. This set up is again much more expensive than our proposed measurement system in Chapter 4. The RX set up was moved along predefined routes with multiple measurements of received power taken. The General Urban Path Loss (GUPL) model proposed in this paper is a modification of the log distance model with the addition of an attenuation constant, a variable exponent for the free space path loss and a floor attenuation factor to take account of the number of building storeys the RF signal has to pass through.

The model is based on a combination of the log distance model and the floor attenuation model found in the text book [1], which in turn takes information from Devasirvatham *et al.* [41] which was concerned with indoor propagation only. Devasirvatham *et al.* proposed a free space plus linear path attenuation model with an attenuation coefficient in dB/m to model the obstructions in an indoor environment based on measurements. Thus, the GUPL model is a mishmash of at least 3 different models and has become quite generic.

The GUPL model is given by (3.9):

$$GUPL(dB) = -10\log_{10}\left(\left[\frac{\lambda}{4\pi d_0}\right]^{\beta}\right) + 10n\log_{10}\left(\frac{d}{d_0}\right) + \alpha d + FAF \tag{3.9}$$

where:
$GUPL(dB)$ = Path Loss (dB)
λ = Wavelength (m)
d_0 = Reference distance in the far field region (m)
β = Power component
n = Path loss exponent
d = Distance between TX and RX (m)
α = Attenuation constant (dB/m)
FAF = Floor attenuation factor, based on the number of building floors a signal passes through (dB)

The values calculated for use in scenario 1 predictions are as follows, these setting will be used in comparison to readings taken in this thesis: power exponent = 2.2, path loss exponent = 1.8, attenuation constant = 0.06 dB/m, floor attenuation factor = 0. This gives the model a slightly higher roll off than the FSPL model (22dB/decade instead of the usual 20dB/decade). The number of measurements for some considered scenarios are as low as 3 measurements over a 90m TX to RX separation, this is a very low number to use for estimating model parameters in these scenarios. GUPL will be included in the comparisons to other propagation models in this thesis.

A UHF Path Loss Model Using Learning Machine for Heterogeneous Networks (Ayadi *et al.*) [42]

This paper describes a UHF (450, 850, 1800, 2100 and 2600MHz) propagation study in a rural, suburban and urban setting. Real world measurements are taken and these measurements are used to train a neural network to predict path loss. The neural network predictions are compared to more measurements and established propagation models.

The measurement set up consists of a signal generator and power amplifier for the TX. For the RX a commercial Berkeley Varitronics Systems Coyote Modular Receiver with a module for each band was

used at a cost of $6,000 for the receiver and $1,000 for each additional module [43]. Measurements were taken from a car driven on a predefined route with an antenna placed at a height of 1.5m. Antenna heights for the transmitter are from 17 to 35m, measurement distances from TX to RX is from 20m to 23km.

The models considered for comparison in this study are:

- **Standard Propagation Model:** based on the Hata model with additions for diffraction loss and clutter attenuation. The model includes a tunable corrective factor for each parameter
- **ITU-R P.1812-4:** an ITU propagation model covering distances from 0.25 to 3000km and frequencies from 30MHz to 3GHz with both TX and RX within a height of 3km from the surface of the earth

Measurements are fed in to a neural network as training data with the aim of producing a propagation model. The following statistical parameters used to validate the model:

- **Absolute Error:** the difference between the measured signal strength at a certain distance and the predicted signal strength at that same distance
- **Mean Absolute Error:** the average value of the Absolute error
- **Standard Deviation of the Absolute Error:** the standard deviation of the Absolute error
- **Minimum Absolute Error**
- **Maximum Absolute Error**
- **Correlation Factor** Between Model and Measurements

The neural network model was found to compare favourably to existing models, it was found to be more accurate but had slightly longer processing time and higher memory requirements.

Short-Range Low-VHF Channel Characterization in Cluttered Environments (Dagefu *et al.*) [19]

This is a study of short range, low VHF ($\sim$40MHz), near ground indoor and indoor-outdoor propagation at distances of up to 200m. The study on measurements of phase and channel transfer function. It is determined that the low VHF band is a good choice for low power, low data-rate and short range communications with simple channel models being able to reasonably predict real world performance.

LoRaWAN Network: Radio Propagation Models and Performance Evaluation in Various Environments in Lebanon (El Chall *et al.*) [44]

This study investigates RF propagation for outdoor (urban and rural) and indoor LoRaWAN deployments in the 868 MHz band. A commercial Pycom LoRa equipped transmitter was used as a portable TX source, a commercial Kerlink LoRa gateway was used for RX. The RX gateway provides received signal strength and signal-to-noise ratio as the location of the TX is moved within each of the different environments. Parameters for the LoRa transmission were set to provide the best sensitivity and therefore lowest data rate, making the measurements only applicable to best case scenario LoRa deployments. Measurements confirmed that the shadowing observed fits a Gaussian zero mean distribution, as

is widely used for modelling. New models were developed, including corrections for antenna height. A model for outdoor propagation was developed and is given in (3.10).

$$PL = 10n\log_{10}(d) + PL_0 + L_h\log_{10}(h_{ED}) + X_\sigma \tag{3.10}$$

where:
PL = Path Loss (dB)
n = Path Loss Exponent
PL_0 = Path Loss at Reference Distance
d = Distance between TX and RX (m)
L_h = Additional loss due to RX antenna height (dB)
h_{ED} = RX antenna height (m)
X_σ = Log Normal shadowing (dB)

Calculated parameters for outdoor campus environments are given as n = 3.12, PL_0 = 140.7, L_h = -4.7 and σ = 9.7. For Outdoor urban they are n = 4.179, PL_0 = 102.86, L_h = -6.3 and σ = 7.2. For outdoor rural they are n = 3.033, PL_0 = 111.75, L_h = -6.65 and σ = 6.4. This model will be compared to measurements taken in our study.

Survey of Available Experimental Data of Radio Wave Propagation for Wireless Transmission (Sarkar *et al.*) [45]

This paper studies short range GSM signal propagation at 900MHz and 1800MHz. Environments considered were urban, suburban, industrial and over water. A measurement campaign was conducted using GSM base stations for TX and GSM mobile phone handsets for RX, with measurement locations recorded by GPS. This study concludes that at the measured frequencies the propagation over ground is the dominant influence over path loss, with environmental concerns such as trees and buildings producing a secondary effect.

Improving RSSI-based Pathloss Models Accuracy for Critical Infrastructures: A Smart Grid Substation Case Study (Sandoval *et al.*)[46]

This paper examines path loss based on the received signal strength indicator (RSSI) of deployed IoT nodes of IEEE 802.15.4 standard at 2.4GHz. The study compares RSSI readings with readings from a VNA and quantifies and accounts for errors made by the nodes in RSSI readings. Once the errors were accounted for, readings from the RSSI were found to be in close agreement with VNA derived readings, showing that this method can provide a low-cost method of conducting propagation studies.

Empirical Study of Near Ground Propagation in Forest Terrain for Internet-of-things Type Device-to-device Communication (Hejselbæk *et al.*)[47]

This paper studies propagation for IoT devices deployed near to ground in a forested environment at a frequency of 917.5MHz. Measurements were found to be in close agreement to predictions made by the Two Ray Model when corrected for clutter loss. Measurements also showed agreement with a model previously proposed by Tewari *et al.*[48]

Securing On-body IoT Devices by Exploiting Creeping Wave Propagation (Wang *et al.*) [49]

This paper uses an on body to on body device propagation study to investigate and improve the security of IoT devices, showing further uses for IoT propagation studies.

Conference Papers

A number of conference papers discussing propagation studies of IoT or IoT-like situations were identified. These papers all followed similar structures, first several readings of signal strength are taken, then converted in to path loss measurements and compared to existing models. The log distance model is then modified to fit the readings taken.

Some of these papers are summarised in Table 1 below to show the general interest of the IoT research community and the in propagation studies at various frequencies and in various terrains.

Author	Title	Frequencies covered (MHz)	Environment	Equipment	Where Published	Key Findings
Oraibi et al. [50]	Empirical Path Loss Model for Vehicle-to-Vehicle IoT Device Communication in Fleet Management	2400	Vehicle to Vehicle	Commercial XBee IoT Nodes	16th Annual Mediterranean Ad Hoc Networking Workshop (2017)	2-Ray model gives better predictions in this scenario than FSPL. Proposes a new model for Vehicle to Vehicle propagation that gives similar results to the 2-ray model. New model includes a path loss exponent of 2.2 to 2.8 and log normal shadowing of 7.4 to 12dB standard deviation depending on the position of the TX and RX in the vehicle
Stewart et al. [51]	Internet of Things - Propagation Modelling for Precision Agriculture Applications	2400	Outdoor Rural	Full Wi-Fi network set up with supporting infrastructure	Wireless Telecommunications Symposium (WTS) (2017)	New propagation model proposed for rural areas via analysis of real world measurements. Model for dense vegetation: $Att_{ECOMESH} = 0.01f^{-1.6}d^{-0.776}$ Model for area with trees and pathway: $Att_{ECOMESH} = 0.002f^{-0.13}d^{-2.182}h^{-0.766}$ Where f = frequency, d = distance and h = height of access point
Cheu et al. [52]	RF Propagation Through Vegetation with Time-Varying Moisture	3000-4000	Outdoor Rural	Horn Antenna, Network Analyser	Radio and Wireless Symposium (2016)	A transmission environment consisting of wet grass will result in higher power at the RX than if the grass is dry, possibly due to a waveguiding effect
Boksiner et al. [53]	Validation of an Analytical Urban Propagation Model	328, 916, 1790	Outdoor Urban	Signal Generator, Spectrum Analyser, Laptop, Field Strength Meter	Military Communications Conference, MILCOM (2016)	Real world measurements are compared to a computer simulation of propagation (via ray tracing), with the model found to give similar predictions to the actual measurements. Actual measurements gave a model of: $P(R) = 144.8 + 53.9\log_{10}(R)$ Where R = distance in km Shadowing standard deviation is 4.9dB
Young et al. [54]	Radiowave Propagation in Urban Environments with Application to Public-Safety Communications	430, 750, 900, 1850, 2400, 4900	Outdoor Urban, Outdoor to indoor	Commercial Portable Transmitter, Spectrum Analyser	IEEE Antennas and Propagation Magazine (2014)	The received power detected inside a building decreases with increasing signal frequency

Table 3.1: Summary of Conference Papers

3.3 Spectrum Measurement Studies

In order for this thesis to provide detailed information regarding the RF spectrum at 70MHz and comparisons at 868MHz in an IoT use case, measurements will be conducted. This section focuses on studies which cover measurements made of RF spectrum or studies that could facilitate further measurements.

A Histogram-Based Segmentation Method for Wideband Spectrum Sensing in Cognitive Radios (Bao et al.) [27]

This paper describes the development of an algorithm for automatic radio spectrum segmentation to identify in use sub bands. The spectrum is first split up in to segments defined by the boundary of each sub band, then each sub band is analysed. This technique is intended to be used to determine which sub bands contain a signal and which do not. This method could be used to divide the spectrum to aid in making measurements of the key features of the sub bands, rather than just find if they are in use or not. Fig. 3.5 below shows a representation of the idea of segmentation aided measurement, using data collected for this thesis.

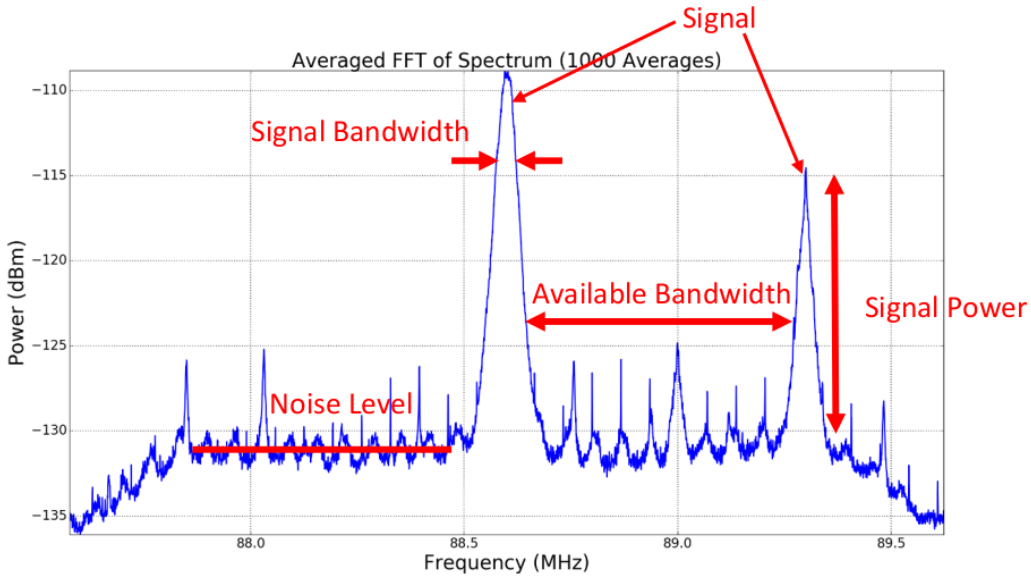

Figure 3.5: Representation of the Segmentation of Sub Bands Idea

The method described in the paper comprises the following steps:

- Obtain an estimate of power spectral density (PSD)
- Find each local maximum reading in the PSD with a value that exceeds a specific level. This level is chosen based on the minimum bandwidth considered for the sub-bands
- Segments that lay within a predefined range of the maxima are rectified (this seems to be intended to produce a smoother PSD graph, thus making it easier to analyse changes within the slope of the graph)
- The slope of the rectified PSD is examined to find a boundary. A boundary is placed where a minimum between 2 segments is found.

This algorithm was tested in the paper on emulated signals produced by a signal generator.

The method was implemented with a personal computer running MATLAB. In testing a signal analyser is used to measure the power spectral density and a signal generator is used to produce a number of different emulated signals at approximately 900MHz with different modulation schemes. Gaussian white noise is added to the emulated signals. Tests of the method were run 100 times determine if the algorithm could find the in-use bands within the emulated signal. The method was found to be successful for most outcomes, with some failures for when 2 signals with vastly different roll off factors are within the same PSD.

The following test scenarios were used on a simulated spectrum that covers 20MHz

- Scenario 1: 4 signals are included in the test spectrum with a phase shift keying (PSK) modulation. The boundaries between the signals were successfully detected with a standard deviation of between 0.01MHz and 0.11MHz over 100 tests when compared to the programmed values of the simulation.
- Scenario 2: 4 signals are included in the test spectrum with an orthogonal frequency division multiplexing (OFDM) modulation. The boundaries between the signals were successfully detected with a standard deviation of between 0.01MHz and 0.19MHz over 100 tests when compared to the programmed values of the simulation.
- Scenario 3: 2 signals are included in the test spectrum. The first is a wideband signal with a high roll off factor, the second is a narrowband signal with a low roll off factor. The width of the narrowband signal was reduced from 4.8MHz (76% successful boundary detection rate, standard deviation of 0.04MHz to 0.19MHz) to 2.4MHz (90% successful boundary detection rate, standard deviation of 0.03MHz to 0.31MHz) then 1.5MHz (88% successful boundary detection rate, standard deviation of 0.03MHz to 0.45MHz), 1.2MHz (92% successful boundary detection rate, standard deviation of 0.03MHz to 0.67MHz) and finally 0.6MHz (51% successful boundary detection rate, standard deviation of 0.03MHz to 0.39MHz)

This method was compared to wavelet transform based segmentation methods and found to be more computationally efficient than other methods while being comparable in successful detection of used spectrum.

A Generic Measurement Setup for Implementation and Performance Evaluation of Spectrum Sensing Techniques: Indoor Environments (Yarkan) [26]

This paper describes a study evaluating the performance of energy detectors in spectrum sensing. It describes a measurement set up and a test plan that could be applicable to the testing of many different techniques.

The measurement set up consists of a signal generator used for the TX, a R&S TSMQ radio network analyser was used to receive and digitize RF signals in to IQ data which is fed in to laptop for processing. This set up therefore allows for the SDR benefit of re-programmability. The RX set up is placed on a moveable cart to allow for different scenarios such as line of sight, non-line of sight and different shadowing characteristics to be investigated. The set up in this paper is confined to indoor use only, it uses mains electricity and is difficult to move.

Measurements are taken in two main sections, first with a stationary TX and RX, secondly with a stationary TX and a moving RX. Line of sight, non-line of sight and heavily shadowed scenarios are considered, with the moving set up considering transitions between the scenarios. The probability of detecting the transmitted signal is analysed, but more in-depth analysis of the spectrum is not provided.

Two forms of energy detectors were tested:

1. Radiometer: records the energy of a received signal over a set amount of time. This energy is then compared to a predefined threshold in order to make a decision on the possible presence of an unknown signal.
2. Second Order Detector: received signal is filtered, full wave rectified, amplified and correlated. The mean output of this process is used to make a decision on the possible presence of an unknown signal.

A second order detector was found to perform better than a radiometer, however the radiometer was found to be more computationally efficient.

Indoor Radio Noise Long-Term Variation in Medium Wave Band Based on Measurements (Landa et al.) [55]

This paper describes a study measuring the variations in indoor noise levels at frequencies below 2MHz over multiple days with readings taken 5 years apart. Results are compared to ITU-R P.372 predictions for outdoor noise. ITU-R P.372 is based on measurements taken over 30 years ago, so this paper attempts to verify these measurements are still valid.

Measurements are taken with a spectrum analyser connected to a computer. They are taken at a bandwidth of 9kHz at the frequencies 1359kHz, 1720kHz and 1910kHz. These were chosen because they are not currently being used for local radio services. Measurements were taken in 2008, 2010 and 2012 over periods of up to 16 days. RMS values of noise are averaged at each location and variations between different years are analysed and compared to predictions.

Indoor noise was found to be higher than ITU predictions for outdoor noise. Noise was found to vary from year to year with no clear reason.

Although this study is not at a frequency comparable to the frequencies studied in this thesis, it shows a current interest in measuring how RF noise has changed in the modern urban environment.

3.4 SDR Instrument Studies

This section focuses on studies using SDR to produce measurement instruments. Through their high-precision measurements of sine and pulse reference signals, Andrich *et al.* [56] have shown that it is possible for an SDR instrument to provide highly accurate readings, surpassing commercially available lab equipment.

SDR instruments have also been used to test ways of characterising RFID tags [57] [58], locating non-cooperative superheterodyne radio receivers [59] and to evaluate algorithms for Blind Wireless sensing [60].

Modular Software-Defined Radio Testbed for Rapid Prototyping of Localization Algorithms (Goverdovsky *et al.*) [61]

This paper describes an SDR based testbed designed to test and facilitate the development of localisation algorithms. Because of the reprogrammable nature of SDR it is possible to deploy multiple different algorithms on the testbed hardware developed, with no hardware changes required, only software.

The testbed comprises multiple Universal Software Radio Peripheral (USRP) boards from Ettus Research (part of National Instruments), each with its own antenna. The boards are synchronised and connected to one PC. The Testbed is modular and designed to be easily expandable or otherwise reconfigured. This is an example of the inherent re-programmability on an SDR and demonstrates how this testbed could be useful across many future localisation algorithm development exercises.

Multiple existing direction finding algorithms were successfully implemented on the testbed, including single source, multiple source and low power. Localisation was able to be performed by the test bed with an rms error of 2.14° for a single source, 2.49° for two sources and 3.36° for three sources. Some failures

were found in multiple source tests when sources were brought with 15° of each other the algorithms could not differentiate the sources.

This work shows that there is an interest in low cost, flexible, reconfigurable measurement systems / testbeds.

Low-cost Real-time Virtual Spectrum (Bilski *et al.*) [62]

Bilski *et al.* [62] produced a real time virtual spectrum analyser using software defined radio techniques within National Instruments (NI) LabVIEW environment and propitiatory NI hardware. However, this system wasn't designed for portability and still used expensive hardware. LabVIEW was also used by Schmidt *et al.* [63] and Soghoyan *et al.* [64] to create SDR GPS receivers which allow rapid prototyping of new GPS techniques. The general use of LabVIEW is now widely accepted in the automatic test equipment community, this shows the value of an SDR instrument and the willingness of the community to adopt them.

3.5 Summary of Review

All the identified propagation studies involved the use of very expensive equipment, with some of the portable spectrum analysers used costing up to £25,000 when new. Some of these analysers can measure frequencies up to 22GHz, which is far in excess of the frequencies required. Cost and complexity savings could be made in a designed SDR instrument by reducing this frequency range to focus on the IoT frequencies of interest. Table 3.2 shows a comparison of the spectrum analysers used in the listed studies as well as the one used in this study to validate the readings of the SDR instrument developed in chapter 4.

Make	Model	Frequency Range	DANL (dBm/Hz)	Cost (New)	Study
Narada	SRM3000	100kHz to 3GHz	-151	£11,000	Fuschini [38]
Agilent	N9342C	100Hz to 7GHz	-164	£8,500	Faruk [39]
HP	8562A	1kHz to 22GHz	-130	£25,000	Andrusenko [40]
Anritsu	MS2712E	9kHz to 4GHz	-162	£6,500	This Thesis

Table 3.2: Comparison of the commercial Spectrum Analysers used in the identified studies

Certain requirements for a propagation study become evident from examining the identified studies. The studies measure received signal intensity, usually of a CW signal, no multipath readings are taken for example to measure delay spread. Readings must be taken at a number of locations across a chosen area. So the designed instrument must be capable of recording a measurement of intensity and frequency of a signal along with the location the measurement is made at. The process should be automated as far as possible in order to reduce the time taken to perform a study.

None of the studies or models reviewed covered the frequencies, distances and use case of the work contained in this thesis, showing a clear niche for this work. Studies did show that it is possible to use SDR instruments to take high quality measurements, although none covered an instrument like the one developed in this thesis.

Chapter 4

SDR Based Instrument Development

The work in this chapter allows an SDR instrument to be used to replace a bulky and expensive spectrum analyser for RF field measurements. Using COTS equipment a low cost, portable SDR instrument for measuring RF propagation has been created and tested. The instrument described in this chapter is designed to meet the use-case of performing an urban propagation study in the repurposed VHF band and UHF SRD band in a fast and low cost manner. Design of the hardware and software is discussed, as well as the calibration of the instrument. Results of a test propagation study are given for the completed instrument.

This chapter describes work published by the author in a conference paper [3] and a journal paper [4].

4.1 Instrument Description

For the instrument discussed in this chapter both hardware and software will be considered. The instrument will consist of 3 parts: hardware; on-device processing software; and post processing software. Due to the licence granted by Ofcom for this work the frequencies examined by the instrument will be 869.525MHz in the SRD band and 71MHz in the newly re-purposed band. However, due to the use of the RTL-SDR device the instrument could be used to investigate any number of frequencies from 25MHz to 1750MHz. While the RTL-SDR could support broadband readings by using the developed program to sweep the local oscillator, since IoT transmissions are regulated to bandwidths much smaller than the 2.048MHz bandwidth that it is possible to realise without sweeping, it was decided that broadband readings were unnecessary. The requirements for the instrument are as follows:

- Dual Band - The instrument must be able to record measurements at both 71MHz and 869.525MHz in quick succession in order for the two bands to be studied at near the same time and location. Assuming an average walking speed of 1.3m/s measurements should be taken within approximately 2s to keep the readings within 2.6m of each other, this allows measurements to be close together but does not allow multiple measurements to be taken over one wavelength, so measurement of fast fading would not be possible.
- Portable - The instrument, including antennas, must be light and compact enough for a person to carry unaided, allowing the instrument to be carried through all pedestrian accessible parts of an urban test area, in the same way an IoT device might be carried.
- Low cost - As shown in Table 3.2 the equipment for a propagation study is extremely expensive, this limits who can perform a study. Where possible COTS parts will be used in this instrument

in order to reduce costs and make the system accessible to more people such as universities and small businesses.

- Automated - Once activated the instrument should require no action from the user to collect measurements, reducing complexity and therefore speeding up the process of conducting a propagation study. This includes the instrument detecting and recording its own location, via GPS, along with measurements.

In order to save time and money, cost and complexity savings will be made by focusing only on the frequencies and bandwidth of the IoT signals that are of interest. The spectrum analyser used in the identified studies, listed in Table 3.2 are able to operate up to multiple GHz and produce wideband measurements, but this holds no benefit when all the signals of interest are in the MHz range and have a narrow bandwidth. It is therefore evident that an instrument with this focus will lead to significant savings.

Because of the automated and portable nature of the instrument it is envisioned that many hundreds of measurements can be made quickly across a large area, providing as much information as possible for analysis. Fig. 4.1 shows the assembled instrument.

Figure 4.1: Picture of the SDR instrument as realised

4.1.1 Hardware

The key enabling technology for this instrument is the COTS RTL-SDR device produced by NooElec, which is based on a USB DVB-T television receiver for a PC. The device contains a Realtek RTL2832u demodulator which can convert received signals to an in-phase and quadrature (IQ) data format, it is this ability that allows this device to be used as part of a low cost SDR system. The RF front end of the device uses a Rafael Micro R820T2 RF tuner IC with a frequency range of 25MHz to 1750MHz. A Temperature Compensated Crystal Oscillator (TCXO) with a frequency stability of 0.5ppm is also included. The cost of this device is approximately £25 [65]. Drivers are available for the Linux and

Windows operating systems, with MATLAB and Python supporting programming for the device. Fig.4.2 shows an overview of the architecture of the entire SDR instrument, including the internal functions of the RTL-SDR device.

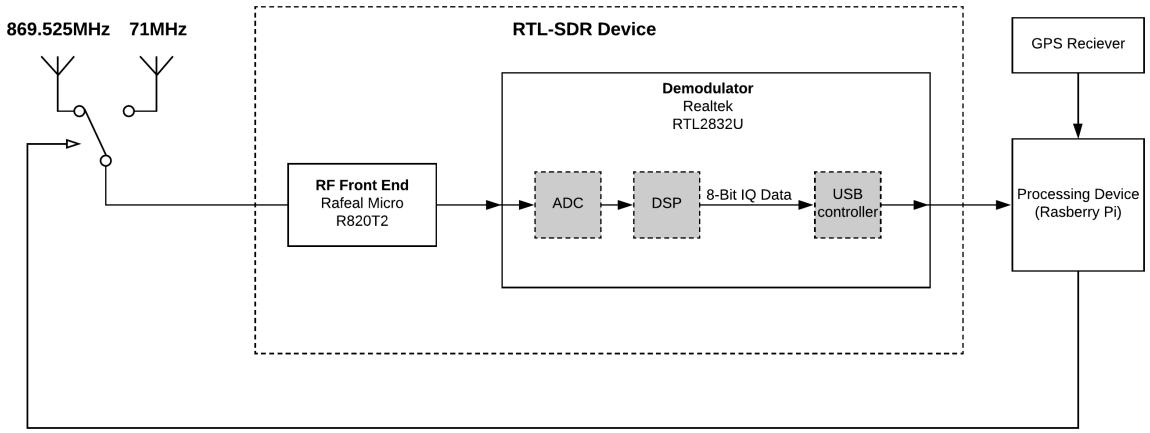

Figure 4.2: Architecture of the SDR instrument including the internal arrangement of the NooElec RTL-SDR device

A Raspberry Pi (RPi) model 3B is used as the processing and control device for the instrument. This COTS device features a 1.2GHz quad core 64-bit CPU and 1GB of RAM [66], allowing it to easily meet the expected computational requirements. The RTL-SDR device and other peripherals can be connected and controlled via the 4 USB ports. General Purpose Input and Output (GPIO) pins on the RPi can also be used to control other devices via user created programs. The RPi is small and lightweight with low power consumption requirements, making it ideal for use in a portable instrument. The RPi costs approximately £35.

The RPi requires a power source capable of providing up to 2.5A at 5V via USB, this power source will also power the RTL-SDR and GPS dongle via the RPi. In order to provide portable power a COTS mobile phone power bank type battery was selected at a cost of approximately £30.

In order to automate the collection of location data for the instrument when a measurement is taken, GPS functionality has been implemented via a COTS USB Dongle using the Ublox UBX-M8030 chipset connected to the RPi, costing approximately £20.

Because measurements of two bands are required and the design of a dual-band receiver (as shown by Liu [67]) is outside the scope of this thesis, in order to conduct measurements of both bands of interest in quick succession a switch between two antennas, with each antenna suited to a specific band, has been created. The GPIO connector on the RPi is used to control an RF switching circuit, with switching instructions issued automatically by the control software on the RPi. A sleeved dipole is used for 869.525MHz measurements and a helical antenna is used for 71MHz measurements in order to keep the antenna size appropriate for pedestrian usage.

The total cost of the COTS parts in the SDR based instrument is approximately £110, compared to £6,500 for the Anritsu MS2712E portable spectrum analyser used to take comparison readings in this study.

4.1.2 On-System Measurement Algorithm

Data and initial measurements are collected in the field by the SDR instrument, with the results being saved for later post-processing into path loss information. The on-system measurement algorithm is implemented using the Python programming language. Fig. 4.3 shows the output of the algorithm at one frequency for one sampling period with the instrument fed from a signal generator emitting -95dBm at 869.525MHz. A large peak can be seen at the center of the figure, which has been detected at a frequency of 869.525MHz and the amplitude of this peak is recorded as -95.3dBm. A smaller peak can be seen to the right of the large peak, this is produced by DC leakage from the RTL-SDR and is ignored by the algorithm.

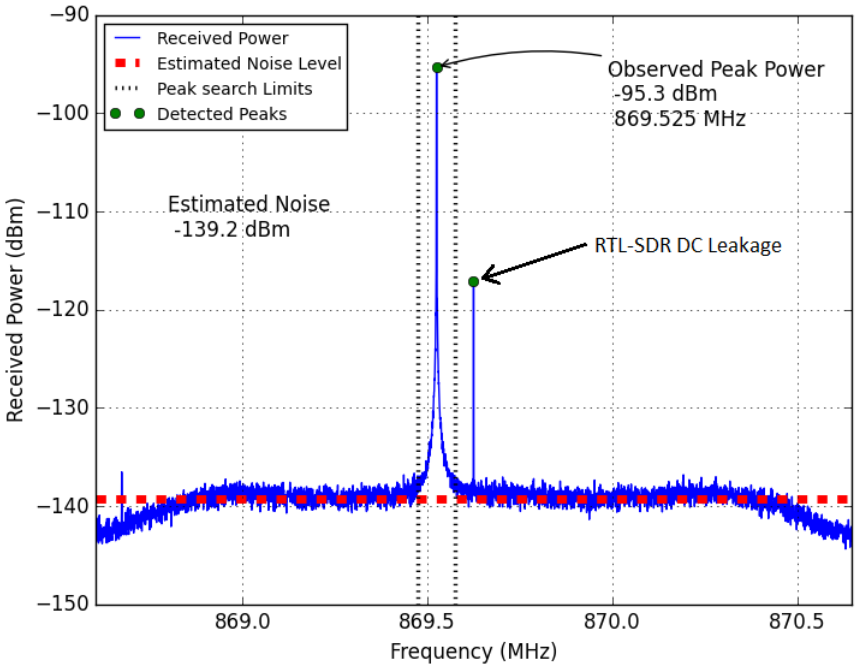

Figure 4.3: An annotated example of an RF signal (produced by a signal generator) received during one sampling period by the SDR instrument.

The algorithm can be thought of in two stages, 1) data is collected and then 2) initial measurements are made of noise and detected peak frequencies and amplitudes.

Fig. 4.4 shows the method of the data collection stage for one frequency. The algorithm first controls the antenna switch via the GPIO outputs of the RPi, selecting the appropriate antenna for the current measurement.

GPS co-ordinates for the instrument's current position are taken in decimal degrees and saved to a comma separated values (.csv) file for later post processing.

RTL-SDR device is set up with the following parameters: the device is tuned to the center frequency of the channel that is currently being measured, this observation frequency (Fch) is either 71MHz or 869.525MHz in this work. A sampling frequency of 2.048MHz was chosen for the RTL-SDR device because this is the highest available rate that guarantees the stability of the driver and no lost samples. The algorithm collects 5000 samples to give a RBW of 409.6Hz. A total of 5000 samples can be collected in 2.44ms at this sampling frequency. Achieving the highest speed possible is important due to the mobile nature of the instrument, readings will be taken while the instrument is in motion, so the

faster the collection is the more the measurements are localized to one position. A discussion of the chosen RTL gain will be given in Section 4.1.4.

The algorithm performs an FFT, sampling and FFT calculation is performed one hundred times, with the results averaged in order to provide a smoother and more readable spectrum with reduced noise. The resulting spectrum is represented by the solid blue line in Fig. 4.3. The time taken to collect data, produce the FFT and conduct averaging has been measured as 0.36s, 0.24s of this time can be attributed to the time it takes to record 5000 samples one hundred times. The averaged FFT is saved as a binary file for later examination, it is then passed on to the measurement part of the algorithm.

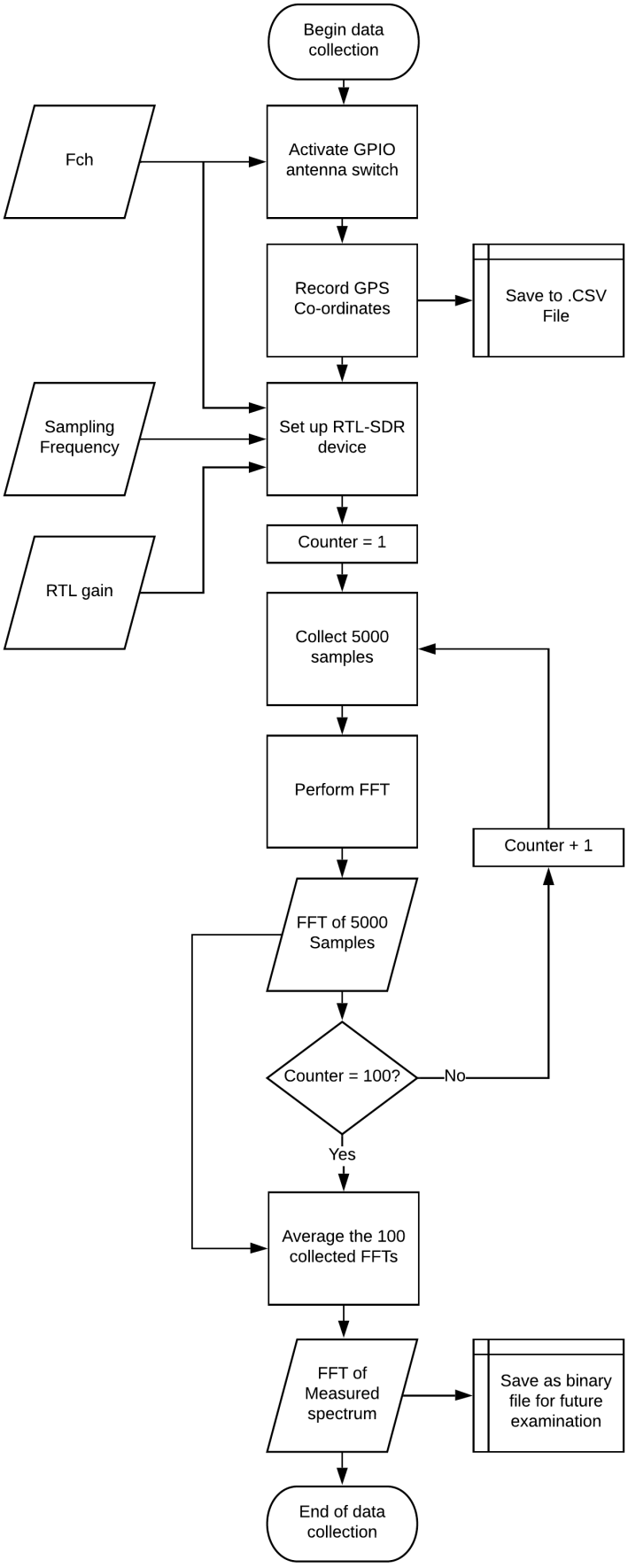

Figure 4.4: Description of method of data collection for one frequency

Fig. 4.5 shows how initial measurements are taken from the averaged FFT produced in the data collection stage.

A peak detection routine, which performs a piecewise first order differential on the FFT trace, is run on the FFT in order to identify any peaks within the collected data. The identified peaks are indicated with green dots in Fig. 4.3.

The detected peaks are searched for a peak within $\pm$50kHz of the current Fch, all peaks outside this $\pm$50kHz area of interest are ignored. These limits are shown as black dotted lines in Fig. 4.3. If a peak is detected within these boundaries it is recorded, peaks closest to the Fch are recorded first, this is the primary measurement used to determine path loss. If no peak is detected the algorithm instead records the value contained in the FFT bin closest to the current Fch, this is used as a backup primary measurement in the case of a peak detection failure.

A secondary measurement is made of the 3 highest magnitude detected peaks. This measurement is used for later debugging and if a more detailed visual inspection of the spectrum is needed.

An estimation of noise within the FFT is performed by averaging the values in every FFT bin, excluding ones where a peak has been detected. The estimated noise value is shown by the dotted red line in Fig. 4.3. This estimation will allow an estimated SNR to be calculated later. The peak detection, peak searching and noise estimation are all performed in approximately 1ms.

The information on detected peaks and estimated noise is saved to a .csv file for later post processing. This process takes approximately 16ms.

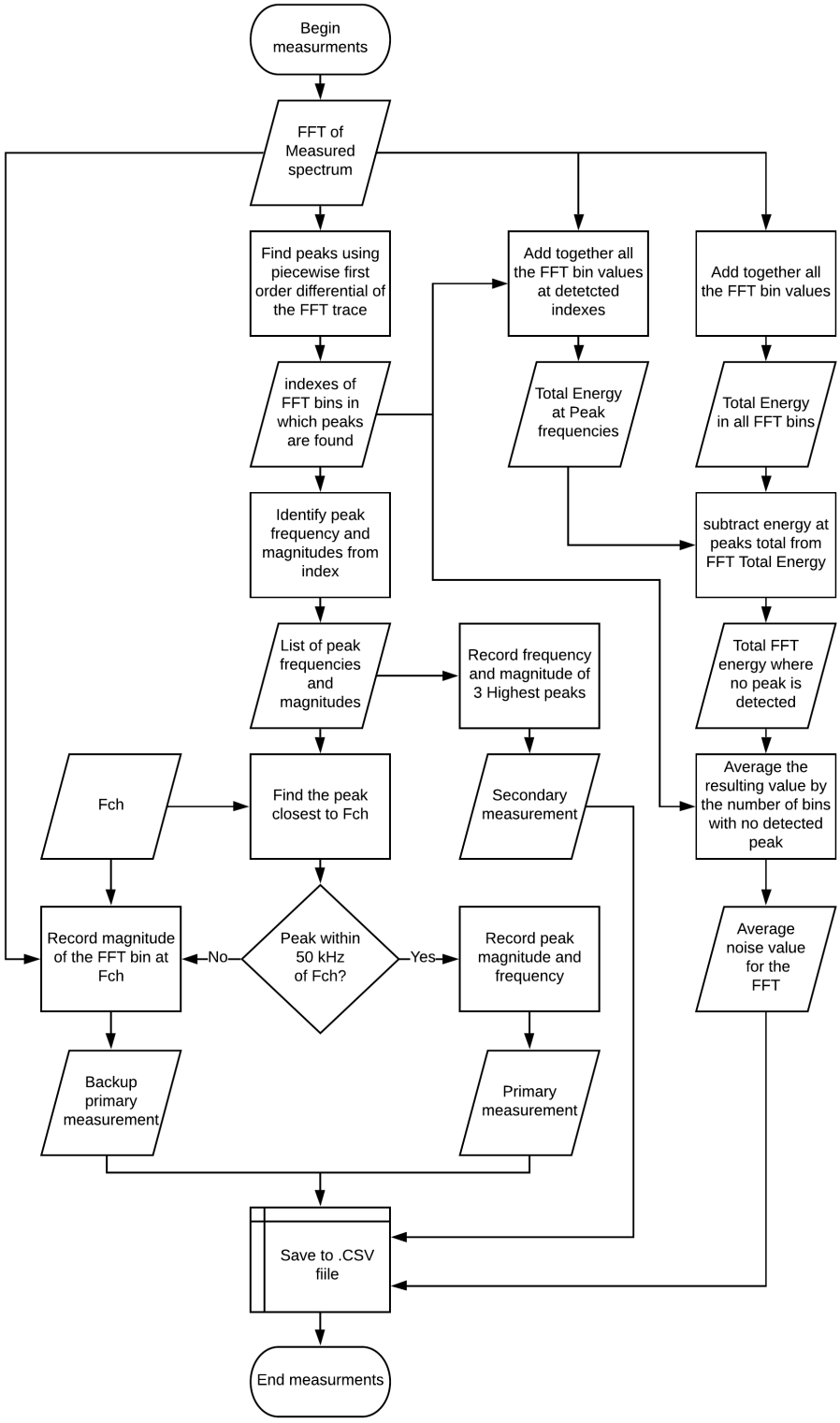

Figure 4.5: Description of the method for performing initial measurements for one frequency

The entire test involves performing data collection and then initial measurements for an Fch of 71MHz and then repeating the same process for an Fch of 869.525MHz.

The algorithm includes 0.5s pauses while the antennas are being electronically switched. Including the

pauses, the entire process is completed for both frequencies in approximately 2.25s. Within the program, measurements for each frequency are recorded within 1.6s of each other.

It is estimated that the instrument will travel at an average walking pace of 1.3m/s. At this speed the maximum Doppler shift that will be expected is 3.8Hz for the 869.525MHz signal. The resolution bandwidth used by the instrument is 409.6Hz, so such a small Doppler shift should be imperceptible [1]. Readings for each frequency are temporally separated by 1.6s, so at a pace of 1.3m/s this means the readings for 71MHz and 869.525MHz will be spatially separated by 2m.

4.1.3 Post-processing Calculation Algorithm

Once the data has been collected in the field by the SDR instrument it is then passed for post processing on a PC using MATLAB. The aim of this post processing is to calculate the path loss given by the readings and to produce a model to describe the path loss in the subject environment.

Calculating Distance From Recorded GPS Co-ordinates

A method is required to calculate the distance between the TX and each measurement location. The intention of this study is to develop a robust instrument that can operate in many different scenarios, in order to increase its usefulness. For short distances, such as the ones in the field test in this paper, a Flat Earth approximation can the used for this calculation. However, this approximation will cause a small, unnecessary, error in the results, with the error increasing as larger distances are measured. Changes in latitude of the measurements also create error. Due to the desire to allow a larger study to be completed as part of future work, the Flat Earth approximation will not be used and a more accurate method will be employed.

The Haversine formula was developed by the Royal Navy to allow sailors to calculate the distance between two points on the curved surface of the Earth [68]. In this thesis the Haversine formula, as given by (4.1), will be used to calculate the distance from the TX location to the recorded GPS location of each measurement point.

$$d = 2r \sin^{-1}\left(\sqrt{\sin^2\left(\frac{\varphi_1 - \varphi_2}{2}\right) + \cos(\varphi_1)\cos(\varphi_2)\sin^2\left(\frac{\lambda_1 - \lambda_2}{2}\right)}\right) \tag{4.1}$$

where:
d = Distance between 2 points on the surface of Earth (m)
r = Radius of the Earth (m)
φ_1, φ_2 = Latitude of point 1 and 2 (radians)
λ_1, λ_2 = Longitude of point 1 and 2 (radians)

Point 1 is defined as the TX location which is a known fixed point. Point 2 is given by the GPS co-ordinates recorded with each individual measurement.

Calculating Path Loss From Received Power

The path loss at each measurement point is calculated by considering the link budget of the system using (4.2).

$$P_L = P_{TX} + G_{TX} + G_{RX} - P_{RX} \tag{4.2}$$

where:
P_L = Path loss (dB)
P_{TX} = Transmission power measured at antenna feed (dBm)
G_{TX} = Transmission antenna gain (dBi)
G_{RX} = Receiving antenna gain (dBi)
P_{RX} = Received power at the calibrated SDR instrument (dBm)

The transmission power is a known value, measured at the antenna feed to eliminate cable losses, which is kept constant throughout the experiment. Received power is provided by the SDR instrument measurements. Gains used for the dipole antennas are 2.15dBi. The helical antenna was measured by the authors and found to have a gain of -14dBi, this is due to it being an electrically small antenna, at only 22 cm long and was considered an acceptable compromise in order to produce a portable instrument.

The path loss value given by this equation will include all losses in the environment, including shadowing.

Modifying a Log-Distance Model

The path loss of a environment can be described by the log-distance path loss model given in (4.3) [35]. Received power decays with distance in a log linear fashion, with the path loss exponent controlling the slope of the line. An extra variable can be added to the model to represent shadowing; this is a random variable with a log-normal distribution, the standard deviation of which can be calculated from recorded path loss measurements.

$$P_L(dB) = K + 10\gamma \log_{10}(d) + X_{\sigma dB} \tag{4.3}$$

where:
$P_L(dB)$ = Path Loss (dB)
K = A constant, depending on antenna characteristics and average channel attenuation [35]
γ = Path loss exponent
d = Distance between TX and RX (m)
$X_{\sigma dB}$ = log normal random variable with standard deviation of σ (dB)

Values of path loss recorded by the SDR instrument are plotted against the log of the distance between the TX source and the measurement location. Linear regression is used on this data to calculate the path loss exponent γ and constant K, to give a model of the intercept and slope.

Calculating Shadowing

Log normal shadowing is a recognised way to model the random variations in received signal strength due to shadowing within an environment [35]. The model, as calculated so far, in the above section will produce a straight line representation of path loss. This straight line is then compared back to the original measurements taken in order to find the standard deviation of these measurements from the straight line model. Equation (4.4) [35] shows how this is achieved by comparing the measurement at a specific distance with a prediction from the straight line model at that same distance. The sum of the

difference between these two values for every measurement is used to calculate the standard deviation for log normal shadowing.

$$\sigma_{dB} = \sqrt{\frac{1}{n}\sum_{i=1}^{n}[M_{measured}(d_i) - M_{model}(d_i)]^2} \tag{4.4}$$

where:

σ_{dB}	= Standard Deviation (dB)
n	= Number of measurements taken
$M_{measured}(d_i)$	= Measured path loss at distance d_i (dB)
$M_{model}(d_i)$	= Predicted path loss at distance d_i (dB)

Together these calculations produce a model which describes the slope of the TX power decay against log distance and the amount of shadowing seen in the area.

4.1.4 Measured SDR Instrument Performance

Measurements were taken with the completed SDR instrument in order to assess its performance. The input of the SDR instrument was connected to an Agilent E4437B RF vector signal generator, which was used to output a continuous wave (CW) signal, first at 70MHz and then at 869.525MHz, the power of these signals was increased from -150dBm to 0dBm in 5dBm steps. The gain of the RTL-SDR section of the SDR instrument was also adjusted to several values between the minimum and maximum available values of 0dB and 49.6dB. The output power of the signal generator was compared to the reading produced by the SDR instrument. Readings were also taken with no input provided to the SDR instrument in order to assess the noise floor.

Fig. 4.6 shows the results for SDR instrument measurements against the signal generator power at 71MHz and Fig. 4.7 shows the results for 869.525MHz. Gain settings of 0dB (minimum available), 25.4dB, 38.6dB and 49.6dB (maximum available) for the RTL-SDR were used. These figures show that across specific input powers a linear sloping relationship can be seen between the signal generator power and the SDR instrument readings. Within this linear region the instrument can be calibrated to produce accurate readings of received power.

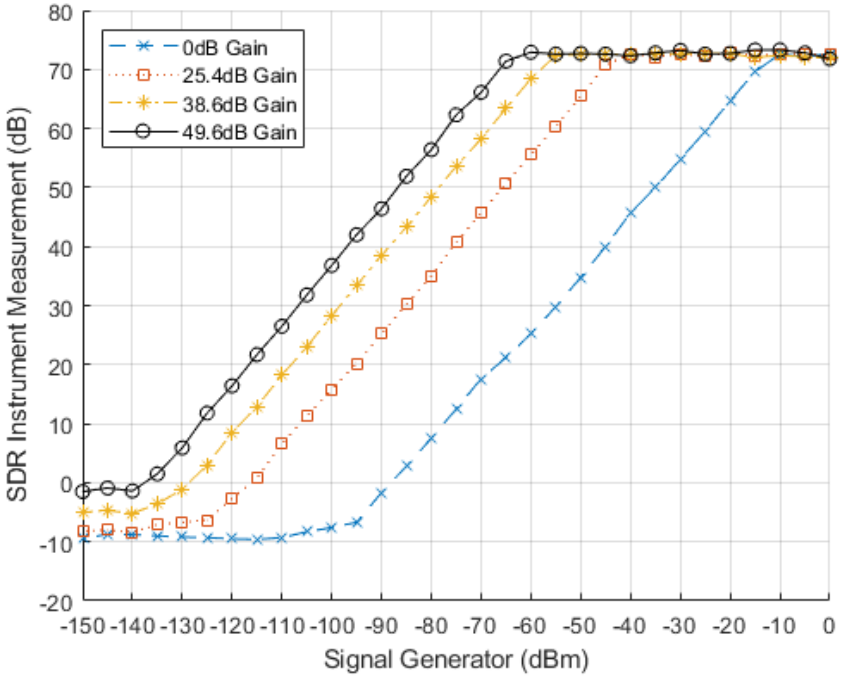

Figure 4.6: Readings taken by the SDR instrument using different gain settings at 71MHz when fed a CW signal from a signal generator

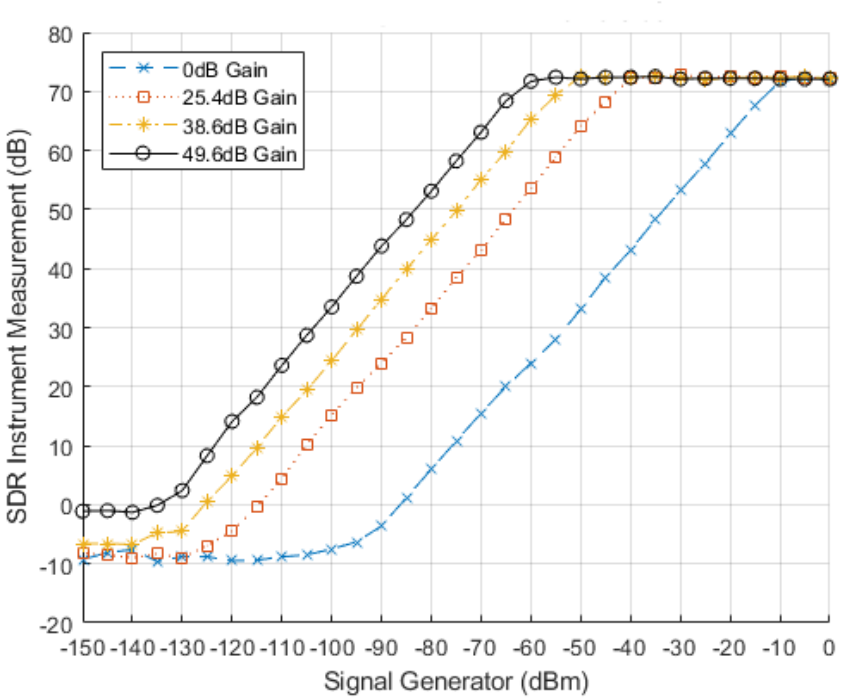

Figure 4.7: Readings taken by the SDR instrument using different gain settings at 869.525MHz when fed a CW signal from a signal generator

By examining the linear region of each graph, Table 4.1 and Table 4.2 show the dynamic range and the receive powers covered at each gain setting by the SDR instrument within this region. The displayed

average noise level (DANL) at each gain setting is also included. It can be seen that as the gain increases the dynamic range of the SDR instrument decreases, this is due to compression at the upper limit of the RTL-SDR as the noise level increases with gain. The increasing gain also allows lower signal powers to be observed, this is at the cost of being able to observe higher signal powers, due to them saturating the instrument. DANL decreases with increasing gain due to the noise level of the instrument mapping to a lower noise power as the incoming signal is amplified, the higher gain producing a corresponding improvement of the instruments noise figure.

Gain (dB)	Dynamic Range (dB)	DANL (dBm/Hz)	RX Power Coverage (dBm)
0	79	-120	-15 to -94
25.4	79	-150	-45 to -124
38.6	78	-159	-55 to -133
49.6	72	-163	-65 to -137

Table 4.1: Comparison of the performance of the SDR instrument using different gain settings at 71MHz

Gain (dB)	Dynamic Range (dB)	DANL (dBm/Hz)	RX Power Coverage (dBm)
0	83	-119	-10 to -93
25.4	83	-149	-40 to -123
38.6	80	-156	-50 to -130
49.6	73	-159	-60 to -133

Table 4.2: Comparison of the performance of the SDR instrument using different gain settings at 869.525MHz

An amplification of 49.6dB was chosen to allow the lowest signal powers to be observed thus giving the instrument higher sensitivity. It is possible to observe a constant difference between the SDR instrument readings and signal generator powers within the linear region, this difference can be used as a calibration offset factor that can be applied to the SDR instrument measurements in order to acquire a reading in dBm. The instrument produces different readings for the same input power at the two different frequencies, this difference is due to the different insertion losses of the RF switch at the different frequencies (1.2dB for 71MHz and 4.8dB for 869.525MHz). This difference necessitates that each of the frequencies be calibrated separately in order to produce an accurate result. The calibration offset factor used for 49.6dB gain is -136.5dB at 71MHz and -133dB at 869.525MHz.

In order to test the calibration of the SDR instrument, signals were again fed in to it from the Agilent E4437B signal generator, the results of this can be seen in Fig. 4.8. This shows that the SDR instrument is accurate to within $\pm$1dBm across the linear region.

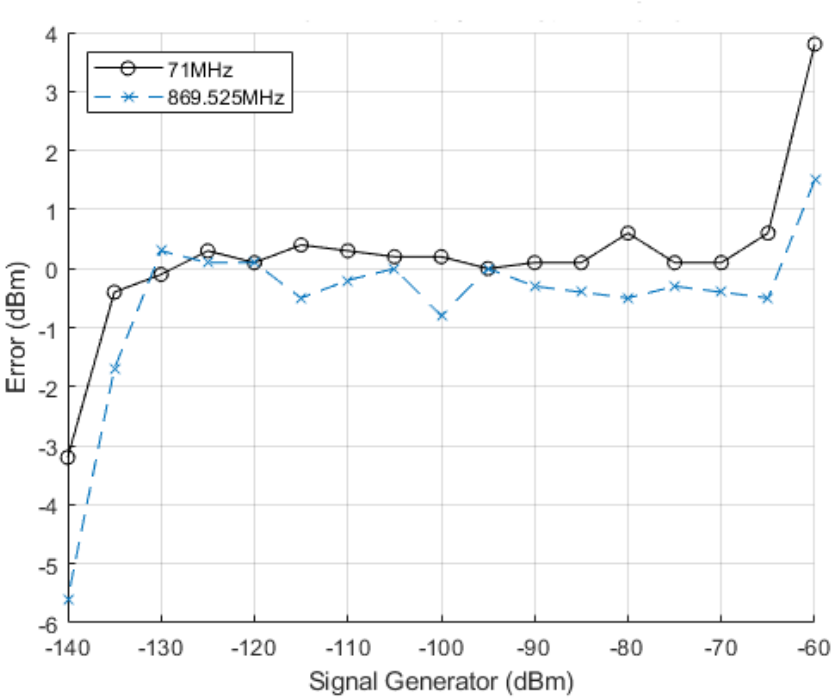

Figure 4.8: The error between the signal generator input power and the reading given by the SDR instrument using a gain of 49.6dB at 71MHz and 869.525MHz, after calibration

4.2 Proof of Concept Field Test

Results are provided for propagation measurements taken by the SDR instrument and a Spectrum Analyser, these measurements will be compared to assess the accuracy of the SDR instrument.

Fig. 4.9 shows an urban area of central Sheffield chosen for these measurements, the transmitter is located at co-ordinates 53.380834, -1.478466. Each black dot represents the location of one recorded measurement. As can be seen, multiple measurements were taken on each street to simulate a non-line-of-sight urban IoT deployment. CW signals at both 71MHz and 869.525MHz were broadcast simultaneously with a conducted power of +9.5dBm using dipole antennas.

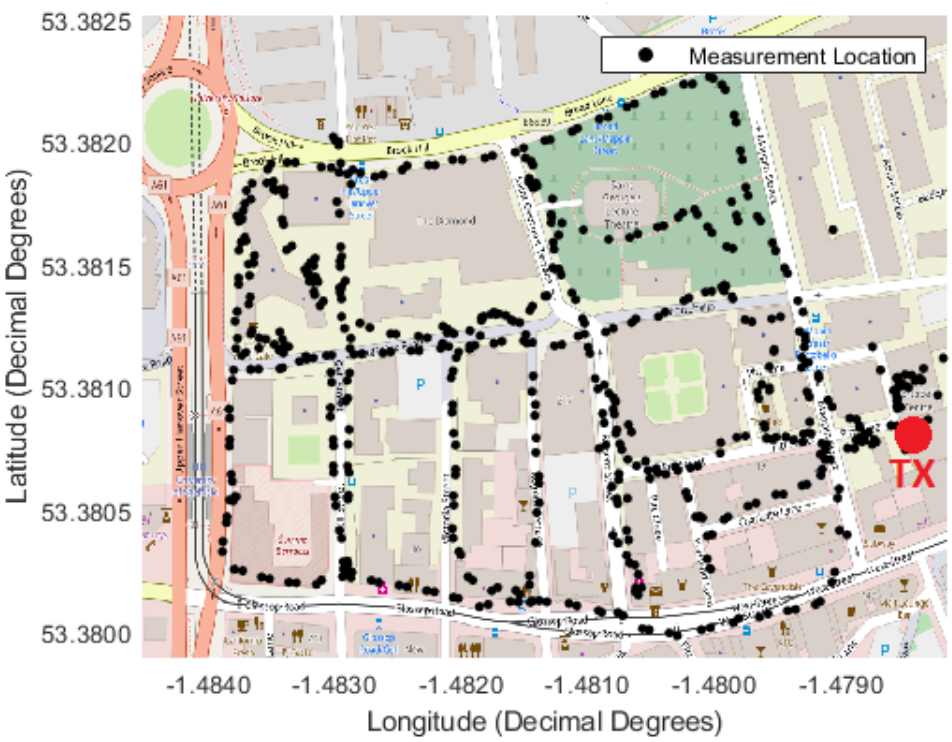

Figure 4.9: Map of the test area including GPS locations of each measurement and TX location. Underlying map ©OpenStreetMap contributors www.openstreetmap.org/copyright. [3]

Delay spread has previously been measured in the test area, at the frequencies used in this thesis, by Ball [69]. Maximum RMS delay spread was found to be less than $1\mu s$. IoT systems have a low data rate, and therefore a low symbol rate, for example LoRa ranges from 0.3kbps to 50kbps [8]. This means the symbol duration is between 3.3ms and $20\mu s$, because the symbol duration is much greater than the RMS delay spread the system will experience negligible levels of Inter-symbol Interference (ISI) [35].

The SDR instrument was carried through the test area with the on-device measurement algorithm running, the test took approximately 1 hour to perform. In total 813 readings were captured by the instrument. Within these readings the 71MHz CW signal was detected 71 times and the 869.525MHz signal was detected 296 times. This gives 71 path loss measurements to calculate the VHF path loss model and 296 measurements to calculate the UHF path loss model. These readings are shown in Fig. 4.11 and Fig. 4.12 as cross markers.

Measurements have also been taken with an Anritsu MS2712E portable spectrum analyser, at a number of locations throughout the test area. Each of these measurements can then be compared to a measurement taken by the SDR instrument at the same location, thus validating the SDR instruments measurements. The spectrum analyser was set to a RBW of 300Hz, an input attenuation of 0dB and a frequency span of 2MHz in order to match the operation of the SDR instrument as closely as possible. One Antenna at a time (dipole, then helical) was connected to the SDR instrument and the spectrum analyser at the same time via a splitter to provide both instruments with the same RF signal.

A comparison of one set of measurements taken at the same location by the SDR instrument and the spectrum analyser is shown in Fig. 4.10. It can be seen that the readings for both instruments at both frequencies agree to within 0.9dBm.

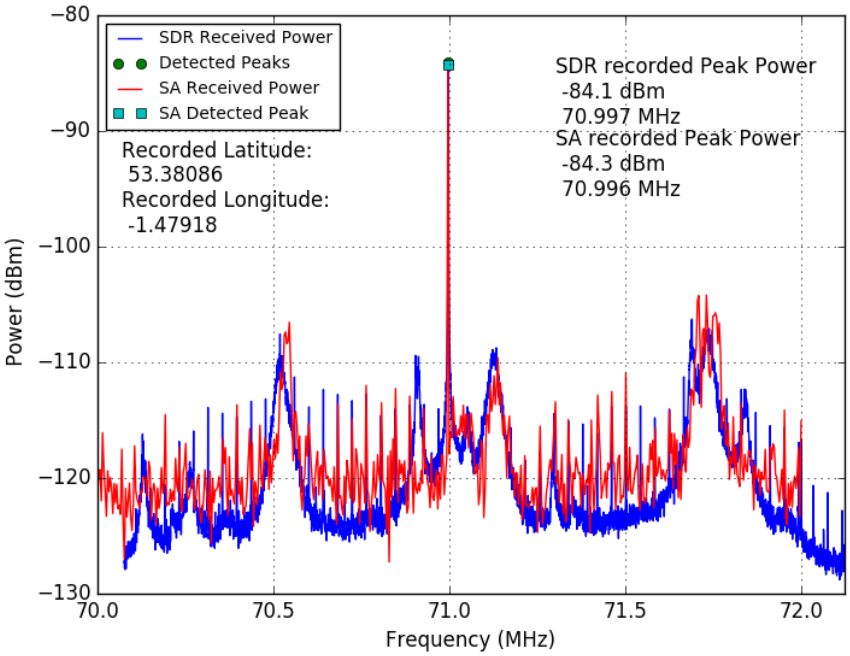

(a) 71MHz signal measurements

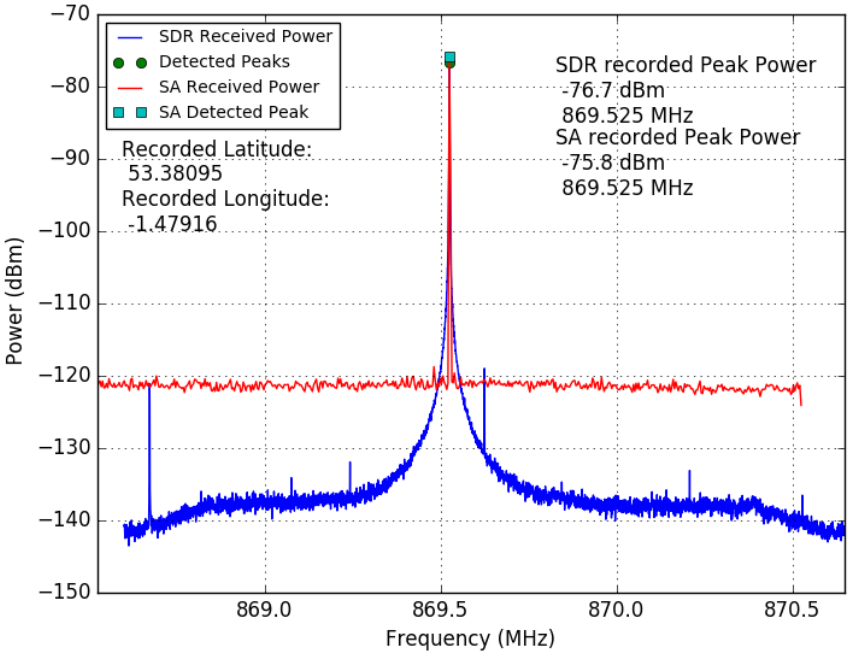

(b) 869.525MHz signal measurements

Figure 4.10: A comparison of readings taken by the SDR instrument and the spectrum analyser at the same location for the same signals

Table 4.3 shows the absolute differences between SDR instrument and spectrum analyser readings for all the measurements taken at the same locations. It can be seen that overall the measurements from each device agreed to a high degree of certainty.

Table 4.3: Comparison of differences between readings from the SDR instrument and spectrum analyser at all matching locations

Frequency (MHz)	Maximum difference (dB)	Average difference (dB)	Standard deviation of average difference (dB)	RMS Difference (dB)
71	4.0	1.3	1.4	1.9
869.525	3.6	1.2	1.1	1.6

The readings taken be the spectrum analyser were converted to path loss information, which is shown in Fig. 4.11 and 4.12 by the circle markers.

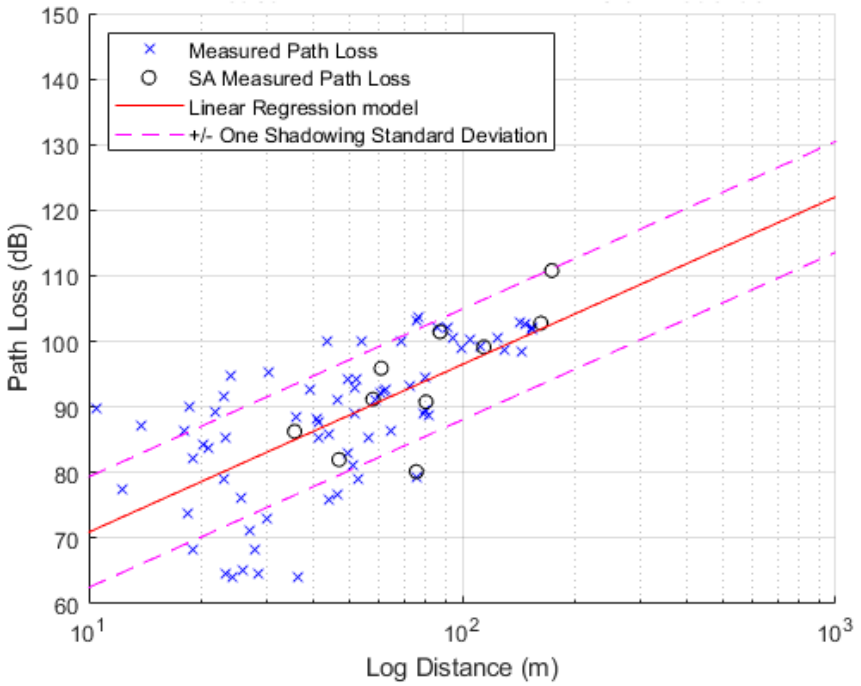

Figure 4.11: Measured path loss and the Log Distance Model calculated from the measurements at 71MHz using the SDR instrument, with spectrum analyser measurements shown for comparison

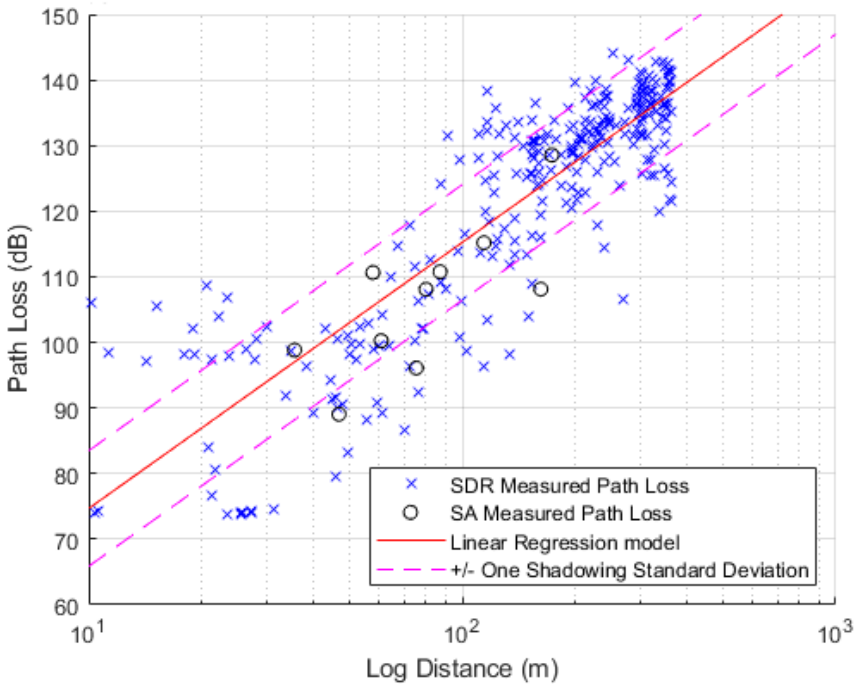

Figure 4.12: Measured path loss and the Log Distance Model calculated from the measurements at 869.525MHz using the SDR instrument, with spectrum analyser measurements shown for comparison

The path loss models created from the SDR instrument readings in Fig. 4.11 and Fig. 4.12 are shown in (4.5) for 71MHz and (4.6) for 869.525MHz. For 71MHz a path loss exponent (γ) of 2.44 and a shadowing standard deviation (σ) of 8.5dB were calculated. For 869.525MHz a path loss exponent (γ) of 4.06 and a shadowing standard deviation (σ) of 8.8dB were calculated.

$$P_{L71}(dB) = 45.3 + 25.6\log_{10}(d) + X_{8.4dB} \tag{4.5}$$

$$P_{L869}(dB) = 34.1 + 40.6\log_{10}(d) + X_{8.8dB} \tag{4.6}$$

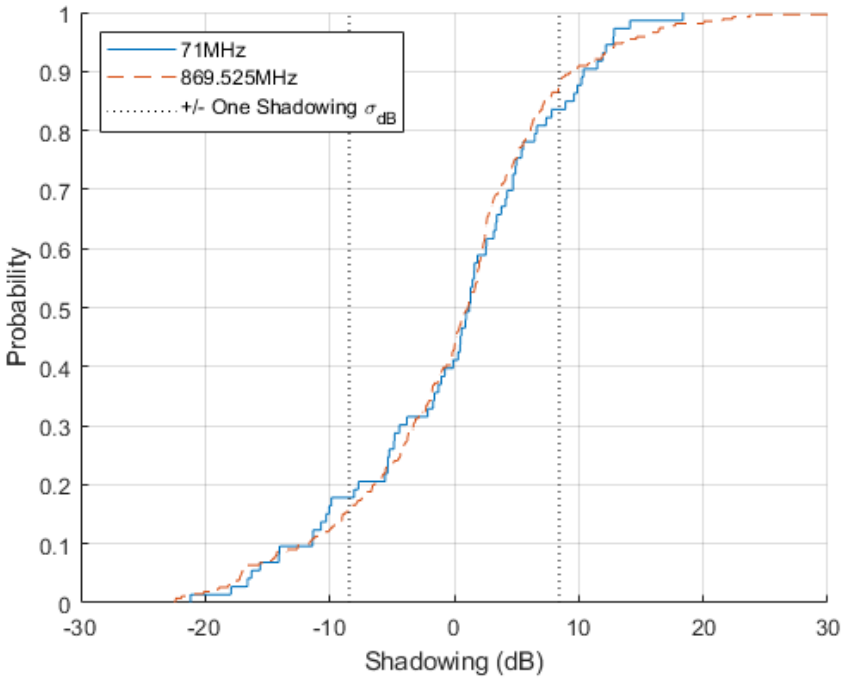

Figure 4.13: A cumulative distribution function plot showing the distribution of shadowing measured by the instrument

For the calculation of the shadowing standard deviation part of the Log Distance Model it is assumed that the shadowing follows a log-normal distribution. During the calculation the shadowing present in each measurement is recorded, Fig. 4.13 shows the cumulative probability distribution of the recorded shadowing, confirming that its distribution is indeed log-normal and validating this assumption.

The readings and models developed were compared to the established Hata urban and suburban models given in (3.6), (3.7) and (3.8). These models are commonly used for mobile communication deployments in cluttered environments, however they are only valid for distances over 1km, frequencies of 150MHz to 1500MHz and TX heights above 30m. This means the model is not valid for the use case considered in this chapter, but it is included as the closest available widely accepted model found.

The measurements taken and model calculated in this chapter compared to Hata predictions at 71MHz are shown in Fig. 4.14. It can be seen that the loss measured varies between 40dB and 20dB more than predicted, with slope of the calculated model being less than predicted.

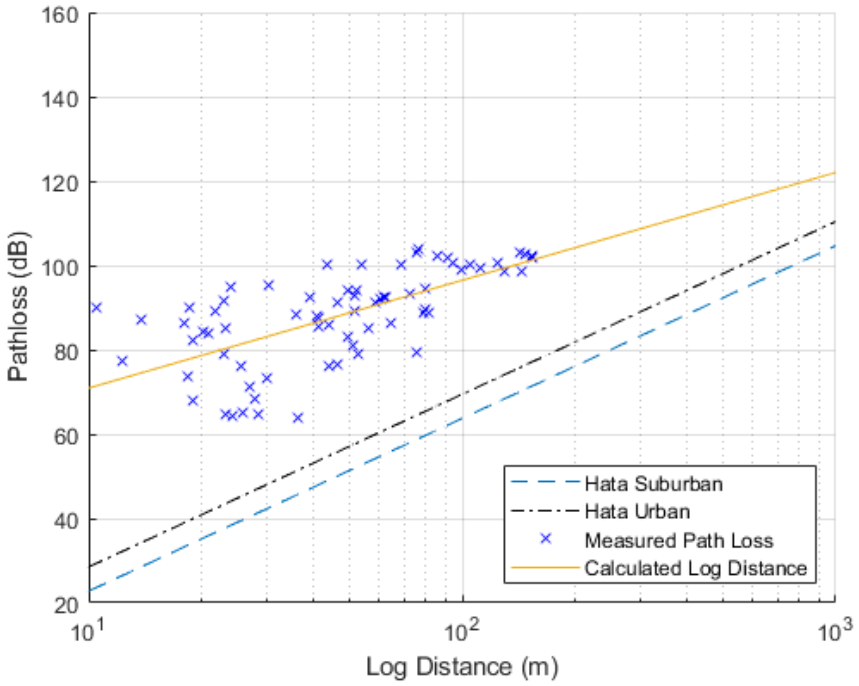

Figure 4.14: Measured path loss and the Log Distance Model calculated from the measurements at 71MHz, with Hata Urban and Suburban Predictions

The measurements taken and model calculated in this chapter compared to Hata predictions at 869.525MHz are shown in Fig. 4.15. It can be seen that the loss measured is on average 20dB more than predicted, with slope of the calculated model matching the prediction well. It was expected that the Hata models would disagree with the actual measurements due to the models being used outside their specifications. However, it appears that the Hata models are closer to being valid at 896.525MHz than 71MHz.

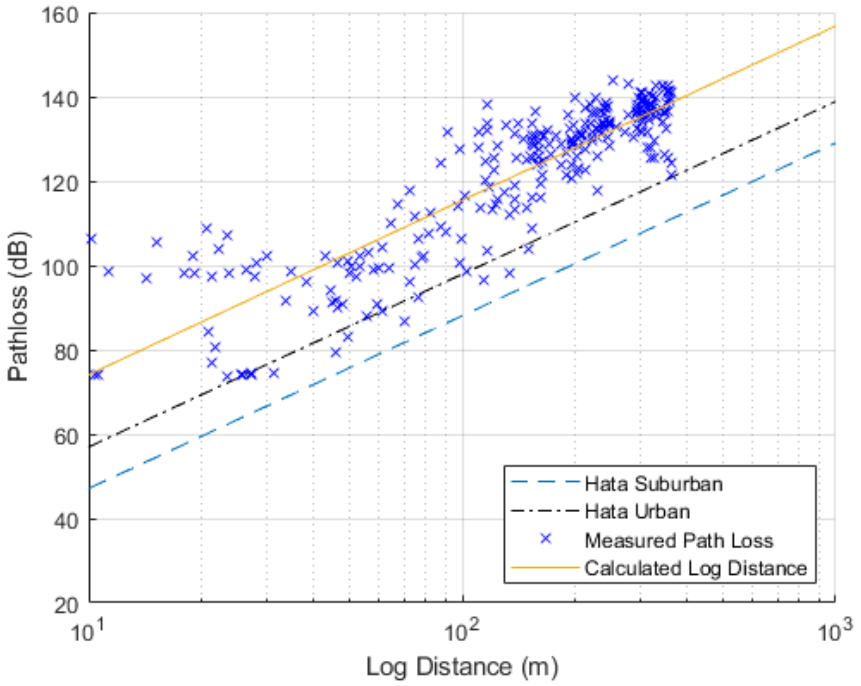

Figure 4.15: Measured path loss and the Log Distance Model calculated from the measurements at 869.525MHz,with Hata Urban and Suburban Predictions

The cumulative probability function (CDF) of the path loss readings within the test area are shown in Fig. 4.16. By considering this information and the link budget of a system it is possible to infer the outage probability of a system within the test area. In order to have a maximum outage probability of 10% at 71MHz a link budget of at least 102dB is required. At 869.525MHz a link budget of at least 138dB is required.

This shows that signals at 869.525MHz require a much higher link budget than at 71MHz, meaning propagation is more favourable at VHF. This is expected due to VHF usually having more favourable propagation characteristics than UHF.

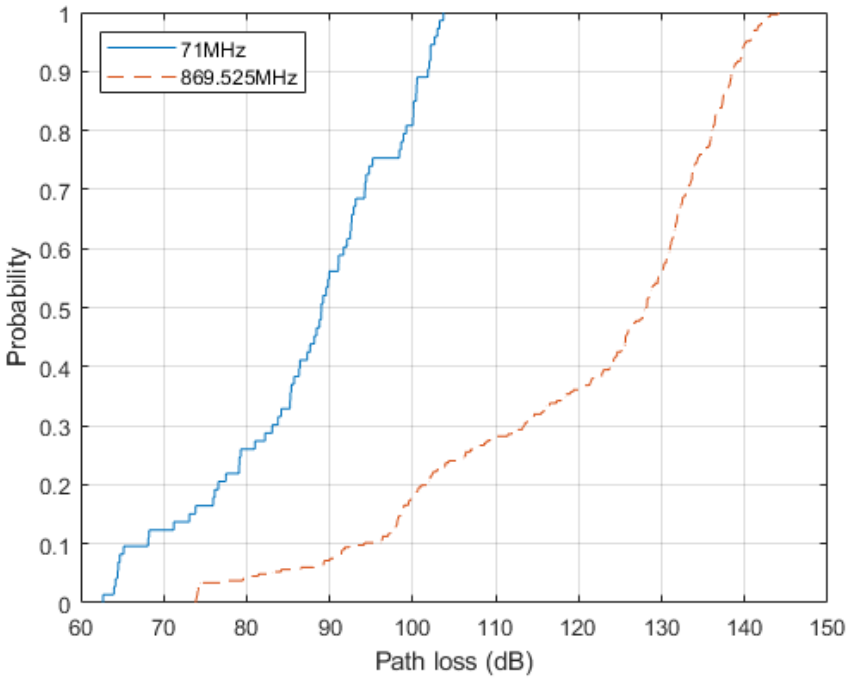

Figure 4.16: CDF of measured path loss readings

Measurements of detected signal strength, in the order they were taken, as the instrument was carried through the test area are shown for 71MHz in Fig. 4.17 and for 869.525MHz in Fig. 4.18. Because the instrument was carried at 1.3m/s this means that, with the exception of sampling periods where no signal was detected, each measurement for the same frequency is taken 5 seconds apart and is separated by 6.5m. The figures also show the difference between each adjacent measurement.

The average and standard deviation of the adjacent difference are shown in the figures, 71MHz has an average of 0.1dB and a standard deviation of 8.1dB, 869.525MHz has an average of 0.0dB and a standard deviation of 7.6dB. Averages were also taken using the absolute results for adjacent difference so as no to have the negative differences skew the results, it is seen that 6.2dB is the average at 71MHz and 5.3dB is the average at 869.525MHz. These figure include the effect of movement relative to the TX as well as shadowing and multipath effects. Even though no measurement of delay spread was undertaken, the variations shown between the adjacent measurements imply that the readings were taken within a rich channel.

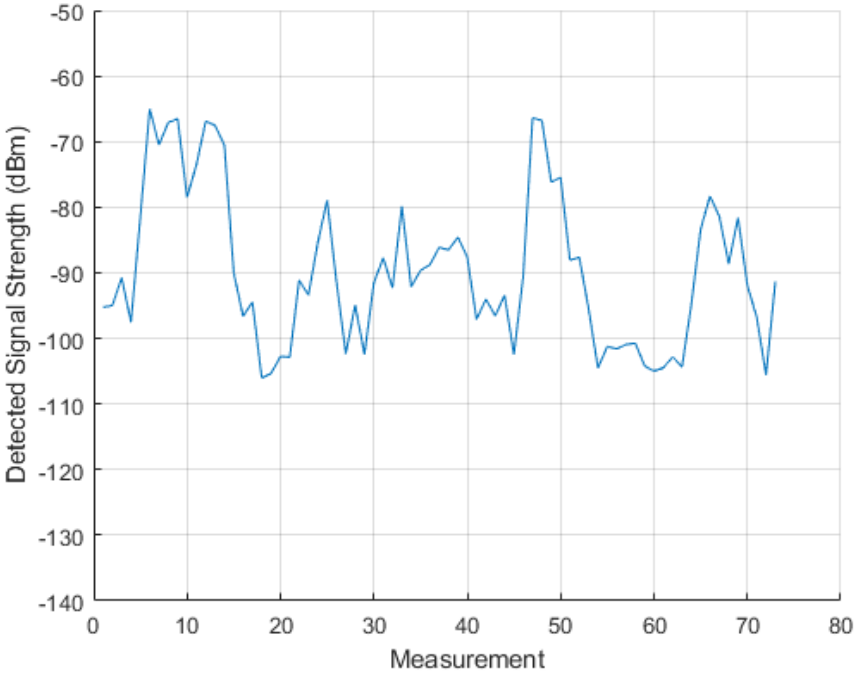

(a) 71MHz Signal Strength for each Measurement

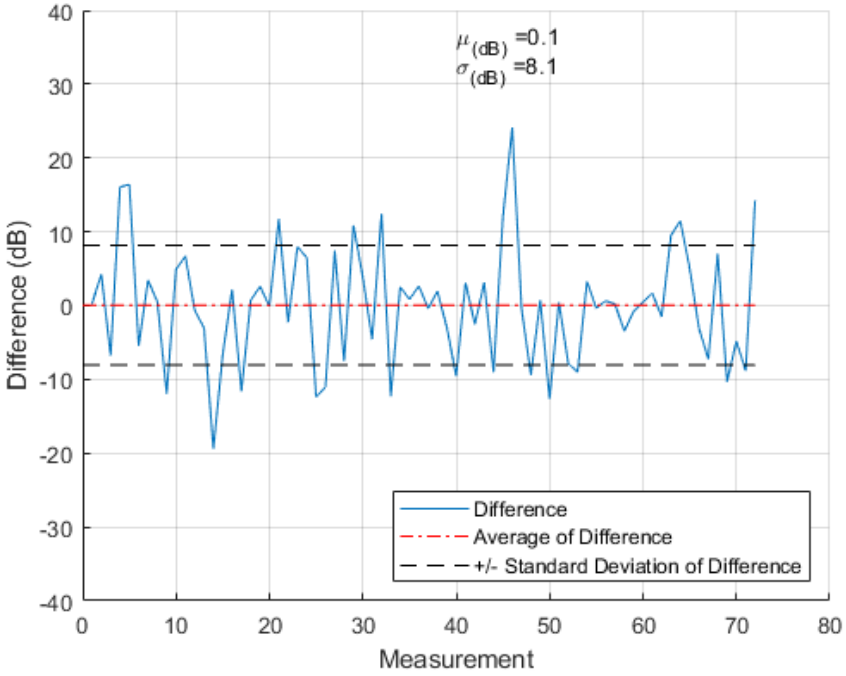

(b) 71MHz Difference Between each Adjacent Signal Strength Measurement

Figure 4.17: Readings taken by the SDR instrument in the order they were taken with the difference between each adjacent reading at 71MHz

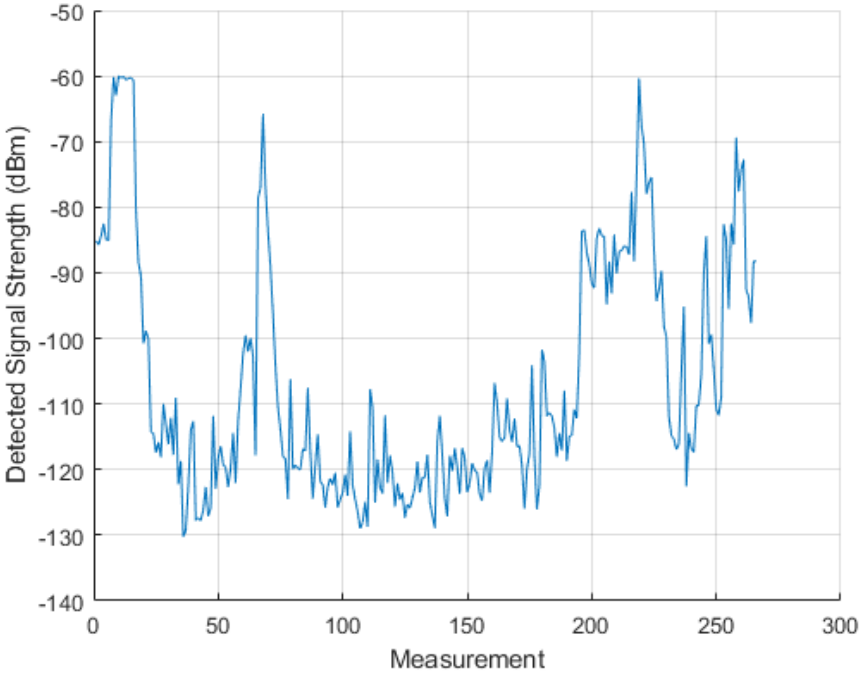

(a) 869.525MHz Signal Strength for each Measurement

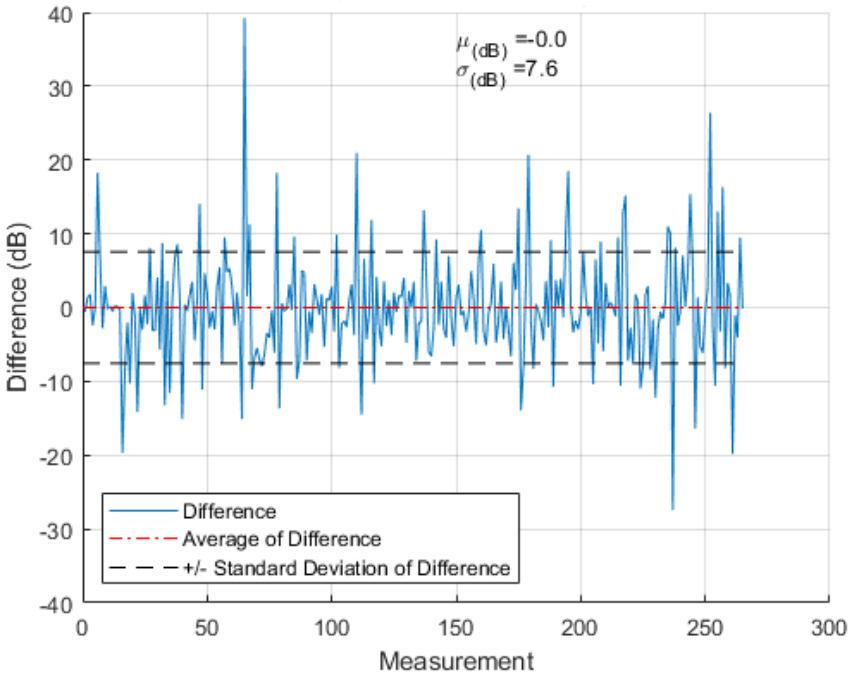

(b) 869.525MHz Difference Between each Adjacent Signal Strength Measurement

Figure 4.18: Readings taken by the SDR instrument in the order they were taken with the difference between each adjacent reading at 869.525MHz

4.3 Conclusion

It has been shown that it is possible to perform measurements of the RF spectrum using low cost COTS SDR equipment, to a similar standard as an expensive spectrum analyser. It has also been shown that hundreds of localized measurements are able to be collected by this instrument in a short space of time, providing extensive data for propagation studies. Due to the inherent ease of re-programming of all SDRs it was possible to develop and deploy new measurement and post-processing algorithms quickly.

The results obtained provide validation of the approach in this thesis, showing that the results agree with results taken by a commercial spectrum analyser. It also proves that current models such as Hata do not accurately model propagation within this use case, showing the value of conducting a propagation study with this instrument.

Further work in this thesis will describe the use of the developed SDR instrument to perform urban, suburban and rural IoT based propagation studies in a number of different cities and locations, in order to investigate the possible use of the new VHF spectrum in these environments. The instrument will be deployed for measurements using a car, allowing much larger areas to be covered quickly. Until now the device has been carried at 1.3m/s and takes 0.24s to collect 5000 samples 100 times, this means that the measurement for an individual frequency is taken over a 0.32m distance, for driving deployments this distance will be longer due to higher speeds. Initial tests on congested city streets at speeds of up to 30km/h (8.3m/s), giving a distance of 1.9m for the measurement, have shown no negative effects on the accuracy of the instrument.

Chapter 5

Location Based Measurement Campaign

This chapter will proceed to use the COTS SDR based instrument previously developed and described in chapter 4 of this thesis to perform propagation studies at 71MHz and 869.525MHz for comparison between the frequencies. The studies are conducted in a number of different environments (rural, suburban, urban and dense urban), with measurement equipment deployed in a manner suitable for a portable IoT use case. Results are presented in comparison to other propagation studies available in the literature and widely used propagation models such as the Hata model. Shadowing and noise are also measured and examined.

The work described in this chapter has been published in a journal paper by the author [5].

Established Propagation Models

The propagation measurements taken in this chapter will be compared with predictions taken from currently available propagation models. This will enable these models to be validated for the frequencies and environments studied here, or to establish the requirement for a new model to be developed. The models used are listed as follows:

- **Free Space Pathloss** [70]. Included to provide a baseline comparison with the simplest way to predict propagation.
- **Two Ray Model** [35]. Included to provide a slightly more complicated comparison and investigate the accuracy of modelling propagation in an urban or suburban environment with only two propagated rays (one Line of Sight, one reflected). Can an urban canyon be accurately modelled using only two dominant rays?
- **Hata Urban** [35]. A widely used empirical model for urban mobile communications, valid for frequencies of 150MHz to 1500 MHz, distances over 1km and TX antenna heights over 30m. This model is not valid for the use case in this chapter (distances and antenna heights are much shorter), but it is included to assess the use case against established, currently utilized models for urban deployments.
- **Hata Suburban** [35]. Is an extension of the Hata model for suburban deployments.
- **Models identified in the literature review** developed by Andrusenko *et al.* [40] (GUPL) and El Chall *et al.*[44] identified in Section 3.2

5.1 Field Measurements

In this chapter the same antennas from chapter 4 are again used here, A sleeved dipole (2.15 dBi gain) is used for UHF reception and a Helical antenna (-14 dBi gain) is used for VHF reception, in order to represent the small, low efficiency antennas common in IoT applications. TX is provided by a custom designed VHF transmitter and a Silicon Labs Si106x wireless MCU development kit [71] for UHF, both transmitters are connected to dipole antennas (2.15 dBi gain) and transmit a CW signal with a conducted power to the antennas of +9.5 dBm, giving an EIRP of +11.65 dBm. The instrument is carried in a car around a predetermined area of interest, measurements of RX power and GPS location are recorded in order to be processed in to pathloss information. It is likely that the measurements will be a rich mixture of LoS and Non-Line-of-sight (NLoS), due to the nature of the trials. It is not practical to try and split the measured data on a point-by-point basis to ascribe it to LOS or NLOS. Due to licences obtained from Ofcom the instrument operates at 71MHz and 869.525MHz.

The following subsections provide details of the areas where measurements are taken, including location co-ordinates for the transmitters, antenna heights and a map of the areas with individual measurement locations indicated. Multiple diverse locations were chosen for measurements in order to provide information across dense urban, urban, suburban and rural environments. The heights and locations of the TX antennas were determined by the availability of access to secure sites for the equipment within the desired environment, for example university building rooftops and residential balconies were the only secure sites available with cities.

5.1.1 Rural (Burniston)

Measurements were taken in and around the rural village of Burniston, near Scarborough, UK. The area consists of farm land, woods and small residential settlements. A map of the area with measurement and TX locations can be seen in Fig. 5.1. The TX is located at the approximate co-ordinates -0.449, 54.323 with an antenna height of 2m. The instrument conducted 725 measurements from which 89 detections of the 71MHz signal and 134 detections of the 869.525MHz signal were registered.

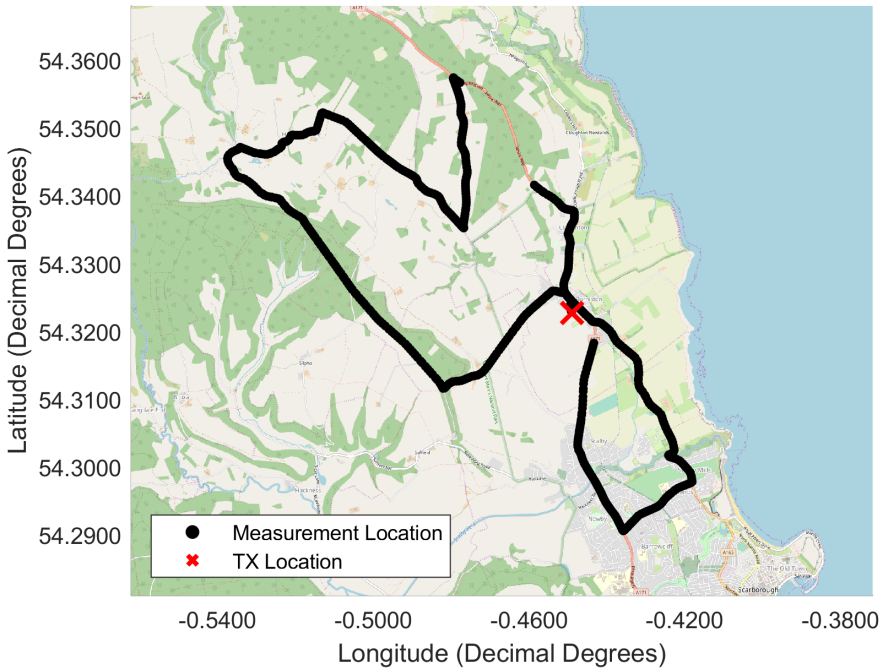

Figure 5.1: Locations of TX and Measurements in the Buriston Area. Underlying map ©OpenStreetMap contributors www.openstreetmap.org/copyright.

Calculated pathloss measurements for VHF and UHF are shown in Fig. 5.2 along with the calculated Log Distance Model and shadowing standard deviation given in (5.1) and (5.2).

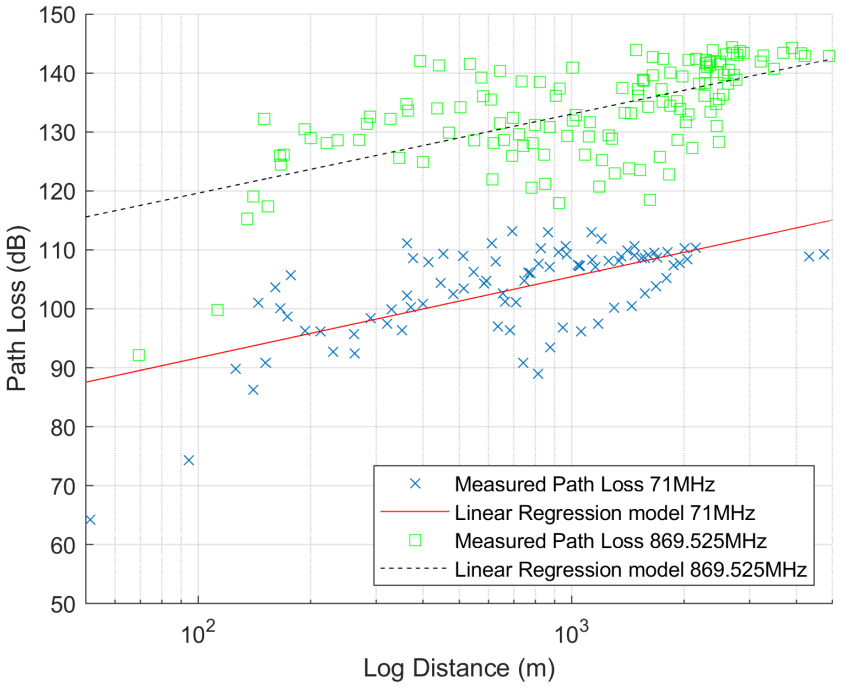

Figure 5.2: Burniston Propagation Results for VHF and UHF

The RF noise measured in the area during the test is shown in Fig. 5.3

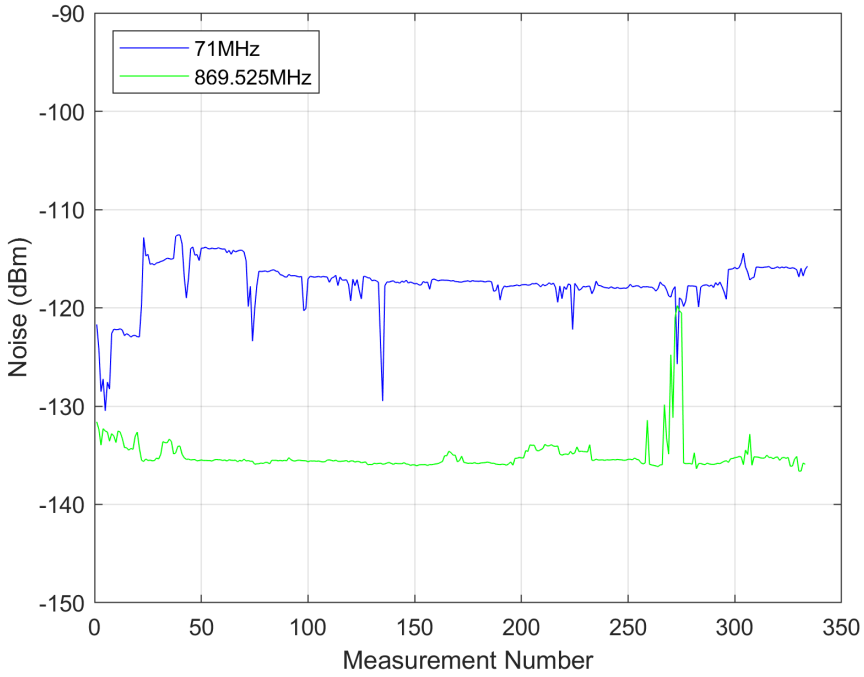

Figure 5.3: Burniston Noise Measurements for VHF and UHF

$$P_{L71}(dB) = 64.2 + 13.8\log_{10}(d) + X_{6.1dB} \tag{5.1}$$

$$P_{L869}(dB) = 92.8 + 13.4\log_{10}(d) + X_{6.5dB} \tag{5.2}$$

The calculated path-loss exponent for the fitted rural models in (5.1) & (5.2) show a result lower than 2. This is very unusual, but can occur with constructive ray interference and has been seen elsewhere within buildings [1] and in vehicle to vehicle propagation studies [72]. It is also note that the fixed loss parameter K for the rural models is very high, suggesting the propagation was subject to very significant fixed loss, possibly skewing the model and resulting in the lower slope parameter. However, the model does have a good overall fit to the measured data, as seen by the R^2 values in Table 5.1 & Table 5.2. Care should be taken in field tests to try and minimise any initial deployment fixed losses, to reduce this skewing of the fitted models. The high fixed loss also led to less signal detection's being registered for both frequencies in this environment, when compared to the other environments in this section.

5.1.2 Suburban (Wakefield)

Measurements were taken around a suburban area of Wakefield, UK. The area consists of residential, parkland and low rise warehouses. A map of the area with measurement and TX locations can be seen in Fig. 5.4. The TX is located at the approximate co-ordinates -1.505, 53.715 with an antenna height of 4m. The instrument conducted 2101 measurements from which 826 detections of the 71MHz signal and 901 detections of the 869.525MHz signal were registered.

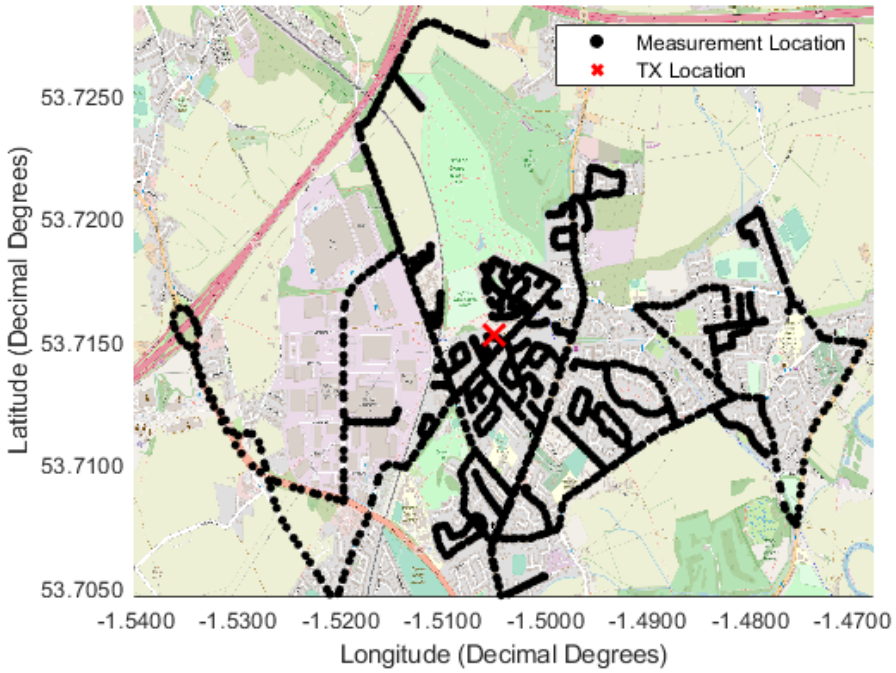

Figure 5.4: Locations of TX and Measurements in Wakefield. Underlying map ©OpenStreetMap contributors www.openstreetmap.org/copyright.

Calculated pathloss measurements for VHF and UHF are shown in Fig. 5.5 along with the calculated Log Distance Model and shadowing standard deviation given in (5.3) and (5.4).

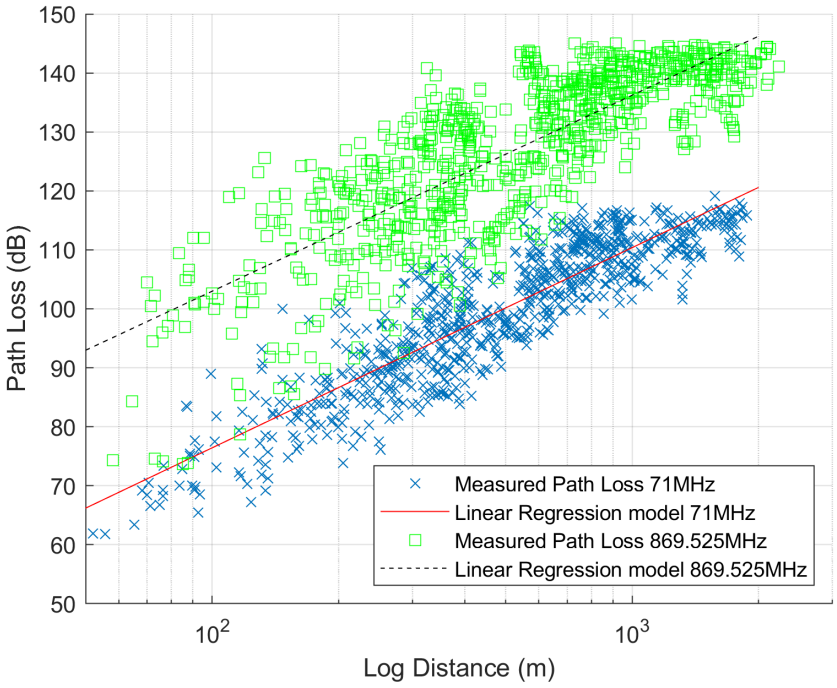

Figure 5.5: Wakefield Propagation Results for VHF and UHF

The RF noise measured in the area during the test is shown in Fig. 5.6

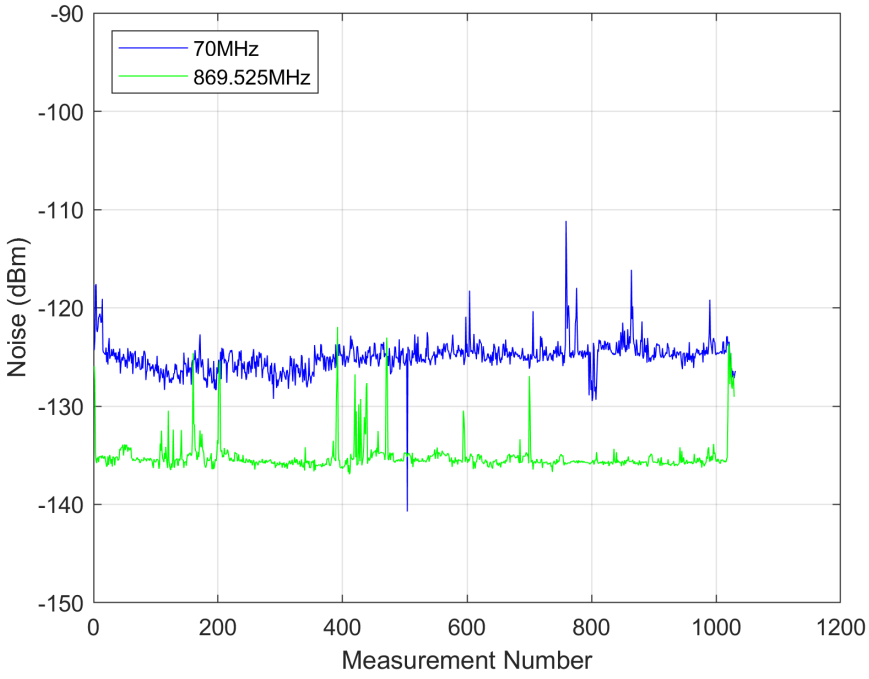

Figure 5.6: Wakefield Noise Measurements for VHF and UHF

$$P_{L71}(dB) = 8.5 + 34.0\log_{10}(d) + X_{5.5dB} \tag{5.3}$$

$$P_{L869}(dB) = 36.5 + 33.2\log_{10}(d) + X_{8.0dB} \tag{5.4}$$

5.1.3 Urban (Sheffield)

Measurements were taken in and around the city center of Sheffield, UK. The area consists of retail, high rise residential and low rise industrial. A map of the area with measurement and TX locations can be seen in Fig. 5.7. The TX is located at the approximate co-ordinates -1.477, 53.382 with an antenna height of 10m. The instrument conducted 999 measurements from which 280 detections of the 71MHz signal and 418 detections of the 869.525MHz signal were registered.

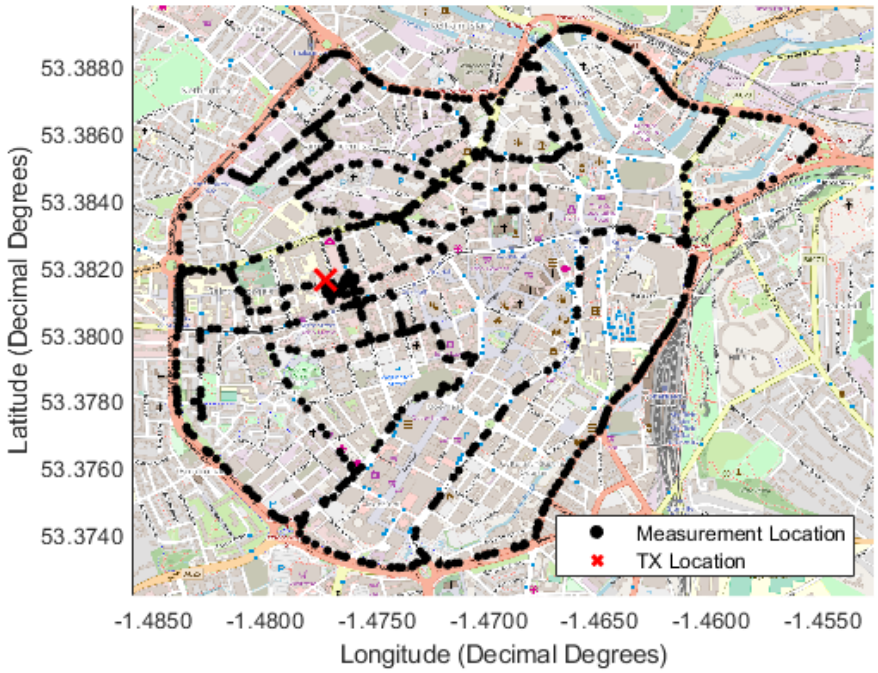

Figure 5.7: Locations of TX and Measurements in Sheffield. Underlying map ©OpenStreetMap contributors www.openstreetmap.org/copyright.

Calculated pathloss measurements for VHF and UHF are shown in Fig. 5.8 along with the calculated Log Distance Model and shadowing standard deviation given in (5.5) and (5.6).

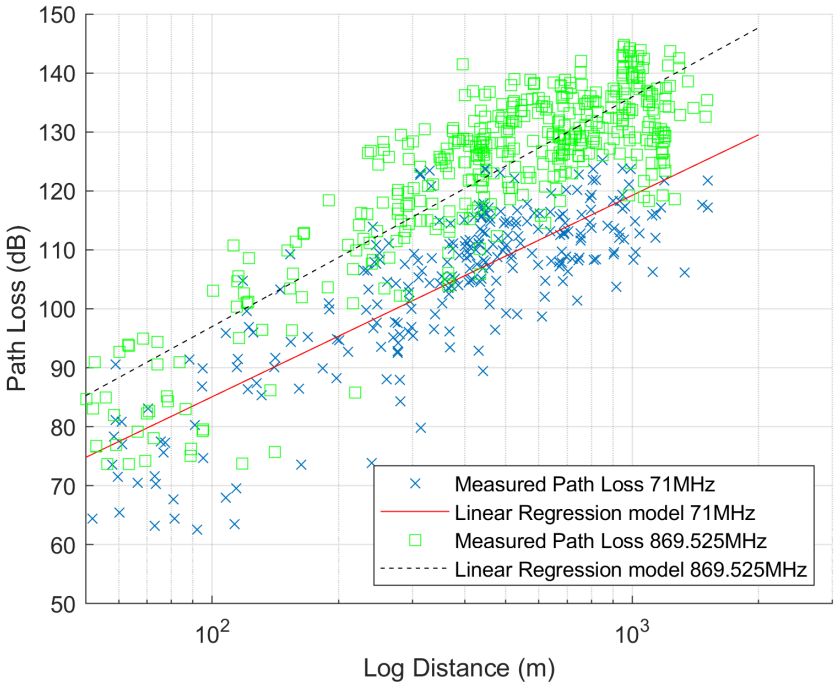

Figure 5.8: Sheffield Propagation Results for VHF and UHF

The RF noise measured in the area during the test is shown in Fig. 5.9

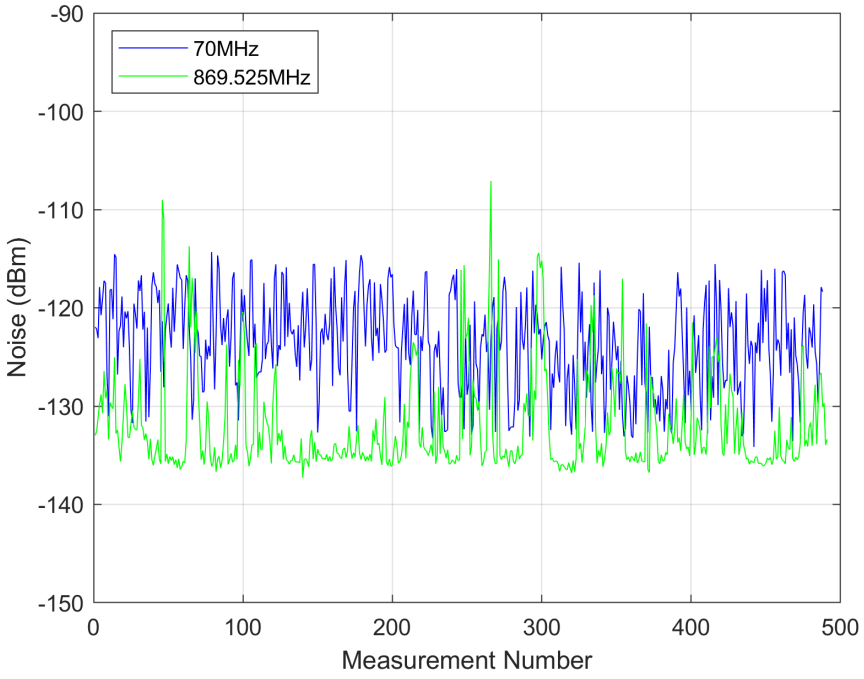

Figure 5.9: Sheffield Noise Measurements for VHF and UHF

$$P_{L71}(dB) = 16.8 + 34.2\log_{10}(d) + X_{8.1dB} \tag{5.5}$$

$$P_{L869}(dB) = 19.1 + 38.9\log_{10}(d) + X_{7.9dB} \tag{5.6}$$

5.1.4 Dense Urban (Leeds)

Measurements were taken in and around the city center of Leeds, UK. The area consists of retail, commercial and high rise residential. The area was chosen as dense urban over the Sheffield area due to the presence of many more tall buildings and the city's higher population. A map of the area with measurement and TX locations can be seen in Fig. 5.10. The TX is located at the approximate coordinates -1.536, 53.794 with an antenna height of 20m. The instrument conducted 1248 measurements from which 503 detections of the 71MHz signal and 517 detections of the 869.525MHz signal were registered.

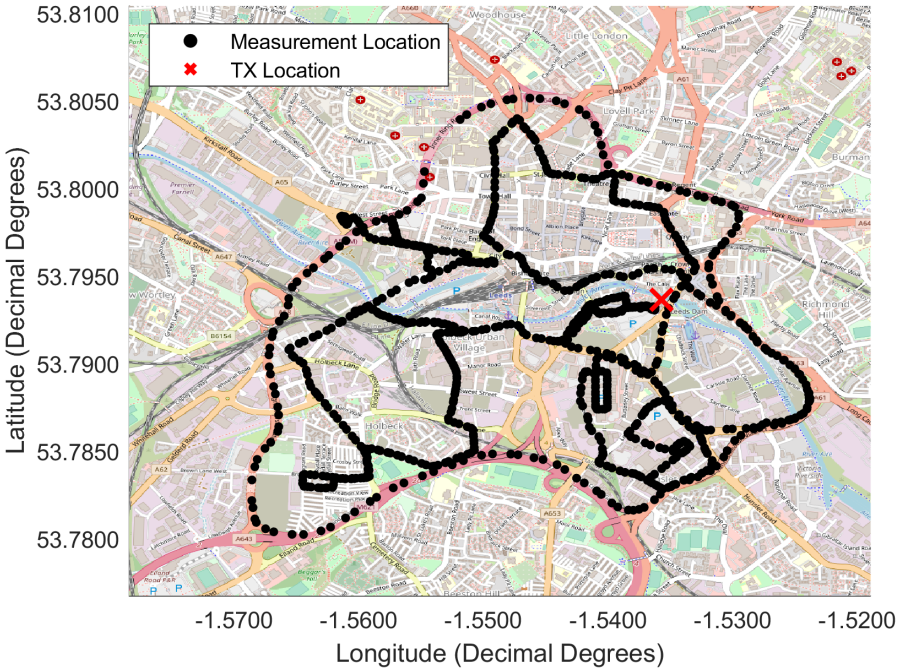

Figure 5.10: Locations of TX and Measurements in Leeds. Underlying map ©OpenStreetMap contributors www.openstreetmap.org/copyright.

Calculated pathloss measurements for VHF and UHF are shown in Fig. 5.11 along with the calculated Log Distance Model and shadowing standard deviation given in (5.7) and (5.8).

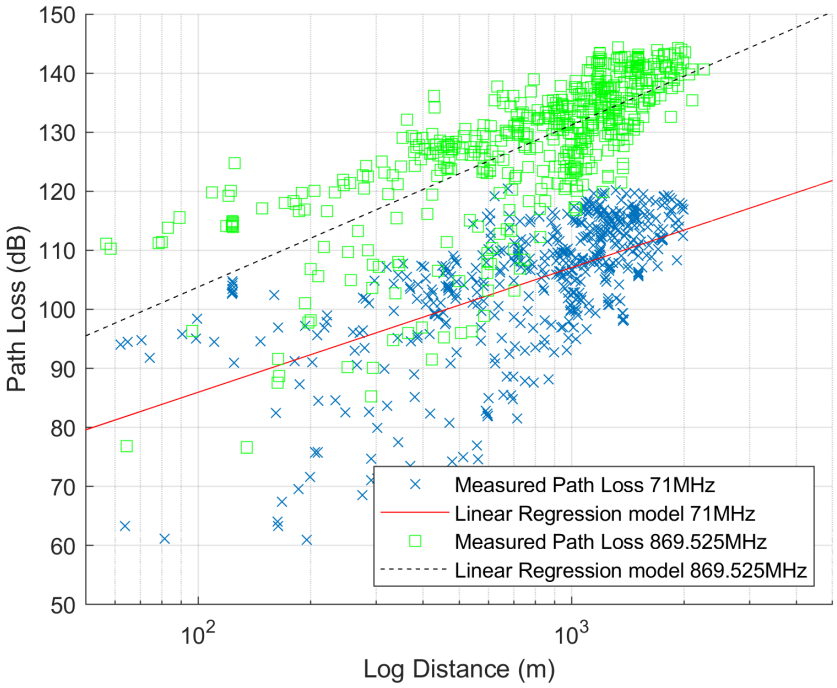

Figure 5.11: Leeds Propagation Results for VHF and UHF

The RF noise measured in the area during the test is shown in Fig. 5.12

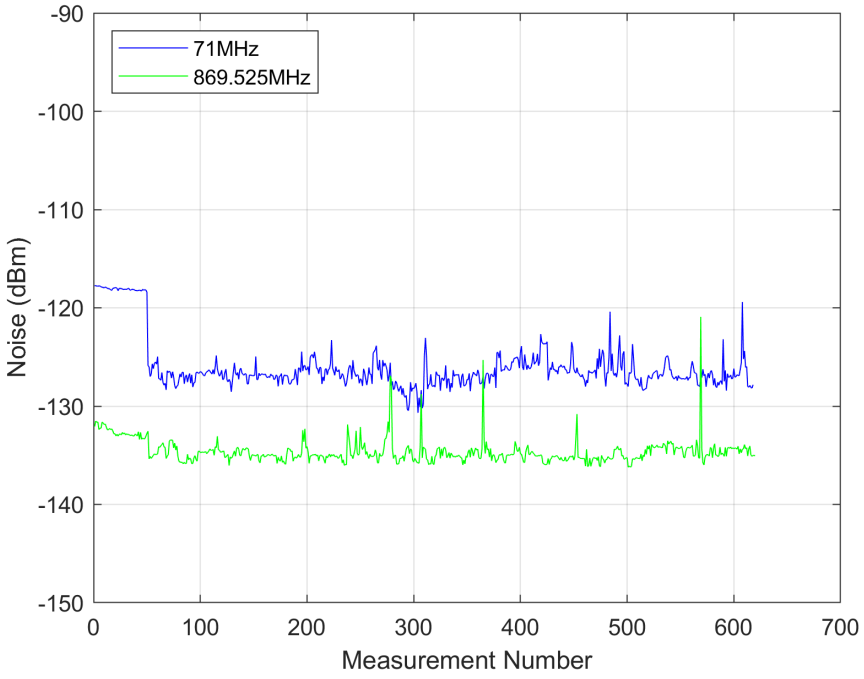

Figure 5.12: Leeds noise Measurements for VHF and UHF

$$P_{L71}(dB) = 43.7 + 21.1\log_{10}(d) + X_{8.9dB} \tag{5.7}$$

$$P_{L869}(dB) = 48.9 + 27.4\log_{10}(d) + X_{7.9dB} \tag{5.8}$$

Tables 5.1 and 5.2 show a summary of the path-loss exponent (γ), channel constant (K), shadowing (σ) and the R^2 fit for the straight line component of each model in the different environments.

Environment	γ	K	σ (dB)	R^2
Rural	1.38	64.2	6.1	0.43
Sub-urban	3.40	8.5	5.5	0.80
Urban	3.42	16.8	8.1	0.66
Dense Urban	2.11	43.7	8.9	0.38

Table 5.1: Summary of The Calculated Log-distance parameters at VHF

Environment	γ	K	σ (dB)	R^2
Rural	1.34	92.8	6.5	0.41
Sub-urban	3.32	36.5	8.0	0.66
Urban	3.89	19.1	7.9	0.64
Dense Urban	2.74	48.9	7.9	0.53

Table 5.2: Summary of The Calculated Log-distance parameters at UHF

5.2 Results

The measurements taken, which are described in Section 5.1 are now analysed in this section. Attention will be directed to path loss measurements and their comparisons with model predictions in Section 5.2.1, the measured shadowing and predictions in Section 5.2.2, the measured noise in Section 5.2.3 and the effects of correcting free space and two ray models for extra clutter loss (including knife-edge diffraction) on the prediction accuracy of these models in Section 5.2.4.

5.2.1 Path Loss

The measurements and calculated models from Section 5.1 are compared to the established propagation models discussed in Section 5. The Root Mean Squared Error (RMSE) between the predictions and the measurements (E_{RMS}) are given in Table 5.3 for Rural Burniston, Table 5.4 for Suburban Wakefield, Table 5.5 for Urban Sheffield and Table 5.6 for Dense Urban Leeds.

Model	E_{RMS} (dB)	
	VHF	UHF
Free Space	37.6	63.7
Two-Ray	11.9	24.9
Hata Urban	13.4	22.5
Hata Suburban	13.0	27.3
GUPL	59.8	72.4
El Chall	-	24.5
Calculated Model	6.1	6.5

Table 5.3: RMSE Between Measurements and Established Models Predictions in the Rural Environment

Table 5.3 shows the Calculated Model produced in this chapter best matches the rural measurements. No standard models produce good predictions at VHF or UHF, though the predictions are significantly better at VHF.

Model	E_{RMS} (dB)	
	VHF	UHF
Free Space	37.2	63.8
Two-Ray	9.8	34.6
Hata Urban	6.6	29.8
Hata Suburban	10.4	35.3
GUPL	21.8	37.0
El Chall	-	40.4
Calculated Model	5.5	8.0

Table 5.4: RMSE Between Measurements and Established Models Predictions in the Suburban Environment

Table 5.4 again shows that the Calculated Model best fits the suburban measured data at VHF and UHF.

Two-Ray, Hata Urban and Hata Suburban produce comparable results to the Calculated Model at VHF. This is surprising because the Hata models are not recommended for use in the VHF frequency examined here. Hata models are recommended for use in the UHF frequency, so a better performance would be expected from the models at UHF than VHF. No other standard model produces good results at either frequency, though again the predictions are better at VHF.

Model	E_{RMS} (dB)	
	VHF	UHF
Free Space	44.6	60.8
Two-Ray	26.6	39.9
Hata Urban	18.7	31.9
Hata Suburban	24.0	37.4
GUPL	25.9	33.0
El Chall	-	40.4
Calculated Model	8.1	9.0

Table 5.5: RMSE Between Measurements and Established Models Predictions in the Urban Environment

Table 5.5 shows that the Calculated Model gives the best fit to the urban measurement data at VHF and UHF. No standard model produces good results at either frequency, though again the predictions are better at VHF.

Model	E_{RMS} (dB)	
	VHF	UHF
Free Space	38.6	61.5
Two-Ray	21.4	43.0
Hata Urban	13.3	33.2
Hata Suburban	17.5	38.7
GUPL	67.2	28.3
El Chall	-	39.1
Calculated Model	8.9	7.9

Table 5.6: RMSE Between Measurements and Established Models Predictions in the Dense Urban Environment

Table 5.6 once again shows that the Calculated Model produces predictions that best fit the dense urban measured data. No standard model produces good results at either frequency, though again the predictions are better at VHF.

It is perhaps unsurprising that the Calculated Log-Distance Model performed best in all environments at both VHF and UHF, this model was directly based on the measured results for each environment. It is however surprising that the Hata Urban and Suburban models consistently performed better outside their stated frequency range (VHF) than within (UHF). The GUPL and El Chall models both failed to produce accurate results even though they are based on measurements from similar environments, this suggests that a model that is very tailored to a particular place may not transfer very well to other places,

even when the environment is similar.

The calculated Log distance path loss models for both frequencies in all locations are compared in Fig. 5.13. This shows that path-loss is consistently lower at VHF than at UHF. This is expected behaviour and shows that VHF retains an advantage for long distance communications even in urban areas when using the use case set out in this thesis. At both VHF and UHF the loss for the urban environment is very high, this is due to a very high fixed loss (K) present in the data, with then only a slight fitting slope needed. This can possibly be attributed to the deployment of the TX very close to a building, in an area surrounded by trees.

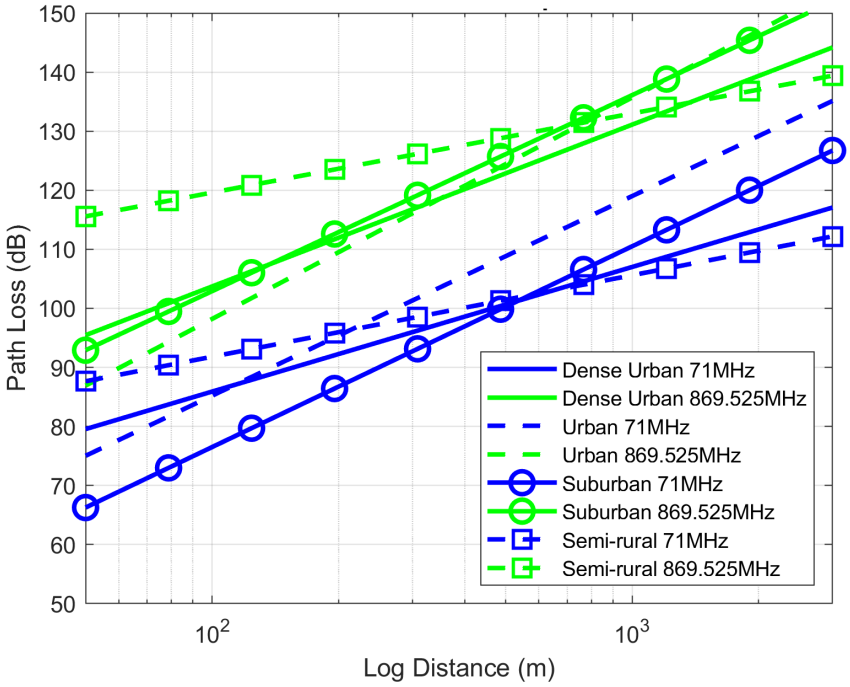

Figure 5.13: Comparison of the Calculated Models for all the Considered Environments

Table 5.7 shows the measured pathloss exponents of the calculated Log Distance models that were produced for both frequencies in all environments. Expected behaviour would be to see higher pathloss exponents for UHF over VHF within each environment and also for pathloss exponents to increase when moving to a more cluttered environment. However, the actual behaviour seen with the measurements show that in both rural and suburban environments the pathloss exponents are roughly similar at VHF and UHF. Thus suggesting that clutter in these environments reduces the advantage of VHF while having less effect on UHF, at the studied use case. For environments with more clutter the pathloss exponent does tend to increase as predicted, with the exception of dense urban. This can be attributed to the high antenna height use in the Leeds test, which is twice as high as the urban test antenna, placing it above much of the surrounding clutter and producing a scenario with much better propagation characteristics than the tests with antennas much closer to ground or located amongst much taller clutter.

Environment	VHF (γ)	UHF (γ)
Rural	1.38	1.34
Suburban	3.40	3.32
Urban	3.42	3.89
Dense Urban	2.11	2.74

Table 5.7: Comparison of Pathloss Exponents from our Calculated Model for VHF and UHF in all Environments

5.2.2 Shadowing

The ITU-R provide a method for prediction of shadowing in large flat urban areas in their recommendation ITU-R P.1406-2 [73] which is stated to be valid from 100MHz to 3GHz, this method is given in (5.9).

$$\sigma_L = 5.25 + 0.42 \log_{10}\left(\frac{f}{100}\right) + 1.01 \log_{10}^2\left(\frac{f}{100}\right) \tag{5.9}$$

where:
σ_L = Standard deviation for a given length (dB)
f = Frequency (MHz)

This method is used to provide predictions which can be compared to the measurements taken in order to verify the validity of the method's possible use for the re-purposed VHF bands examined here. Using the model the following shadowing standard deviation predictions were made: σ_L = 5.2dB at 71MHz and σ_L = 6.5dB at 869.525MHz

The measured shadowing is compared to the prediction given by the ITU recommendation ITU-R P.1406-2 [73]. The Log Normal shadowing standard deviation values for 71MHz and 869.525MHz within each test area are given in Table 5.8. El Chall *et al.*[44] also provides predictions for shadowing in LoRa deployments as part of their model, campus = 9.7dB, Urban = 7.2dB and rural = 6.4dB.

Frequency	ITU Prediction (dB)	Rural (dB)	Suburban (dB)	Urban (dB)	Dense Urban (dB)
VHF	5.2	6.1	5.5	8.1	8.9
UHF	6.5	6.5	8.0	7.9	7.9

Table 5.8: Observed and Predicted Shadowing Standard Deviation

The predictions given by the ITU are a little lower than the measurements, at VHF the measurements differ by the following; rural = 0.9dB, suburban = 0.3dB, urban = 2.9dB and dense urban = 3.7dB, at UHF the measurements differ by the following; rural = 0.0dB, suburban = 1.5dB, urban = 1.4dB and dense urban = 1.4dB. Considering the ITU prediction is for flat urban areas and not all areas measured were flat or urban some deviation from the predictions were expected. Table 5.9 shows the variation of the height above sea-level for the measurements locations.

Environment	Mean (m)		Standard Deviation (m)		Maximum (m)		Minimum (m)	
	VHF	UHF	VHF	UHF	VHF	UHF	VHF	UHF
Rural	66.0	79.0	27.2	36.9	197.3	186.4	42.4	36.9
Suburban	76.4	73.7	10.2	14.6	99.7	106.4	26.5	23.1
Urban	84.5	77.1	21.1	20.4	154.7	158.3	47.9	47.2
Dense Urban	37.9	37.4	10.8	9.7	82.7	71.5	11.3	4.9

Table 5.9: Height of the Recorded Measurements Above Sea-Level in Each Environment

For VHF, measurements show greater shadowing in rural areas than Suburban, but shadowing is shown to increase as the urban environment increases in density, as would be expected. UHF measurements show lower shadowing for rural areas, but consistent shadowing as the urban density increases, meaning the increase in urban density has no further effect on shadowing. UHF measurements match well with the measurements made by El Chall *et al.* for LoRa deployments. Shadowing values are very similar at both VHF and UHF, with the exception of the suburban environment, no frequency shows a clear advantage over the other.

5.2.3 Noise

The average noise level and the standard deviation of this average for each environment and frequency are compared in this section, this is shown in Table 5.10. All noise measurements are made within a 409.6Hz bandwidth.

Environment	Mean (dBm)		Standard Deviation (dB)	
	VHF	UHF	VHF	UHF
Rural	-117	-135	2.5	1.9
Suburban	-125	-135	1.6	1.6
Urban	-124	-132	4.9	4.9
Dense Urban	-126	-135	1.2	2.6

Table 5.10: Analysis of the Noise Measured in Each Environment

At VHF the average noise level roughly increases as the density of human activity increases from rural to dense urban, suggesting that presence of more electronic device and human activity increases the noise in the environment. At UHF the average noise level does not increase in the same way and is constant across the environments, suggesting the noise may not be as dependent on human activity. By inspecting the standard deviation results in Table 5.10 and figures 5.3, 5.6, 5.9 and 5.12 it is possible to see there is a greater variation in the noise measurements at both frequencies within the urban environment than within any other in environment. The measurements for the urban environment were performed during the normal working day, whereas the other environments were measured outside this time at weekends and evenings. This suggests that the heavier human activity during the work day may create a more diverse RF environment and add a time-dependant factor to the levels of noise present in these environments.

5.2.4 Extra Clutter Loss

The ITU provides a model for the prediction of extra loss due to clutter, including knife-edge diffraction, in ITU-R P.2108-0 [74] this is shown in (5.10) and (5.11). The model is valid for terminals deployed below the level of the representative clutter height at frequencies between 30MHz and 3GHz.

By changing the value for representative clutter height between the values recommended by the ITU, 10m for rural and suburban, 15m for urban and 20m for dense urban [74] it is possible to calculate the extra loss predicted in each environment. This extra loss can be added to the Free Space Pathloss and Two Ray Model to act as a form of correction factor to make these models more accurate to the measured data. Table 5.11 shows the extra clutter loss results predicted by the ITU model.

$$A_h = \begin{cases} J(\nu) - 6.03 & \text{for all Urban} \\ -K_{h2} \log_{10}(h/R) & \text{for Rural} \end{cases} \tag{5.10}$$

where:
A_h = Additional loss due to clutter (dB)
$J(\nu)$ = Single knife-edge diffraction loss estimate, given by (5.11)
K_{h2} = $21.8 + 6.2 \log_{10}(f)$

$$J(\nu) = 6.9 + 20 \log_{10} \left(\sqrt{(\nu - 0.1)^2 + 1} + \nu - 0.1 \right) \tag{5.11}$$

where:
$J(\nu)$ = Single knife-edge diffraction loss estimate
ν = $K_{nu} \sqrt{h_{diff} \theta_{clut}}$
h_{diff} = $R - h$ (m)
θ_{clut} = $\tan^{-1} \left(\frac{h_{diff}}{w_s} \right)$ (degrees)
K_{nu} = $0.342\sqrt{f}$
f = Frequency (GHz)
w_s = Relates to width of street (m) default = 27
R = Representative clutter height (m)
h = Antenna height (m)

Environment	VHF (dB)	UHF (dB)
Rural	12.1	17.7
Suburban	8.6	18.6
Urban	11.8	22.4
Dense Urban	14.2	24.9

Table 5.11: ITU Predicted Extra Clutter Loss from Equation (5.10) for all Considered Environments and Frequencies

Table 5.12 shows the RMSE (E_{RMS}) of both the free space path loss model and the two ray model when additional clutter losses from Table 5.11 are incorporated in to each model, considered against the measurements taken in each environment at VHF and UHF. Using previous results shown in Tables 5.3,

5.4, 5.5 and 5.6, the cluttered and uncluttered Free space RMSEs are compared to see if the RMSE to the measurements has been decreased by the addition of clutter to the model, the same process is performed with the cluttered and uncluttered two ray models. The difference between cluttered and uncluttered for each model is noted in the table by E_{dif}, a negative difference suggests the RMSE has decreased and the model has therefore become more accurate, a positive difference suggests the RMSE has increased and therefore the model has become less accurate.

Environment	Free Space with Clutter				Two Ray with Clutter			
	E_{RMS} (dB)		E_{dif} (dB)		E_{RMS} (dB)		E_{dif} (dB)	
	VHF	UHF	VHF	UHF	VHF	UHF	VHF	UHF
Rural	25.8	46.2	-11.8	-17.5	17.6	13.2	5.7	-11.7
Suburban	28.8	45.5	-8.4	-18.3	5.9	17.2	-3.9	-17.4
Urban	33.1	38.9	-11.5	-21.9	15.8	18.8	-10.8	-21.1
Dense Urban	25.0	37.0	-13.6	-24.5	11.7	19.3	-9.7	-23.7

Table 5.12: RMSE Between Extra Clutter Loss Inclusive Models and the Measured Path-loss. Including the Change in RMSE Between Corrected and Uncorrected Models

In almost all the scenarios considered, the addition of clutter loss increased the accuracy of the models predictions by a significant amount, shown by E_{dif} in Table 5.12, with the best case improving by 24.9dB. This is to be expected because clutter loss is a very important mechanism affecting propagation, so adding a consideration of its effects will produce a more complete model. However, none of the corrected free space models predictions came close to the accuracy of the Hata or calculated models. The corrected two ray model performed better, especially at UHF, where the accuracy was much better than the Hata models, but not as good as the calculated models.

5.3 Conclusion

It has been shown that the current mainstream propagation models do not accurately predict the propagation loss of an IoT deployment at the frequencies of 71MHz and 869.525MHz within rural, suburban, urban or dense urban environments with RX antennas deployed close to ground. It has also been shown that the propagation at these frequencies and within these environments can be accurately modelled using a conventional log-distance model with the correct parameters derived from measurements taken in the areas. Measured path loss is shown to be consistently lower at VHF than UHF, meaning that even with the low efficiency helical antenna used in this study to simulate an IoT deployment, VHF retained its advantage for long distance communication in all the studied environments. Shadowing was shown to be close to predicted levels at VHF and UHF in all environments, with no frequency having a clear advantage. The recorded RF noise was measured and found to be consistently lower at UHF than VHF. Interesting differences were seen in the variation of individual noise measurements, shown by the standard deviation of the mean noise being higher in the urban environment (4.9 dB, over 2.3 dB higher than the next highest measurement), showing the possibility that fluctuations in noise levels relate to the time of day the measurements were taken. These results suggest that the newly repurposed VHF spectrum is suitable for IoT deployments in all the environments studied when compared to the currently utilised UHF spectrum.

Further work in this thesis will now measure the RF environment over a longer time period at static locations in order to discover if the RF noise, and indeed other propagation readings, have a time dependant factor to them possibly relating to the intensity of human activity or other factors.

Chapter 6

Time Based Measurement Campaign

In Section 5.3 it was concluded that it was possible the measurements taken in chapter 5 could have a time dependant nature, with the possibility of changing readings over time. This chapter will investigate that conclusion. This chapter will also investigate the number of users in the re-purposed VHF band and the UHF band in-order to examine the possibility using a dual band system to avoid congestion and therefore increase reliability. The study is conducted using a modified version of the instrument described in chapter 4, with changes made to fit the objectives of this chapter. The modified instrument is deployed to a single indoor location in a sub-urban area for 6 days, readings of the RF spectrum are continuously taken over this time. Measurements are taken in both the VHF and UHF band including an FFT of the spectrum, RF noise and the number of user present. These measurements are then compared between the bands. The modified instrument will also enable future work on spectrum sensing techniques, such as in the papers described in Section 3.3, the inherently reprogrammable nature of SDR will allow the new algorithms to be quickly deployed, tested and improved. The COTS nature of the instrument will also mean this research activity is cost effective and open to all.

6.1 Instrument Modification

This section will discuss the modification of the chapter 4 instrument and the reasons for each change and measurement performed. The modified instrument is intended to take long term measurements and as such it will be designed to operate indefinitely, until stopped by the user. Because measurements are intended to be taken in a static location the GPS functionality will be removed, the rest of the hardware will remain unchanged. It is envisioned that multiple instruments will be deployed to different locations at the same time, these instruments will transmit there measurements back to a central system for immediate analysis, thus eliminating the need to collect the instruments from their locations when analysis needs to be performed. This will be accomplished using Amazon Web Services (AWS) IoT core cloud based service.

In Ofcom's original consultation on the re-purposing of UHF spectrum for IoT use it was stated that there had been very few recent noise studies at the discussed frequencies [15]. Indeed, during the literature review for this research thesis it was found that most studies focus on propagation. The only recent noise study identified was by Landa *et al.* and only covered frequencies below 2MHz. Therefore, measurements of noise over time will be taken using the FFT averaging technique used in chapter 4 and further described below in Section 6.1.3.

Spectrum scarcity is a well known problem, no studies were found in the literature review relating to this in an IoT context. FFTs of the measured spectrum will be displayed as a waterfall plot, allowing a visual inspection of the number of users and the amount of congestion present. Measurements will also

be taken on the number of peaks detected in the spectrum with an SNR of over 10dB in order to ascertain if this is a good way to quantify the number of users present. This is further described in Section 6.1.3 below.

Although other changes will be made, the instrument will continue to operate with a 2.048MHz sampling frequency, taking 5000 samples for a resolution bandwidth of 409.6Hz.

The modified instrument retains its SDR nature, with all the measurements conducted in software, thus it retains its inherent re-programmability. Spectrum sensing techniques, such as the histogram-based method discussed by Bao *et al.* [27] and the detectors discussed by Yarkan *et al.* [26] could be quickly deployed on the instrument. It is intended that in the future the modified instrument will allow work to be conducted on development and testing of novel spectrum sensing and measurement algorithms.

6.1.1 IoT Cloud Service

When using the chapter 4 instrument to measure propagation, the instrument must be brought back to the lab for the measurements to be downloaded to a suitable device for the post-processing calculation algorithm to be run, this is considered appropriate because the measurements are made over a short amount of time and the nature of the test means the instrument is transported by the user. Because the modified instrument will be deployed for long periods of time away from user interaction, it is decided that the measurements will be transmitted from the modified instrument, back to a suitable device for immediate analysis and troubleshooting. This eliminates the possibility of the instrument being left in the field for extended periods of time operating in an errored state.

The chosen cloud service for the modified instrument is AWS IoT Core [75]. This service allows messages to be sent from an IoT device to Amazon's cloud servers, where the message can then be sent on to other destinations for further use. The free tier of AWS IoT is currently being utilised, this allows 500,000 messages to be sent over the cause of one year for no charge. If more capacity is required the service can handle billions of messages if the paid for tier is used. AWS provides a python SDK for use with the system, allowing the cloud services to be integrated in to the existing python programmes, such as those developed to implement the algorithms described in chapter 4.

Communication between devices and AWS IoT is subject to certificate based authentication for security purposes. Destinations for messages are set using the idea of "Topics", each device can publish and/or subscribe to a topic, when a message is published to a topic all the devices subscribed to that topic will be sent the message. Device can subscribe and publish to multiple topics. When the instruments described in this chapter are deployed to multiple locations in the field, each instrument can publish its measurements to a unique topic in order to differentiate themselves.

As well as being able to communicate between devices messages can also be sent via AWS IoT core to other AWS services, such as Amazon S3 for cloud storage, AWS Lambda to run code and Amazon Machine Learning to create machine learning models. This could prove useful in future work and allow some processing to be shifted in to the cloud.

In order to use register a device and use it with AWS IoT core the following actions must be performed in the AWS web portal:

1. Create an IoT policy - This defines a list of allowable actions, such as whether publishing or subscribing is allowed.
2. Create a "Thing" - A thing is an entry in the AWS IoT registry, each individual device must have its own entry.

3. Create and download certificates - Each thing has its own unique set of certificates that allow it to communicate securely with AWS.

4. Attach a policy to a ”Thing” certificate - This applies the defined list of allowable actions to a device, multiple devices can use the same policy.

Messages are sent using the Message Queuing and Telemetry Transport (MQTT) standard [76]. This is a lightweight messaging protocol for use in IoT applications. AWS IoT Core acts as an MQTT message broker, it receives all messages published to all topics and republishes them to all MQTT clients subscribed to the relevant topic.

An MQTT client must be set up on all devices receiving and publishing messages, this can be done using the Python SDK. The client must load the correct private key, certificate and root certificate authority (root CA). The client can be set to one of two quality of service (QoS) levels, QoS 0 sends a message zero or more times, this means the message may be missed, QoS 1 sends a message at least once and then continues sending until a receipt acknowledgement is received.

When a client session starts it can start a clean session or a persistent session. When connecting to a persistent session all topic subscriptions are reinstated and all unacknowledged messages are sent to the client at a rate of ten messages per second. Persistent sessions can time out if they are not connected to for a predetermined length of time. QoS along with persistent sessions ensure that measurements sent from the instrument will be received for analysis, even if clients experience a dropped connection.

The payload of a message sent using MQTT can not exceed 128kB, the payload can be sent as any binary data or as a JSON object. If sent as a JSON object the AWS rules engine can run SQL queries on the messages if required.

Fig. 6.1 shows a representation of an AWS IoT core network.

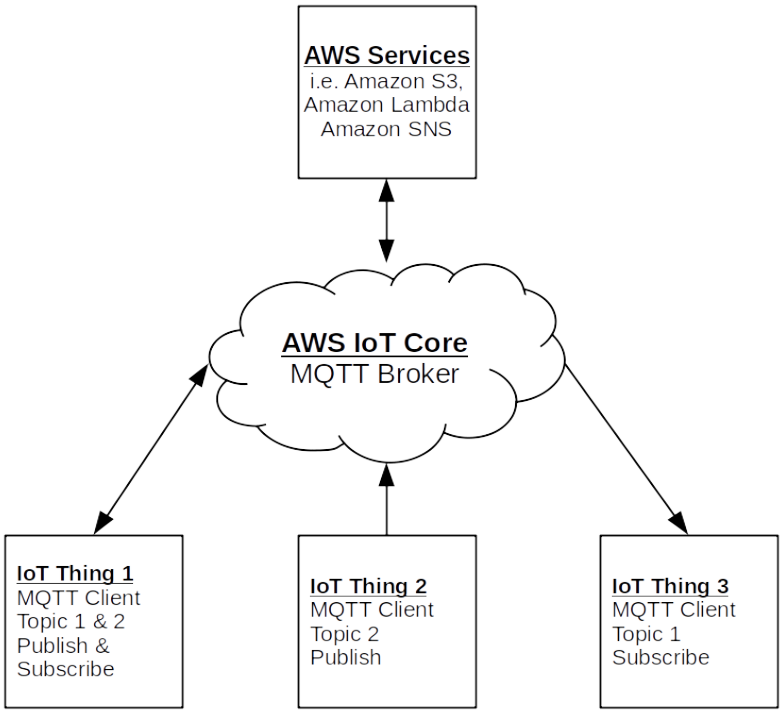

Figure 6.1: Representation of an AWS IoT Core Network

6.1.2 Cloud Publishing Algorithm

Fig. 6.2 shows how measurements are taken and published to AWS IoT core, this algorithm is written in Python. First an MQTT client is set up with the correct end point, credentials and configuration. This client is then connected to the AWS IoT core cloud. The on-system data collection algorithm described in Section 4.1.2 and Fig. 4.4 is then performed for both 71MHz and 869.525MHz in order to acquire FFTs for both frequencies in .npy format. Each of these FFTs are 40kB in size, so two can be combined in to one message of 80kB while still remaining safely under the 128kB message size limit. The message is converted in to an array of bytes and published to a chosen topic. This processes repeats until the user triggers a keyboard interrupt, at which point the data collection ends and the MQTT client is disconnected.

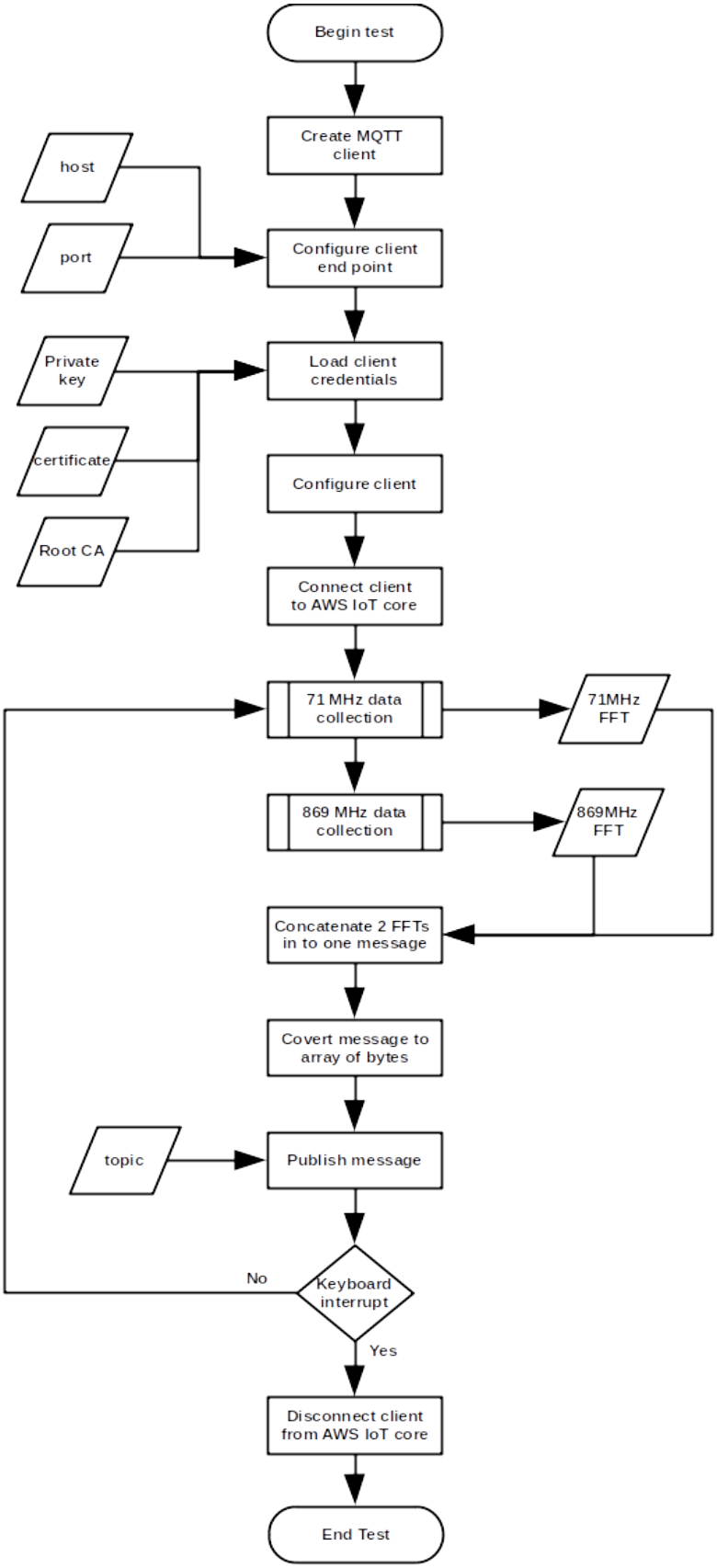

Figure 6.2: Description of Method of Publishing Measurements to the Cloud

6.1.3 Cloud Subscriber Algorithm

Fig. 6.3 how a device receives and analyses measurements, the algorithm is written in Python. The programme operates concurrently over two threads, one controls the MQTT client, the other performs measurements.

Thread 1:
First an MQTT client is set up with the correct end point, credentials and configuration. This client is then connected to the AWS IoT core cloud. The client subscribes to the topic corresponding to the deployed measurement publisher the uses wishes to work with.

The thread waits for a message to be received, once it is received it is converted back from a byte array to a message containing two FFTs and placed in a queue for the second thread, using the Python Thread module, which is designed to be used between different threads.

This processes repeats until the user triggers a keyboard interrupt, at which point the MQTT client unsubscribes from its topic and is disconnected.

Thread 2:
The thread waits for a message to be placed in the queue by the first thread. Once a message is received it is divided back in to two separate FFTs. A peak detection routine, which performs a piecewise first order differential on the FFT trace, is run on the FFT in order to identify any peaks within the collected data.

An estimation of noise within the FFT is performed by averaging the values in every FFT bin, excluding ones where a peak has been detected. This estimation allows an estimated SNR to be calculated for each detected peak.

The FFT data is added to a waterfall plot for each frequency, as shown in Fig. 6.4 & 6.7. The noise level measured is added to plots for each frequency, shown in Fig. 6.6 & 6.9. The number of peaks with an SNR greater than 10dB are appended to plots for each frequency, Shown in Fig. 6.5 & 6.8.

The thread then performs the same actions on the next message in the queue, creating an on-going plot of FFT against time, noise against time and peaks over 10dB SNR over time. This continues until the user trigger a keyboard interrupt.

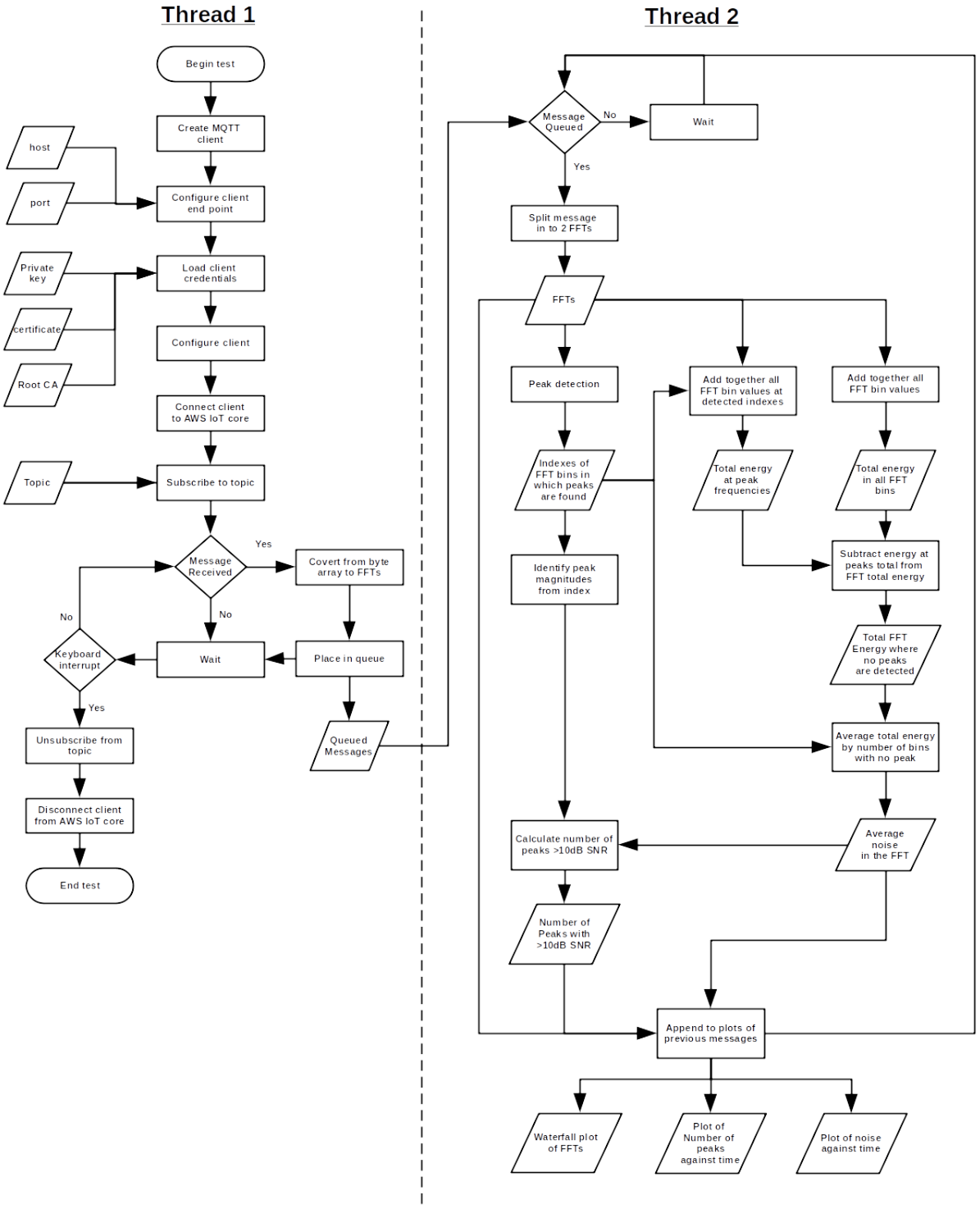

Figure 6.3: Description of Method of Receiving Messages from the Cloud and Performing Measurements

6.2 Measurements

The instrument was deployed to an indoor sub-urban location for 6 days. A total of 89,112 measurements were successfully taken, 44,561 around 71MHz and 44,561 around 869.525MHz.

Waterfall plots are created from the FFTs by assigning colours to values and stacking them one on top of the other, each FFT bin is given its own pixel in the plot. Because there are 5000 FFT bins and 44,561 individual FFTs per frequency, this means the plot image in 5000 pixels wide by 44,561 pixels high. Obviously it is impossible to reproduce this size of image on a printed page, so a reduced resolution is used here. However, the full extent of the information does still exist and it is possible to zoom in to any area of the plot to examine different features in more detail.

Fig. 6.4 shows the waterfall plot for spectrum around 71MHz. By examining the plot it is possible to see lots of interference all across the band, changing throughout the test, with a reading of unknown origin drifting between ∼70MHz and ∼70.5MHz through the entire duration of the test. Users in the band can clearly be seen by signals at ∼70.55MHz, ∼71.45MHz and ∼72MHz active throughout the duration of the test.

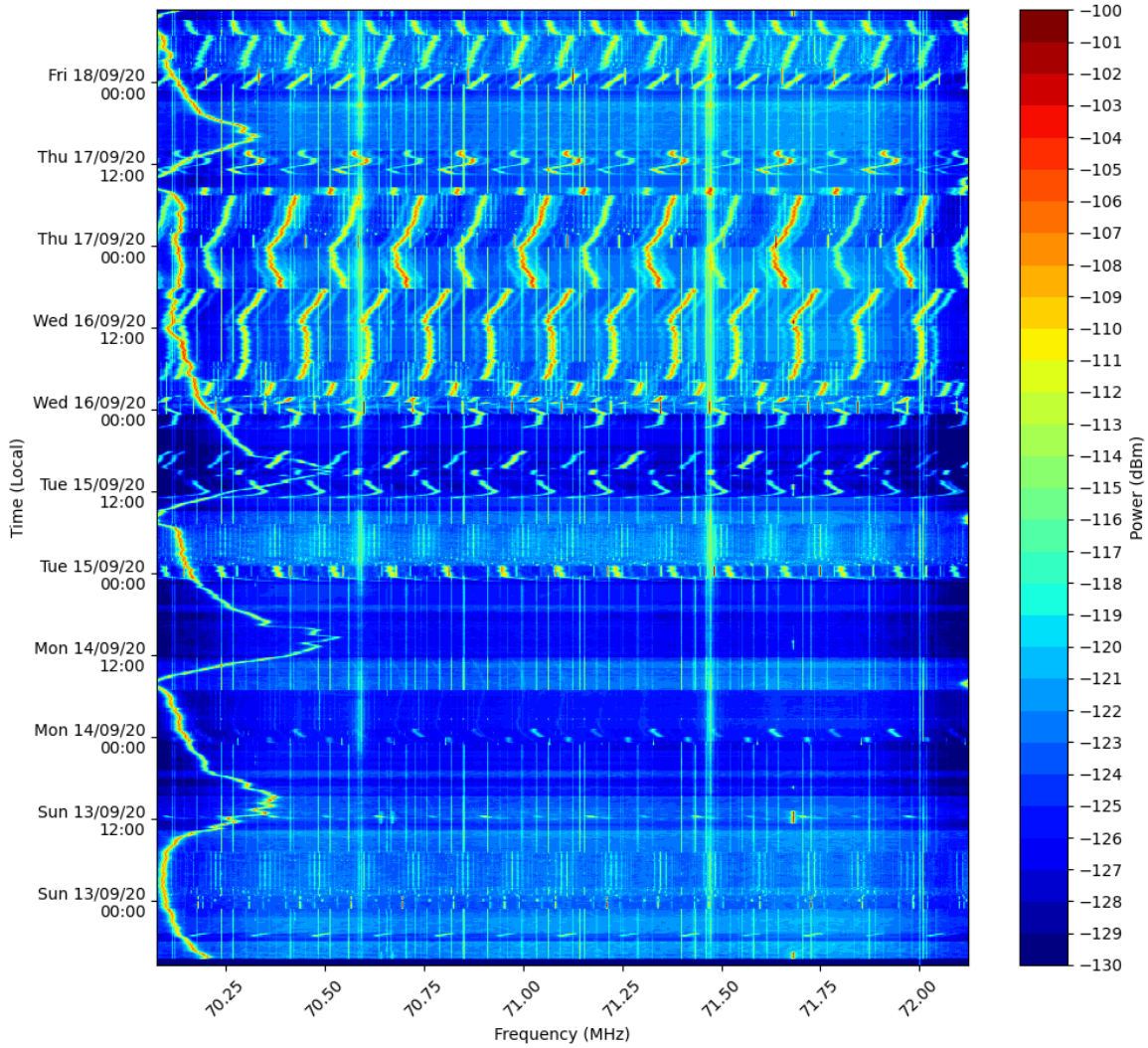

Figure 6.4: 71MHz Waterfall Plot

Fig. 6.5 shows a plot of the number of peaks detected with an SNR above 10dB against time around 71MHz. It was hoped that the number of peaks would correspond with the number of users in the band, but the amount of interference present in the band means that this measurement is proportional to the amount of interference in this case.

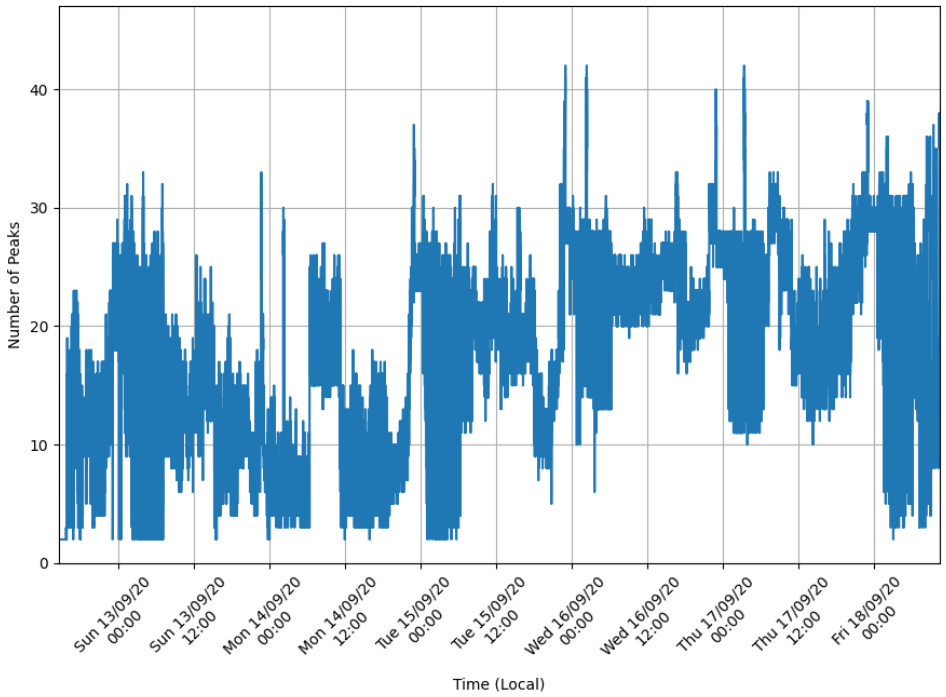

Figure 6.5: 71MHz Number of Peaks Detected with an SNR over 10dB Against Time

Fig. 6.6 shows the noise measurement against time around 71MHz. It is clearly seen that the noise does vary by a significant amount over the course of the test.

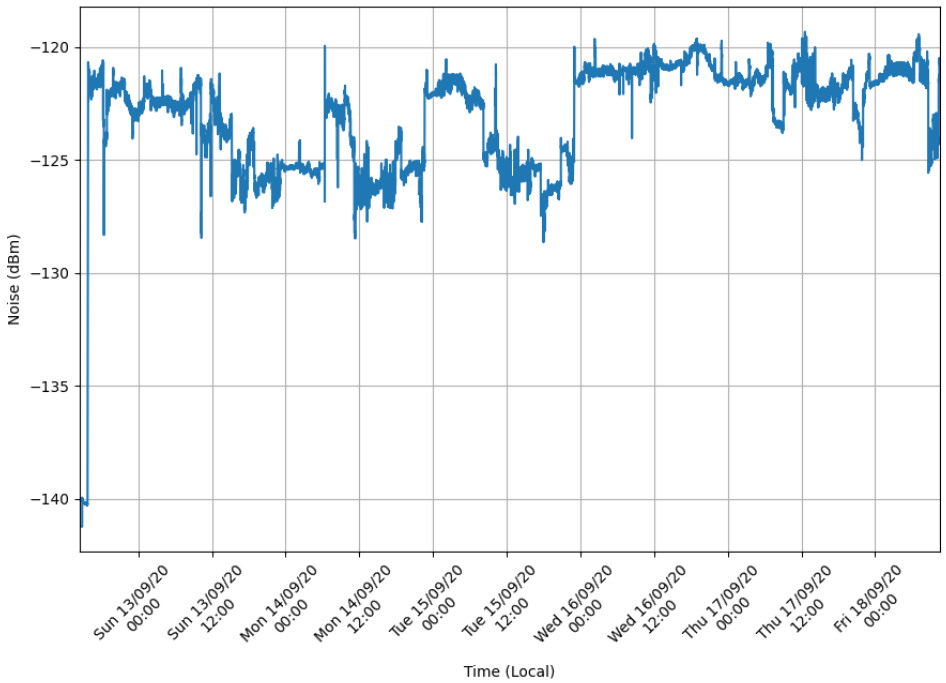

Figure 6.6: 71MHz Noise Measured Against Time

Fig. 6.7 shows the waterfall plot for spectrum around 869.525MHz. Many other users can be seen across

the band, with the most activity at the higher end of the band. One particularly strong and long-lasting signal appears at ∼869.7MHz throughout the entire test.

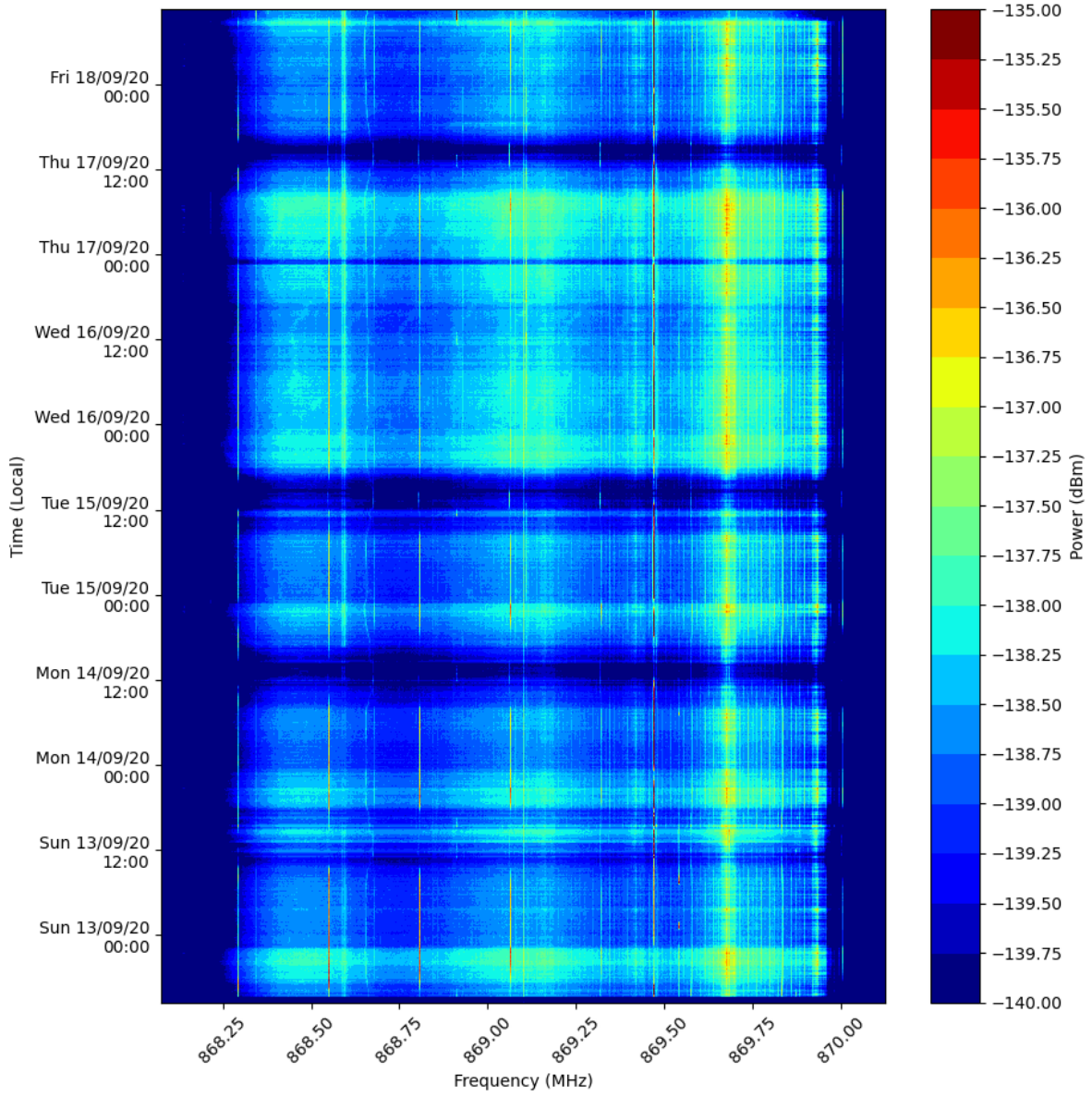

Figure 6.7: 869MHz Waterfall Plot

Fig. 6.8 shows the number of peaks with an SNR above 10dB against time around 869.525MHz. Comparing this figure to Fig. 6.7 it is clear to see that this approach did not succeed in measuring the number of users in the band. Multiple users can be manually counted in the waterfall plot, but the number of detected peaks never exceeds 3, showing no match to the number of users counted.

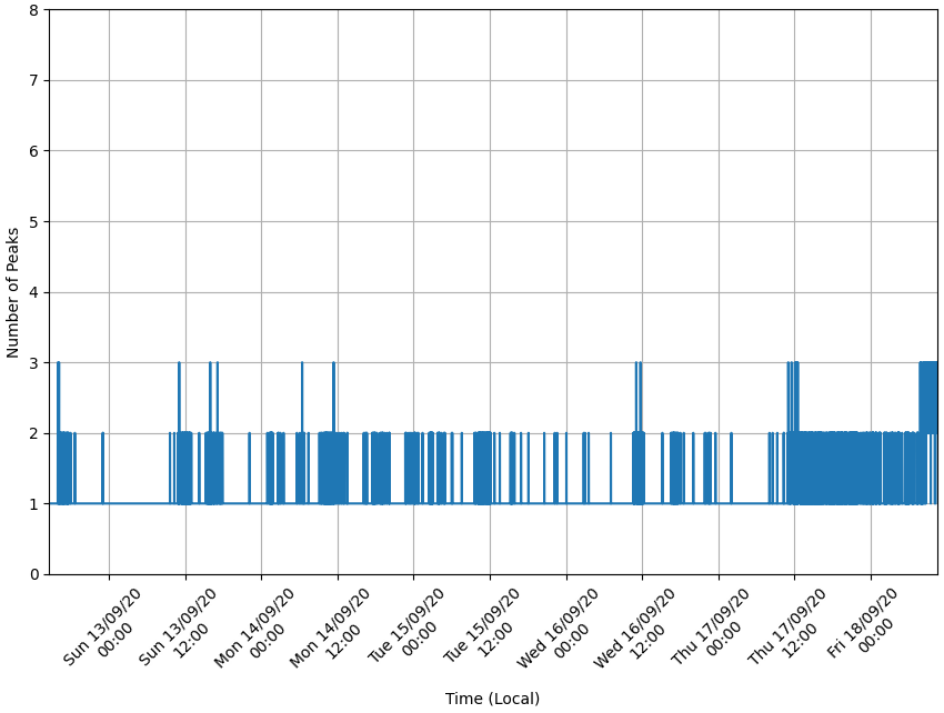

Figure 6.8: 869MHz Number of Peaks Detected with an SNR over 10dB Against Time

Fig. 6.9 shows the noise measurement against around 869.525MHz. Again it can be seen that the measured noise changes over the course of the test.

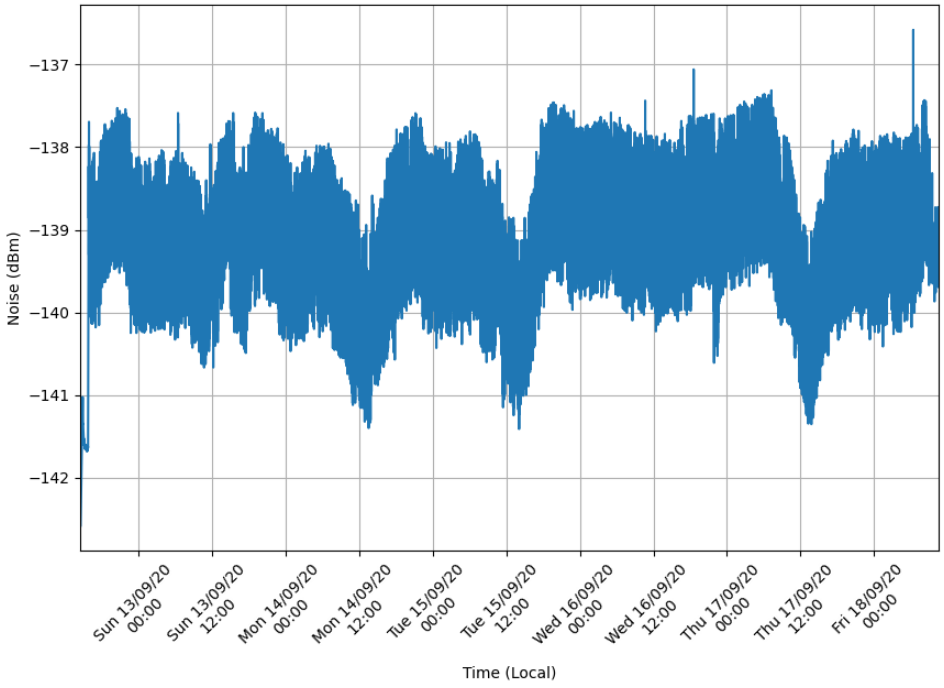

Figure 6.9: 869MHz Noise Measured Against Time

6.3 Analysis

This section will compare the measurements taken in each band of the spectrum, number of peaks over 10dB SNR and noise.

By examining Fig. 6.4 and Fig. 6.7 it can be seen that much more interference is present in the VHF spectrum with very little present in the UHF spectrum, this interference could be due to florescent lights, switched-mode power supplies or a number of other general EMI sources present in a sub-urban home. This suggests that the VHF band could be more susceptible to human made interference sources that are common around IoT deployments. This could degrade the ability for VHF spectrum to be used in high reliability applications.

When examining the other users present at UHF it can be seen that the spectrum above $\sim$869.45MHz is quite congested, but plenty of free spectrum is available at the low end of the measured band. At VHF not many other users can be seen, however they could be obscured by interference, this shows that at current usage levels congestion is unlikely in the measured VHF band. The lack of users at VHF confirm the idea that this spectrum could be used as a back-up in a high reliability dual-band system in tandem with the VHF spectrum.

Table 6.1 shows a comparison of the peaks over 10dB SNR measurements shown in Fig. 6.5 and Fig. 6.8. The greater maximum, mean and standard deviation recorded around 71MHz show clearly that a greater amount of interference is present at this frequency. The results in this area clearly show a need to implement a more sophisticated spectrum sensing algorithm to detect users and congestion, excluding interference.

Frequency (MHz)	Minimum	Maximum	Mean	Standard Deviation
71	2	42	17	7
869.525	1	3	1	0

Table 6.1: Peaks with Over 10dB SNR Measurements Analysis

Fig. 6.10 shows a comparison of the noise against time measurements from Fig. 6.6 and Fig. 6.9. It can clearly be seen that the noise around 71MHz is consistently higher than the noise 869.525MHz.

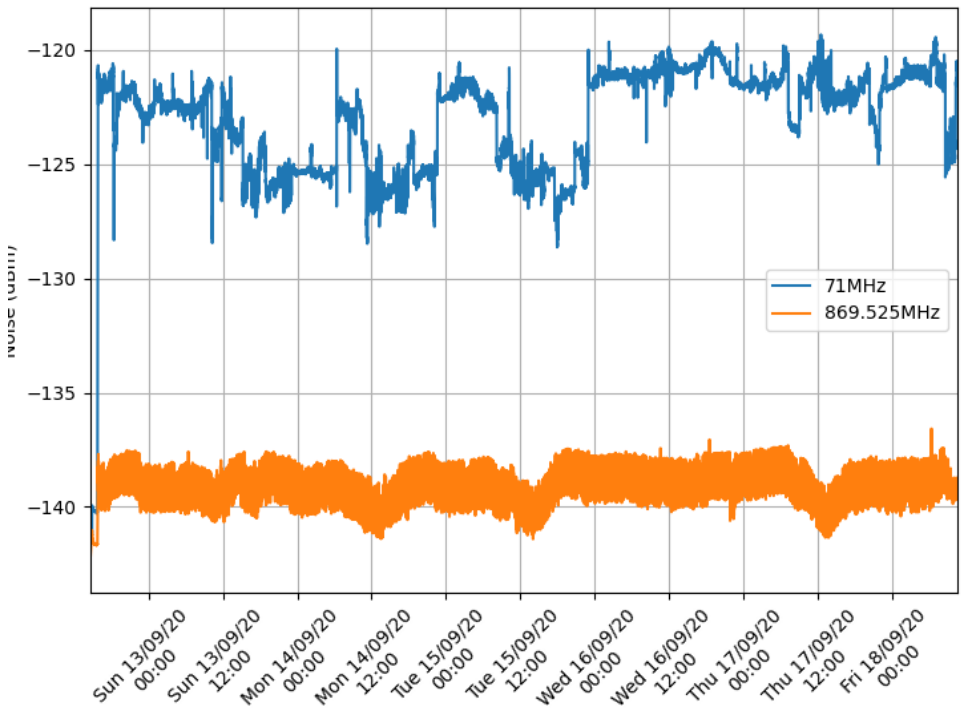

Figure 6.10: Noise Measured Against Time for VHF and UHF

Table 6.2 compares the measurements, but excludes the outlying -142.6dBm noise reading at 71MHz as an erroneous result. It shows that the mean noise level is 16dB higher in the measured VHF spectrum than the measured UHF spectrum, the standard deviation is also 1.8dB higher suggesting that the noise level is also more volatile.

Frequency (MHz)	Minimum (dBm)	Maximum (dBm)	Mean (dBm)	Standard Deviation (dB)
71	-129	-119	-123	2.4
869.525	-143	-137	-139	0.6

Table 6.2: Noise Measurements Analysis

6.4 Conclusion

It has been shown that it is possible to produce a low-cost, SDR based instrument with high enough reliability to allow the conducting of tens of thousands of measurements over an extended period of time. The possibility of relaying measurements of this type over the cloud, allowing many instruments to be distributed and remotely monitored, has also been shown to be possible. Different measurement techniques were implemented in software on the instrument, showing successfully that it could be used as a test bed for different software based spectrum sensing algorithms.

Clear differences have been discovered between the measured VHF and UHF spectrum in this specific scenario and location, such as:

- **Noise:** Consistently higher, by an average of 16dB, at VHF. More changeable, with an extra 1.8dB standard deviation to the measurements at VHF.

- **Interference:** Lots of interference present at VHF, negligible at UHF.
- **Congestion:** Qualitatively, few users and no congestion were seen at VHF, While many more users and some congestion were seen at UHF. A quantitative analysis was not possible due to the failure of the algorithm used to detect other users in the band.

From a reliability point of view, the worse performance of VHF with respect to noise and interference would cause that spectrum to be less desirable, however that may be offset by the absence of congestion.

Future work should include replacing the use of the measurements of peaks over 10dB SNR to detect other users in the band. This has been shown to be ineffective and so more sophisticated spectrum sensing techniques such as those described by Bao *et al.* [27]. Once a new technique has been implemented, the instruments should be deployed to take measurements in multiple different environments.

Chapter 7

Conclusion

This Thesis has shown the advantages in using SDR to design, test and deploy scientific instruments in a fast and flexible way using available software tools. When coupled with the use of low-cost COTS equipment, very cheap and reliable instruments can be produced, reducing the cost and therefore the bar of entry to this type of scientific study. A low-cost SDR instrument was able to be created that can perform an RF propagation study to a similar standard, within a specific use case, as a commercially produced spectrum analyser costing thousands of pounds. Agreement between the SDR instrument's measurements and measurements taken by a commercial spectrum analyser were found to be within an average of 1.4dB at 71MHz and 1.1dB at 869.525MHz. This instrument can collect hundreds of localised path loss measurements in an automated fashion, greatly reducing the manpower and time needed to conduct a propagation study.

The instrument was then able to be further quickly modified, due to its software based nature, to provide measurements for long term spectrum studies. It operated with enough reliability to be left unattended for days at a time, collecting nearly 100,000 FFTs.

These instruments were developed in order to allow the investigation of VHF spectrum that has been re-purposed by Ofcom for use in IoT applications and compare its performance to currently commercially utilised UHF spectrum. It was used to ascertain if reliable communications can be provided with the VHF spectrum and if these communications could possibly be higher in reliability than with the UHF spectrum. It was also considered that a combination of VHF and UHF in a dual band approach could provide greater reliability than either band alone.

7.1 Key Findings

The key findings of the within this thesis are listed under the following boldface headings. These findings apply only to the IoT use case and specific locations the measurements were taken within:

Current propagation models were found not to provide accurate path loss predictions for IoT deployments at VHF and UHF with near ground antennas. This was tested in the rural, sub-urban, urban and dense urban environments.

When the measured path loss was compared to predictions made by the established models listed in Chapter 5, none of them were found to be accurate with the studied use case. Table 7.1 shows the RMS errors between the predictions and measurements for each environment taken in the VHF band. Also shown is the average of the RMS error across all the environments, per model. It can be seen that the only scenarios where a less than 10dB RMS error is recorded are suburban predictions made by Two-ray and Hata urban, with Hata suburban close behind at 10.4dB. No model behaved well across all the environments, with none achieving an average RMS error less than 13.0dB.

Model	Environment (E_{RMS}(dB))				Average
	Rural	sub-urban	Urban	Dense Urban	(dB)
Free Space	37.6	37.2	44.6	38.6	39.5
Two-Ray	11.9	9.8	26.6	21.4	17.4
Hata Urban	13.4	6.6	18.7	13.3	13.0
Hata Suburban	13.0	10.4	24.0	17.5	16.2
GUPL	59.8	21.8	25.9	67.2	43.7

Table 7.1: RMS Error For All Models at VHF in All Environments

Table 7.2 shows the RMS errors between the predictions and measurements for each environment taken in the UHF band. Also shown is the average of the RMS error across all the environments, per model. It can be seen no individual model gives an RMS error of less than 22.5dB in any environment. No model behaved well across all the environments, with none achieving an average RMS error less than 29.4dB.

Model	Environment E_{RMS}(dB)				Average
	Rural	sub-urban	Urban	Dense Urban	(dB)
Free Space	63.7	63.8	60.8	61.5	62.5
Two-Ray	24.9	34.6	39.9	43.0	35.6
Hata Urban	22.5	29.8	31.9	33.2	29.4
Hata Suburban	27.3	35.3	37.4	38.7	34.7
GUPL	72.4	37.0	33.0	28.3	42.7
El Chall	24.5	40.4	40.4	39.1	36.1

Table 7.2: RMS Error For All Models at UHF in All Environments

Therefore, all of the models behaved poorly overall for both frequencies, with performance in the UHF band noticeably worse, as shown by the higher average RMS errors across the environments for each model at UHF over VHF. It is clear that these models failed because they were used outside of their intended use cases, defined in chapter 5, and cannot be repurposed for near ground IoT deployments.

Accurate log-distance propagation models were developed using tailored variables obtained through the analysis of path loss measurements taken in each environment.

Because the existing propagation models were found to be inaccurate, the measurements collected were used to develop log-distance models with tailored path loss exponents for each environment. Table 7.3 shows the RMS error between the developed models and measurements in each environment at VHF and UHF, as well as the average of the RMS error across all the environments for both frequencies. All the developed models produced an RMS error well below 10dB in each environment. The average of the RMS errors across all the environments shows that the tailored approach worked well over all environments at both frequencies.

Frequency	Environment E_{RMS}(dB)				Average
	Rural	sub-urban	Urban	Dense Urban	(dB)
VHF	6.1	5.5	8.1	8.9	7.2
UHF	6.5	8.0	9.0	7.9	7.9

Table 7.3: RMS Error For the Calculated Log-distance model at VHF and UHF in All Environments

Comparing Table 7.3 to Tables 7.1 and 7.2, it is evident that, due to the much lower average RMS errors, the developed models performed much better than the existing models.

Because the measurements used to develop these models were only taken over one example of each environmental type, it is not possible to say if the tailored variables for each environment will apply over all areas that conform to that environmental type, due to the small sample they almost certainly won't. Due to the failure of the GUPL and El Chall models, which are based on measurements in similar environments, it is possible that highly tailored models such as these do not transfer well to other areas with similar environments. It can only be said that using the using the instrument developed in chapter 4, measurements can be taken which allow tailored variable to be calculated for the measured area.

Measured path loss was consistently lower at VHF than at UHF in all environments.

Using measurements from Chapter 5 it is possible to plot Figures 7.1, 7.2, 7.3 and 7.4 which show the CDF for the measured path loss in each environment. These plots show the cumulative probability that an amount of path loss has been measured across all the path loss measurements taken in an area. From these plots it is clear that measured path loss in each environment is lower at VHF than UHF, with the cumulative probability showing that the maximum path loss measurement is reached at a lower measurement for VHF in all cases.

Fig. 7.1 shows that for a maximum outage probability of 10% in the measured rural area a link budget of at least 110dB is required at VHF and 143dB at UHF

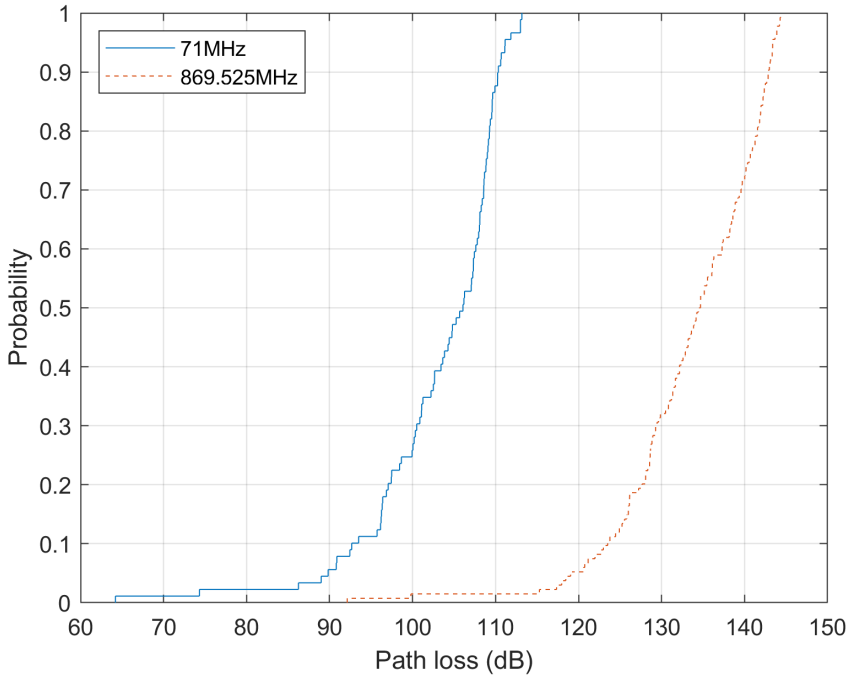

Figure 7.1: CDF of Path Loss Measurements Made in the Rural Environment

Fig. 7.2 shows that for a maximum outage probability of 10% in the measured sub-urban area a link budget of at least 114dB is required at VHF and 142dB at UHF

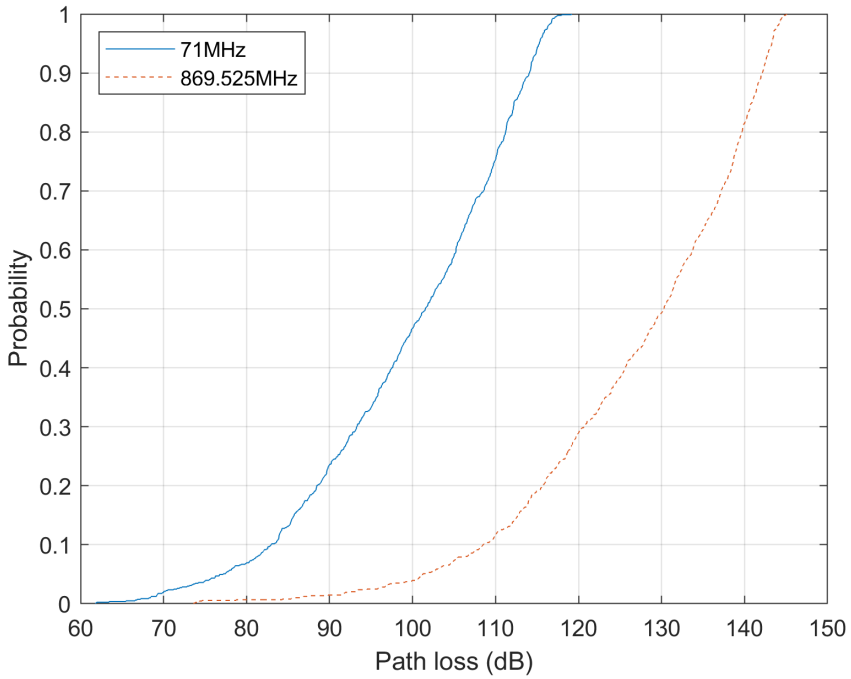

Figure 7.2: CDF of Path Loss Measurements Made in the Sub-urban Environment

Fig. 7.3 shows that for a maximum outage probability of 10% in the measured urban area a link budget of at least 118dB is required at VHF and 138dB at UHF.

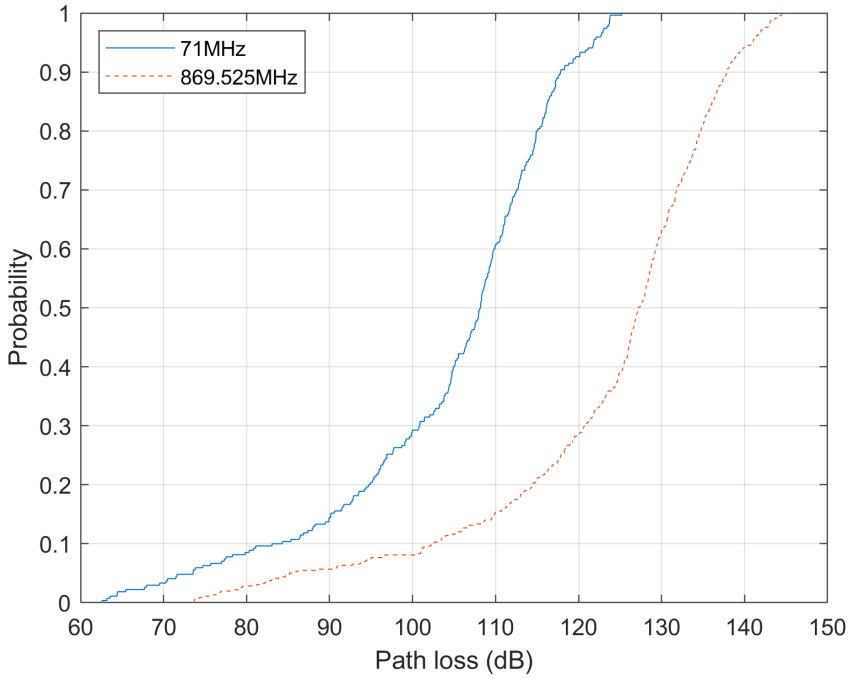

Figure 7.3: CDF of Path Loss Measurements Made in the Urban Environment

Fig. 7.4 shows that for a maximum outage probability of 10% in the measured dense urban area a link budget of at least 117dB is required at VHF and 141dB at UHF

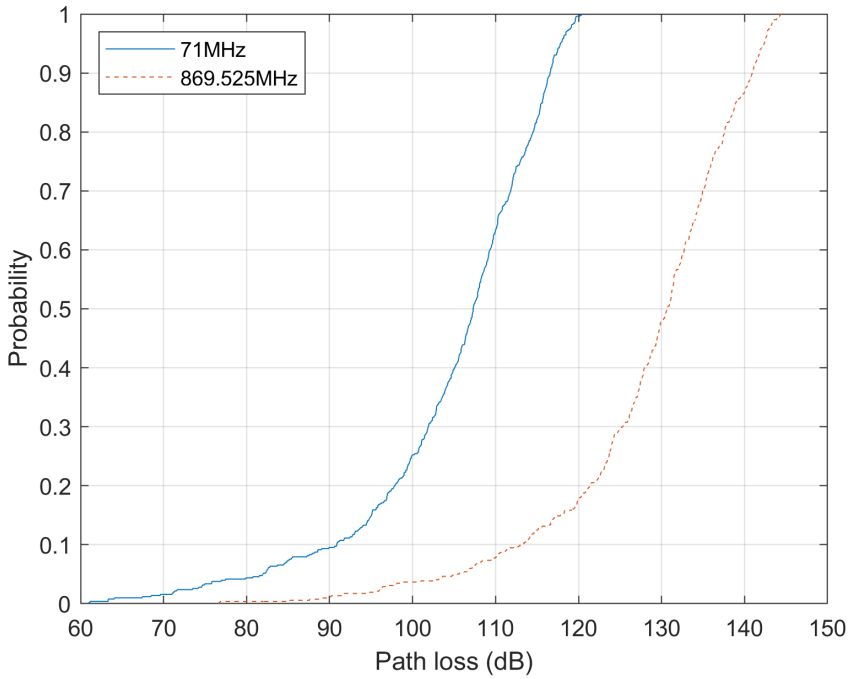

Figure 7.4: CDF of Path Loss Measurements Made in the Dense Urban Environment

This shows that the VHF link budget is more favourable by 33dB in the rural environment, 28dB in the suburban environment, 20dB in the urban environment and 24dB in the dense urban environment.

This means that, due to the lower link budget requirements, lower power could be used at VHF to cover an area than at UHF. The differences in the link budgets seem to decrease as the area becomes more built up, with the exception of the move from urban to dense urban, though it is hard to compare across the environments due to the different antenna heights used. The lower antenna used in the urban environment, when compared to the dense urban, may have skewed the results. From the measured data it is only safe to compare VHF and UHF within each environment, due to the differences in variables within the tests across the environment's.

Shadowing measurements were similar at both VHF and UHF.

Table 7.4 shows the differences between shadowing standard deviations measured at VHF and UHF, in each environment, taken in Chapter 5. This shows that in each individual environment the shadowing experienced at VHF and UHF is very similar, meaning that the use of one band over the other offered no advantage when it comes to shadowing in these tests.

Environment	Difference between VHF & UHF (dB)
ITU Prediction	1.3
Rural	0.4
Suburban	2.5
Urban	0.2
Dense Urban	1.0

Table 7.4: Differences between Shadowing Standard Deviations at VHF and UHF for Each Environment

Measured RF noise was consistently higher at VHF than at UHF, both when measured at changing locations and over time. Levels of noise were also found to be more changeable at VHF.

Table 7.5 takes the mean noise readings at each environment from Chapter 5 and the long term noise reading mean from Chapter 6. In each measured case more noise was seen at VHF than UHF, Table 7.5 shows how much more noise was measured at VHF above the UHF level, with between 8dB and 18dB extra noise recorded. Table 7.5 also shows that in 3 of the 5 scenarios a higher standard deviation for the mean was measured at VHF, this means that the noise measurements showed more variation at VHF than at UHF.

Environment	Extra noise at VHF over UHF (dB)	Extra Standard Deviation at VHF over UHF (dB)
Rural	18	0.6
Suburban	10	0
Urban	8	0
Dense Urban	9	1.4
Long-term Sub-urban	16	1.8

Table 7.5: Extra noise present at VHF, calculated between Mean Noise Measurements at VHF and UHF for Each Environment

Because noise is shown to vary over time in the measurements taken in chapter 6 it is not possible to take the low duration snapshots of noise as representative of long term trends. Indeed, the average of the long term measurement in the suburban environment gave a different result to the low duration measurement. This shows the need for more detailed investigations in to the noise in this use case, with long term measurements needed across all areas.

More interference was present in the measurements taken at VHF.

Using visual inspection of Fig. 6.4 and 6.7 it is possible to see interference sources present in the VHF spectrum, paying particular attention to the measurements made between 16/9 and 17/9 in Fig. 6.4 it is possible to see a very obvious interference pattern. Attempts were made to measure the number of users in each band by looking at the number of peaks detected with an SNR above 10dB. This attempt failed, but the measurement taken can be used to examine interference. Table 6.1 shows the maximum number of peaks detected at VHF was 42 at VHF compared to 3 at UHF, with the mean being 17 peaks at VHF and 1 at UHF. Thus, confirming that far more interference is present in the measured VHF band.

Few Users and no congestion were seen in the VHF band. The UHF band had many more users and appeared to be congested in some areas.

Because the measurement technique used to detect the number of users in a band failed, a visual inspection of the waterfall plots Fig. 6.4 and 6.7 is the only way to estimate this number. The interference present in Fig. 6.4 hinders this process, but approximately 3 to 5 concurrent users can be seen using the measured VHF band, with plenty of free spectrum available. By examining Fig. 6.7 up to 12 concurrent users can be seen in the measured UHF band, with the spectrum above 869.50MHz seeming to be fully utilised at numerous times. This is just a rough visual estimate and shows the need for more advanced spectrum sensing techniques to be utilised. However, from the estimates taken it is clear that the UHF band is more trafficked than the VHF band, this is due to the wider adoption of the SRD band within presently deployed communications technology.

A dual-Band system could allow users to take advantage of the strength of each band.

The conclusions made this far show that the VHF band has fewer users and lower path loss, but the UHF band has less noise and interference. This shows each band to have particular strengths and weaknesses, switching between these two bands could provide users with the strength of both bands together. For instance, if the UHF band becomes too congested the device could switch to the VHF band or if too much interference is present in the VHF band it could switch to the UHF band. Switching to the VHF band to take advantage of the lower path lose and therefore lower transmit power needed could be another option. Coupling the two bands with a cognitive radio type location awareness could allow devices to communicate with other devices a long way away via VHF to take advantage of the lower path loss and then switch to UHF for nearby devices when the extra link budget is not required.

Overall, The re-purposed VHF spectrum is found to be suitable for IoT applications, with better path loss and more unused spectrum available than at UHF. The lower measured path loss at VHF means longer distance communication can be provided with higher reliability than at UHF. However, the higher noise and interference seen in the VHF band will have a negative effect on this ability to provide reliable communications. Because both bands are suitable for IoT use, a dual band system using VHF and UHF could work, possibly providing higher reliability by allowing an IoT device to take advantage of the strengths of both bands.

7.2 Future Work

Opportunities for future work have been identified, first to improve the research conducted in this thesis, then to expand and extend it.

Improvements should be made to the deployments of TX antennas for the location based measurements described in chapter 5. Firstly the antennas should be deployed further away from buildings to avoid the large fixed loss seen in the rural environment test. Secondly TX sites should be secured which allow the TX antennas to deployed at the same height across all the studied environments, this will provide for a like-for-like comparison of the measurements. The sites selected should be at ground level, to further emphasise the difference between this work and previous propagation studies based on mobile phone use, with very high TX antennas.

Current work in chapter 5 shows that it is possible to produce a tailored log-distance propagation model on a site by site basis from measurements taken in a specific area. Measurements could be taken in multiple different areas of the same environmental classification, to see if there is any correlation of the propagation model variables (path loss exponent, shadowing standard deviation) within similar environments. This could lead to the development of a more general propagation model, covering all areas of a particular environment.

The time based measurements taken in chapter 6 show that the instrument is capable of providing long term measurements and that interesting features can be seen in the recorded spectrum. The next step in this work will be to develop and deploy better spectrum sensing techniques, allowing the automatic detection of other users with the measured band. This will also allow the interference to be separated out and studied further to possibly identify its source. Once the improved spectrum sensing is completed, multiple instruments can be deployed to lots of different areas over a much longer period than the initial 6 day trial. RF noise was shown to be changeable over time in the suburban environment, it is suspected that this will also be the case in the other types of environment, longer term measurements could allow patterns in these changes to be identified and studied.

Once the instrument can operate long term with accurate spectrum sensing capabilities it could be used as a test bed for new cognitive radio techniques. For instance its ability to identify other users could allow the investigation of white space spectrum hopping. One of the strengths of using SDR for research identified in chapter 4 was the ease in which measurement algorithms could be deployed, tested and changed. This advantage would also prove useful here, with new CR algorithms able to be implemented easily.

Glossary

A

ADC Analogue to Digital Converter.

AI Artificial Intelligence.

AWS Amazon Web Services.

C

CDF Cumulative Distribution Function.

COTS Commercial Off The Shelf.

CR Cognitive Radio.

CSV Comma Separated Values.

CW Continuous Wave.

D

DANL Displayed Average Noise Level.

DC Direct Current.

DSP Digital Signal Processing.

DVB-T Digital Video Broadcasting - Terrestrial.

E

E Field Electric Field.

ECG Electrocardiogram.

EEG Electroencephalogram.

EM Electromagnetic.

ERIP Effective Isotropic Radiated Power.

EU European Union.

F

FFT Fast Fourier Transform.

FPGA Field-programmable Gate Array.

FSPL Free Space Path Loss.

G

GPIO General Purpose Input and Output.

GPS Global Positioning System.

GSM Global System for Mobile Communications.

GUPL General Urban Path Loss Model.

H

H Field Magnetic Field.

I

IEEE Institute of Electrical and Electronics Engineers.

IF Intermediate Frequency.

IoT Internet of Things.

IQ In-phase and Quadrature.

ITU International Telecommunications Union.

J

JSON Java-script Object Notation.

L

LNA Low Noise Amplifier.

LoS Line of Sight.

LPWAN Low-power Wide-area Network.

M

MQTT Message Queuing and Telemetry Transport Standard.

N

NI National Instruments.

NLOS Non Line of Sight.

O

Ofcom The Office of Communications, UK telecommunications regulator.

OFDM Orthogonal Frequency Division Multiplexing.

P

PC Personal Computer.

PSD Power Spectral Density.

PSK Phase Shift Keying.

Q

QoS Quality of Service.

R

R&D Research & Development.

RAM Random-access Memory.

RBW Resolution Bandwidth.

RF Radio Frequency.

RFID Radio Frequency Identification.

RMS Root Mean Square.

RMSE Root Mean Squared Error.

RSSI Received Signal Strength Indicator.

RTL-SDR Commercial Software Defined Radio Receiver.

RX Radio Receiver.

S

SA Spectrum Analyser.

SDE Standard Deviation of the Mean Error Between a Measurement and a Predication.

SDK Software Development Kit.

SDR Software Defined Radio.

SNR Signal-to-Noise Ratio.

SQL Structure Query Language.

SRD Short Range Devices.

T

TCXO Temperature Compensated Crystal Oscillator.

TVWS Television White Space.

TX Radio Transmitter.

U

UHF Ultra High Frequency.

UK United Kingdom of Great Britain and Northern Ireland.

USA United States of America.

USB Universal Serial Bus.

USRP Universal Software Radio Peripheral.

V

VHF Very High Frequency.

VNA Vector Network Analyser.

References

[1] T. S. Rappaport, *Wireless Communications : principles and practice*. Prentice-Hall, 2002.

[2] C. A. Balanis, *Antenna Theory: Analysis and Design*. Wiley, 2005.

[3] D. P. Wright and E. A. Ball, "Highly portable software defined radio test bed for dual band propagation studies," in *The Loughborough Antennas Propagation Conference (LAPC 2018)*, Nov 2018, pp. 1–6.

[4] D. P. Wright and E. A. Ball, "Highly portable, low-cost sdr instrument for rf propagation studies," *IEEE Transactions on Instrumentation and Measurement*, vol. 69, no. 8, pp. 5446–5457, August 2020.

[5] D. P. Wright and E. A. Ball, "Iot focused vhf and uhf propagation study and comparisons," *IET Microwaves, Antennas & Propagation*, vol. 15, no. 8, pp. 871–884, 2021.

[6] Oracle, "What is the internet of things (iot)?" accessed: 16 January 2020. [Online]. Available: https://www.oracle.com/uk/internet-of-things/what-is-iot.html

[7] ETSI, "Electromagnetic compatibility and Radio spectrum Matters (ERM); Short Range Devices (SRD); Radio equipment to be used in the 25 MHz to 1 000 MHz frequency range with power levels ranging up to 500 mW; Part 1: Technical characteristics and test methods," 2012.

[8] LoRa Alliance, "What is LoRaWAN?" 2015, accessed: 27 May 2021. [Online]. Available: https://docs.wixstatic.com/ugd/eccc1a_ed71ea1cd969417493c74e4a13c55685.pdf

[9] LORA Alliance, "Showcase search - lora alliance," 2021, accessed: 21 May 2021. [Online]. Available: https://lora-alliance.org/showcase/search/?_sfm_lorawan_certified_device=certified

[10] Sigfox, "Technology," accessed: 21 May 2021. [Online]. Available: https://www.sigfox.com/en/what-sigfox/technology

[11] Sigfox, "News," accessed: 21 May 2021. [Online]. Available: https://www.sigfox.com/en/news

[12] Wi-Fi Alliance, "Wi-Fi HaLow," 2021, accessed: 21 May 2021. [Online]. Available: https://www.wi-fi.org/discover-wi-fi/wi-fi-halow

[13] WI-FI Alliance, "Wi-Fi HaLow - Worth the Wait," 2021, accessed: 21 May 2021. [Online]. Available: https://www.wi-fi.org/beacon/kevin-walsh/wi-fi-halow-worth-the-wait

[14] X. Zhang, T. W. Burress, K. B. Albers, and W. B. Kuhn, "Propagation comparisons at vhf and uhf frequencies," in *2009 IEEE Radio and Wireless Symposium*, Jan 2009, pp. 244–247.

[15] OFCOM, "Vhf radio spectrum for the internet of things," March 2016, accessed: 21 May 2021. [Online]. Available: https://www.ofcom.org.uk/__data/assets/pdf_file/0029/78563/vhf-iot-statement.pdf

[16] ITU-R, "Question ITU-R 203-8/3: Propagation prediction methods for terrestrial broadcasting, fixed (broadband access) and mobile services using frequencies above 30 MHz," 2019.

[17] ITU-T, "Reccomendation ITU-T E.800 Definitions of terms related to quality of service," 2011.

[18] H. Hecht, *Systems Reliability and Failure Prevention*. Artech House, 2003.

[19] F. T. Dagefu, G. Verma, C. R. Rao, P. L. Yu, J. R. Fink, B. M. Sadler, and K. Sarabandi, "Short-range low-vhf channel characterization in cluttered environments," *IEEE Transactions on Antennas and Propagation*, vol. 63, no. 6, pp. 2719–2727, June 2015.

[20] J. Mitola, "The software radio architecture," IEEE Communications Magazine, pp. 26–38, May 1995.

[21] C. R. Aguayo González, C. B. Dietrich, and J. H. Reed, "Understanding the software communications architecture," IEEE Communications Magazine, pp. 50–57, September 2009.

[22] D. Carey, R. Lowdermilk, and M. Spinali, "Testing software defined and cognitive radios using software defined synthetic instruments," IEEE Instrumentation & Measurement Magazine, pp. 19–24, April 2015.

[23] W. Tuttlebee, *Software Defined Radio: Enabling Technologies*. Wiley, 2002.

[24] IEEE Computer Society, "Part 22: Cognitive Wireless RAN Medium Access Control (MAC) and Physical Layer (PHY) Specifications: Policies and Procedures for Operation in the TV Bands," 2011.

[25] IEEE Computer Society, "Ieee 802.11af-2013 - ieee standard for information technology - telecommunications and information exchange between systems - local and metropolitan area networks - specific requirements - part 11: Wireless lan medium access control (mac) and physical layer (phy) specifications amendment 5: Television white spaces (tvws) operation," 2013.

[26] S. Yarkan, "A generic measurement setup for implementation and performance evaluation of spectrum sensing techniques: Indoor environments," *IEEE TRANSACTIONS ON INSTRUMENTATION AND MEASUREMENT*, vol. 64, no. 3, pp. 606–614, March 2015.

[27] D. Bao, L. De Vito, and S. Rapuano, "A histogram-based segmentation method for wideband spectrum sensing in cognitive radios," *IEEE Transactions on Instrumentation and Measurement*, vol. 62, no. 7, pp. 1900–1908, 2013.

[28] Y. Huang and K. Boyle, *ANTENNAS: FROM THEORY TO PRACTICE*. Wiley, 2008.

[29] ITU-R, "Recommendation ITU-R P.372-14 Radio Noise," 2019.

[30] Agilent Technologies, "Application note 57-1: Fundamentals of rf and microwavenoise figure measurements," 2004.

[31] ITU, "Radio Regulations - Articles - Volume 1," 2020.

[32] ITU-R, "Recommendation ITU-R P.452-16 Prediction procedure for the evaluation of interference between stations on the surface of the Earth at frequencies above about 0.1 GHz," 2015.

[33] A. V. Oppenheim, R. W. Schafer, and J. R. Buck, *Discrete-Time Signal Processing*. Prentice Hall, 1999.

[34] Agilent Technologies, "Application note 1383-1: Spectral analysis using a deep-memory oscilloscope fast fourier transform (fft)," 2001.

[35] A. Goldsmith, *Wireless Comunications*. Cambridge University Press, 2005.

[36] ITU-R, "Recommendation ITU-R P.529-3 PREDICTION METHODS FOR THE TERRESTRIAL LAND MOBILE SERVICE IN THE VHF AND UHF BANDS," 1999.

[37] ITU, "Radiowave propagation," accessed: 27 May 2021. [Online]. Available: https://www.itu.int/rec/R-REC-P/en

[38] F. Fuschini, M. Barbiroli, G. E. Corazza, V. Degli-Esposti, and F. G., "Analysis of Outdoor-to-Indoor Propagation at 169 MHz for Smart Metering Applications," *IEEE TRANSACTIONS ON ANTENNAS AND PROPAGATION*, vol. 63, no. 4, pp. 1811–1821, 2015.

[39] N. Faruk, O. W. Bello, N. T. Surajudeen-Bakinde, O. Obiyemi, L. A. Olawoyin, M. Ali, and A. Jimoh, "Clutter and terrain effects on path loss in the vhf/uhf bands," *IET Microwaves, Antennas and Propagation*, vol. 12, no. 1, pp. 69–76, 2018.

[40] J. Andrusenko, R. L. Miller, J. A. Abrahamson, N. M. Merheb Emanuelli, R. S. Pattay, and R. M. Shuford, "VHF General Urban Path Loss Model for Short Range Ground-to-Ground Communications," *IEEE TRANSACTIONS ON ANTENNAS AND PROPAGATION*, vol. 56, no. 10, pp. 3302–3310, 2008.

[41] D. M. J. Devasirvatham, C. Banerjee, M. J. Krain, and D. A. Rappaport, "Multi-frequency radiowave propagation measurements in the portable radio environment," in *IEEE International Conference on Communications, Including Supercomm Technical Sessions*, vol. 4, April 1990, pp. 1334–1340.

[42] M. Ayadi, A. Ben Zineb, and S. Tabbane, "A uhf path loss model using learning machine for heterogeneous networks," *IEEE Transactions on Antennas and Propagation*, vol. 65, no. 7, pp. 3675–3683, July 2017.

[43] Berkeley Varitronics Systems, Inc., "Coyote Dual Modular Receiver," 2018, accessed: 27 May 2021. [Online]. Available: https://www.bvsystems.com/product/coyote-dual-modular-receiver/.

[44] R. El Chall, S. Lahoud, and M. El Helou, "Lorawan network: Radio propagation models and performance evaluation in various environments in lebanon," *IEEE Internet of Things Journal*, vol. 6, no. 2, pp. 2366–2378, April 2019.

[45] T. K. Sarkar, M. N. Abdallah, and M. Salazar-Palma, "Survey of available experimental data of radio wave propagation for wireless transmission," *IEEE Transactions on Antennas and Propagation*, vol. 66, no. 12, pp. 6665–6672, Dec 2018.

[46] R. M. Sandoval, A. Garcia-Sanchez, and J. Garcia-Haro, "Improving rssi-based path-loss models accuracy for critical infrastructures: A smart grid substation case-study," *IEEE Transactions on Industrial Informatics*, vol. 14, no. 5, pp. 2230–2240, May 2018.

[47] J. Hejselbæk, J. Ødum Nielsen, W. Fan, and G. F. Pedersen, "Empirical study of near ground propagation in forest terrain for internet-of-things type device-to-device communication," *IEEE Access*, vol. 6, pp. 54 052–54 063, 2018.

[48] R. K. Tewari, S. Swarup, and M. N. Roy, "Radio wave propagation through rain forests of india," *IEEE Transactions on Antennas and Propagation*, vol. 38, no. 4, pp. 433–449, 1990.

[49] W. Wang, L. Yang, Q. Zhang, and T. Jiang, "Securing on-body iot devices by exploiting creeping wave propagation," *IEEE Journal on Selected Areas in Communications*, vol. 36, no. 4, pp. 696–703, April 2018.

[50] I. Oraibi, C. E. Otero, and T. O. Olasupo, "Empirical path loss model for vehicle-to-vehicle iot device communication in fleet management," in *2017 16th Annual Mediterranean Ad Hoc Networking Workshop (Med-Hoc-Net)*, 2017, pp. 1–4.

[51] J. Stewart, R. Stewart, and S. Kennedy, "Internet of things — propagation modelling for precision agriculture applications," in *2017 Wireless Telecommunications Symposium (WTS)*, 2017, pp. 1–8.

[52] A. Cheu, M. M. Morys, C. R. Anderson, and G. D. Durgin, "Rf propagation through vegetation with time-varying moisture," in *2016 IEEE Radio and Wireless Symposium (RWS)*, 2016, pp. 73–75.

[53] J. Boksiner, Y. Posherstnik, M. Murphy, C. Chrysanthou, T. Marsault, and J. Millet, "Validation of an analytical urban propagation model," in *MILCOM 2016 - 2016 IEEE Military Communications Conference*, 2016, pp. 717–722.

[54] W. F. Young, K. A. Remley, C. L. Holloway, G. Koepke, D. Camell, J. Ladbury, and C. Dunlap, "Radiowave propagation in urban environments with application to public-safety communications," *IEEE Antennas and Propagation Magazine*, vol. 56, no. 4, pp. 88–107, 2014.

[55] I. Landa, A. Arrinda, M. Velez, and I. Eizmendi, "Indoor radio noise long-term variation in medium wave band based on measurements," *IEEE Transactions on Antennas and Propagation*, vol. 62, no. 6, pp. 3398–3401, 2014.

[56] C. Andrich, A. Ihlow, J. Bauer, N. Beuster, and G. Del Galdo, "High-precision measurement of sine and pulse reference signals using software-defined radio," *IEEE TRANSACTIONS ON INSTRUMENTATION AND MEASUREMENT*, vol. 67, no. 5, pp. 1132–1141, May 2018.

[57] L. Catarinucci, D. De Donno, R. Colella, F. Ricciato, and L. Tarricone, "A Cost-Effective SDR Platform for Performance Characterization of RFID Tags," *IEEE TRANSACTIONS ON INSTRUMENTATION AND MEASUREMENT*, vol. 63, no. 4, pp. 903–911, 2012.

[58] R. Colella, L. Catarinucci, P. Coppola, and L. Tarricone, "Measurement Platform for Electromagnetic Characterization and Performance Evaluation of UHF RFID Tags," *IEEE TRANSACTIONS ON INSTRUMENTATION AND MEASUREMENT*, vol. 65, no. 4, pp. 905–914, April 2016.

[59] C. Stagner, M. Halligan, C. Osterwise, D. G. Beetner, and S. L. Grant, "Locating noncooperative radio receivers using wideband stimulated emissions," *IEEE TRANSACTIONS ON INSTRUMENTATION AND MEASUREMENT*, vol. 62, no. 3, pp. 667–674, March 2013.

[60] S. Majhi, M. Kumar, and W. Xiang, "Implementation and measurement of blind wireless receiver for single carrier systems," *IEEE TRANSACTIONS ON INSTRUMENTATION AND MEASUREMENT*, vol. 66, no. 8, pp. 1965–1975, 2017.

[61] V. Goverdovsky, D. C. Yates, M. Willerton, C. Papavassiliou, and E. Yeatman, "Modular software-defined radio testbed for rapid prototyping of localization algorithms," *IEEE TRANSACTIONS ON INSTRUMENTATION AND MEASUREMENT*, vol. 65, no. 7, pp. 1577–1584, 2016.

[62] P. Bilski and W. Winiecki, "A low-cost real-time virtual spectrum analyzer," *IEEE TRANSACTIONS ON INSTRUMENTATION AND MEASUREMENT*, vol. 56, no. 6, pp. 2169–2174, 2007.

[63] E. Schmidt, D. Akopian, and D. J. Pack, "Development of a real-time software-defined gps receiver in a labview-based instrumentation environment," *IEEE TRANSACTIONS ON INSTRUMENTATION AND MEASUREMENT*, vol. 67, no. 9, pp. 2082–2096, Sep 2018.

[64] A. Soghoyan, A. Suleiman, and D. Akopian, "A Development and Testing Instrumentation for GPS Software Defined Radio With Fast FPGA Prototyping Support," *IEEE TRANSACTIONS ON INSTRUMENTATION AND MEASUREMENT*, vol. 63, no. 8, pp. 2001–2012, Aug 2014.

[65] Nooelec, "Nooelec NESDR SMArt SDR - Premium RTL-SDR w/ Aluminum Enclosure, 0.5PPM TCXO, SMA Input. RTL2832U, R820T2-Based," accessed: 27 May 2021. [Online]. Available: https://www.nooelec.com/store/sdr/nesdr-smart-sdr.html

[66] RASPBERRY PI FOUNDATION, "Raspberry pi 3 model b," accessed: 27 May 2021. [Online]. Available: https://www.raspberrypi.org/products/raspberry-pi-3-model-b/

[67] Y. Liu, "Concurrent dual-band rf signal measurement with adaptive blind feedforward cancellation of wideband receiver nonlinearities," *IEEE TRANSACTIONS ON INSTRUMENTATION AND MEASUREMENT*, vol. 66, no. 8, pp. 1976–1984, Aug 2017.

[68] Captain, HM Navigation School, *Admiralty Navitagtion Manual, Vol 2*. HM Stationery Office, 1938.

[69] E. A. Ball, "Design and field trial measurement results for a portable and low-cost very-high-frequency/ultra-high-frequency channel sounder platform for internet of things propagation research," *IET Microwaves, Antennas Propagation*, vol. 13, no. 6, pp. 714–724, 2019.

[70] ITU-R, "Recommendation ITU-R P.525-3 Calculation of free-space attenuation," 2016.

[71] Silicon Labs, "Si106X Delelopment Kits User's Guide," 2017, accessed: 30 July 2020. [Online]. Available: https://www.silabs.com/documents/public/user-guides/Si106x-DK.pdf

[72] J. Karedal, N. Czink, A. Paier, F. Tufvesson, and A. F. Molisch, "Path loss modeling for vehicle-to-vehicle communications," *IEEE Transactions on Vehicular Technology*, vol. 60, no. 1, pp. 323–328, 2011.

[73] ITU-R, "Recommendation ITU-R P.1406-2 Propagation effects relating to terrestrial land mobile and broadcasting services in the VHF and UHF bands," June 2015.

[74] ITU-R, "Recommendation ITU-R P.2108-0 Prediction of clutter loss," June 2017.

[75] Amazon Web Services, "AWS IoT Core: Developer Guide," 2020.

[76] MQTT.org, "MQTT: The Standard for IoT Messaging," 2020, accessed: 15 September 2020. [Online]. Available: https://mqtt.org/